UV/VUV transmission characteristics of capillary-array windows

by
Haoyu Cheng

A dissertation submitted in partial fulfillment
of the requirements for the degree of

Doctor of Philosophy
(Electrical and Computer Engineering)

at the
University of Wisconsin-Madison
2023

Date of final oral examination: 05/25/2023

This dissertation is approved by the following members of the Final Oral Committee:
J. Leon Shohet, Professor Emeritus, Electrical and Computer Engineering
Zhenqiang Ma, Professor, Electrical and Computer Engineering
Hongrui Jiang, Professor, Electrical and Computer Engineering
Dan Botez, Professor, Electrical and Computer Engineering
Hau D. Le, Assistant Professor, Surgery

Abstract

Capillary-array windows have garnered significant interest in the realm of plasma processing and semiconductor fabrication. One potential application of these windows is their use in enabling the transmission of optical radiation produced by plasma processing systems while simultaneously safeguarding the substrate being exposed to these radiation from damage caused by high-energy electrons, ions, and neutral particles generated in the plasma.

The hypothesis of this study posits that capillary-array windows would exhibit superior optical transmission capabilities in the ultraviolet (UV) and vacuum-ultraviolet (VUV) range in comparison to solid thin films. Furthermore, it is believed that the transmission efficiency of the capillary-array windows can be maximized by optimizing their dimension and the experimental settings while still maintaining a substantial pressure differential between two regimes.

Three types of capillary-array windows were considered, classified according to their pore size: nanoporous, microporous, and milliporous. The nanoporous capillary-array windows were found to behave similarly to solid thin films, with low transmission of optical radiation in the ultraviolet (UV) and vacuum-ultraviolet (VUV) range. In contrast, the microporous and milliporous capillary-array windows exhibited UV and VUV transmission efficiencies of up to approximately 58.93% and 44.87%, respectively.

This work employed a fractional-factorial design method to investigate the effect of various factors on the optical transmission through capillary-array windows. These factors included pore diameter, window thickness, open area ratio (OAR), exposed area, wavelength of incident radiation, and incident angle of radiation. Subsequent statistical analyses, including effect analysis, ANOVA, and regression analysis, were conducted to determine the optimal optical transmission

through microporous and milliporous capillary-array windows. The results showed that the optimal optical transmission through microporous capillary-array windows was 59.24%, which closely aligned with the theoretical maximum of 60%. Similarly, the optimal optical transmission through milliporous capillary-array windows was found to be 45.03%, which aligned well with the theoretical maximum of 44%.

In addition to the optical transmission measurements, several rounds of pressure tests were conducted on the capillary-array windows to evaluate their mechanical durability. The windows were subjected to two initial pressure differentials: (1) 10^{-6} torr to 20 mtorr, which mimics the condition of optical transmission measurements through the capillary-array windows in the Electron Cyclotron Resonance (ECR) plasma system, and (2) 20 mtorr to 760 torr, which is the pressure range required for generating UV and VUV radiation. All capillary-array windows were observed to withstand these pressure differentials without any failure. Further pressure tests were conducted to investigate the maximum pressure differential that capillary-array windows could withstand before failure. The results revealed that the capillary-array windows demonstrated a high tolerance for pressure differentials of several hundred of psi without experiencing any failure.

Acknowledgements

Throughout my Ph.D. journey at the University of Wisconsin Madison, I have had the privilege of collaborating with a diverse and exceptional group of individuals who have significantly influenced my personal and academic growth. Their unwavering support, guidance, and contributions have been paramount in the completion of my research. I wish to express my utmost gratitude and appreciation to these individuals for their invaluable efforts, without which my accomplishments would not have been possible.

First and foremost, I would like to express my deepest gratitude to my advisor, Prof. J. Leon Shohet, for his invaluable guidance and unwavering support throughout my entire research life. His expert knowledge, critical feedback, and tireless dedication have been instrumental in the success of this project and encouraged me throughout my academic research career and daily life. Without his council, I would never get to where I am today. I would also like to thank Prof. Zhenqiang Ma, whose expertise was invaluable in the development of this work. His insightful feedback pushed me to sharpen my thinking and elevate my work. Additionally, I would also like to thank the members of my thesis defense committee, Prof. Hongrui Jiang, Prof. Dan Botez, and Prof. Hau D. Le, for their insightful comments and helpful suggestions that have greatly improved the quality of this work.

My appreciation also goes to my colleagues and friends who have provided me with a stimulating research environment and supported me during the ups and downs of the journey. In particular, I would like to thank my lab mates, Dr. Josh Blatz and the future Dr. Yuting Wu, for their encouragement and friendship. Working collaboratively with their accomplished scientific minds has been a rewarding experience, and our conversations have been invaluable to my research.

I am also deeply appreciative of the opportunity to work alongside exceptional colleagues, including Yu Huang, Panpan Xue, Ha Nguyen, Dajun Zhang, Tingyou Gou, Dan Benjamin, Faraz Choudhury, Majid Altoumi, Huifeng Zheng, and He Ren. I would also thank my best friends, Kimberly Blatz, Yuanyuan Wang, Prof. Chunzi Liang, Dr. Zhongkai Sun, Dr. Xinnan Li, and Dr. Youjuan Li. Their unwavering support, encouragement, and guidance have been invaluable to me, especially during challenging times when I was struggling with the pressure and sleepless nights.

Nobody has been more important to me in the pursuit of this work than the members of my family. I would like to thank my parents, Guang'ao Cheng and Chunxiu Li, for their enduring love and guidance, which have contributed significantly to shaping my character and professional growth. The unwavering support of my family has been a pillar of strength, providing a constant source of encouragement to pursue my aspiration. Most importantly, I wish to express my sincere appreciation to my partner, Zhidong Chen, for her affectionate, thoughtful, and patient support throughout this journey, without which, none of this would have been possible.

Table of Contents

Chapter 1 - Introduction

1.1 Motivation

Plasma processing has a wide range of applications in the semiconductor industry where it is used for, but not limited to, fine line-pattern definition, selective processing over topography, planarization, and resist stripping.[1] During processing, semiconductor materials are often exposed to plasma-generated ultraviolet (UV) and vacuum-ultraviolet radiation (VUV), as well as electrons, ions, and neutral particles that can lead to damage to the materials under exposure.[2] Also, experiments with optical-radiation sources often require separation of a region of relatively high pressure from a low-pressure region while allowing transmission of radiation between regions.[3] Traditional techniques using thin solid films of various materials, such as aluminum, carbon, and tin to transmit radiation limits the VUV spectrum from X rays (in the range of 0.01 to 10 nm) to about 70 nm. [3] Indium and LiF are suitable materials for thin solid windows for transmitting radiation greater than 80 nm in wavelength. [3] However, these thin solid windows, which are not fabricated as capillary arrays have drawbacks. Some of these windows can withstand only a small pressure differential, while some of them can only provide limited transmission over a relatively narrow spectral range especially above approximately 100 nm. [3] Previous work has shown that a microporous capillary-array window in conjunction with a VUV source at 104.8 nm and 106.6 nm in wavelength from an argon plasma can be used as a transmission window with roughly 50% transmission efficiency. [3,4,5] In this work, multiple capillary-array windows as well as thin solid films with a range of pore dimensions, thicknesses, and materials, will be investigated to see if

they can couple VUV radiation more effectively at the same wavelengths and other wavelengths while still holding a pressure differential between two systems.

On one hand, with a small pore size, a window will be able to slow the transmission of large particles, which makes it a protective layer to prevent damage to targets. On the other hand, making a comparison to solid windows, a thinner window with a large amount of open area should result in higher UV and VUV transmission, which makes it appropriate for several applications such as gas sensing or mass spectrometry. [6] Of course, there is a tradeoff with the highest-pressure differential such a window can support. The thicker and more porous the window is, the higher the pressure differential it can hold. However, the optical transmission will be limited when the thickness increases. but if it is more porous, it could be improved. Therefore, it is critical to find a balance between obtaining the optimal UV and VUV transmission while still holding a pressure differential. This indicates that it is important to know how to choose window dimensions, such as the pore diameter, the thickness, the open area, as well as other important factors, such as the wavelength of the incident radiation, the exposed area, and the incident angle of the radiation.

1.2 Hypothesis and tasks

We hypothesize that porous capillary-array windows and thin solid films will both be able to transmit UV and VUV, but that porous capillary-array windows will exhibit a better transmission efficiency than thin solid films while still holding a significant pressure differential between atmosphere and vacuum. The UV and VUV transmission efficiency of the capillary-array windows can be optimized by modifying the pore dimensions, percentage of open area, thickness of the window, total exposed area, as well as the incident angle and the wavelength of the UV and/or VUV. We also need to examine the total exposed area when doing the pressure tests to get an idea of how large it can be while still holding the pressure differential.

The following tasks will be undertaken to prove the above hypothesis. If confirmed, they will provide us with methods that can select optimized UV and VUV transmission properties over a given wavelength range using either/or capillary-array windows and thin solid-film windows.

1. To the gas-flow rates through capillary-array windows and solid windows, the pressure at break of the capillary-array windows, and optical transmission through them as a function of wavelength.
2. To design fractional-factorial experiments to reduce the number of trials for the UV and VUV transmission measurements while still letting us find the optimum choices of factors, which are, but not limited to: pore diameter, thickness, the percentage of opening area, the total exposed area, as well as the angle and the wavelength of incident radiation, will be undertaken.
3. To experimentally measure the UV and VUV transmission efficiency through both capillary-array windows and solid windows.

4. To evaluate the weight of each factor and each of their interactions and to estimate the effects of the factors. To use statistical models to analyze the results of the fractional-factorial design to estimate the combination of factors that output the optimized optical transmission through the capillary-array windows.
5. To experimentally measure the pressure differential across both capillary-array windows, and to test out the maximum pressure differential that one window can hold before break.

The organization of this document is as follows.

Chapter I defines the motivation, hypothesis, and tasks for this work.

Chapter II is the background for this work. It includes a brief overview of the capillary-array windows that will be used as the experimental samples. Next, a general introduction to the light source, ultraviolet (UV) and vacuum-ultraviolet (VUV), is presented. Finally, the applications of the capillary-array windows in the industry are presented.

Chapter III will look into the details of theoretical calculations of this work. The calculation of gas-flow rate through a capillary-array window and the pressure at break of a capillary-array window are included to estimate how much the pressure differential a given capillary-array window can hold. Next, the calculations of optical transmission through both capillary-array windows and thin solid windows as a function of wavelength and incident angle are presented and discussed.

Chapter IV introduces the experimental methods and setups used in this work. As many of the devices were built and methods were developed specifically for this work, characterization and design choices are presented and discussed. In details, the descriptions of a capillary-array window holder, the description of the UV source, and the configuration of an Electron Cyclotron

Resonance (ECR) system which generates plasma that will be used as the VUV source in this work are introduced. To enhance the ability of detecting signals, specific signal collection and digital-signal processing methods are also described and tested. Fractional-factorial-experimental-design methods are also introduced in this chapter to give us the experimental results with fewer data collected instead of taking all possible experiments.

Chapter V examines the optical transmission through both capillary-array window samples with several dimensional parameters, such as pore diameters, thickness and the open area ratio (OAR) of the window, as well we several system parameters such as the total exposed area, the wavelength and the incident angle of the radiation. The examinations on thin solid windows with the same parameters were also implemented so as to be compared with the capillary-array windows.

Chapter VI presents the statistical analysis on the experimental results of both optical transmission and pressure differential. The optimized responses, as well as the weighs of each factor and their interactions were determined by the statistical analysis.

Chapter VII examines the pressure differential across the same capillary-array window samples as those being used to measure the optical transmission. Maximum pressure differential over the window samples were obtained by breaking the samples.

Chapter VIII presents the conclusions drawn from this work as well as a discussion of the future work.

1.3 Reference

[1] M Armacost, P. D. Hoh, R. Wise, W. Yan, J. J. Brown, J. H. Keller, G. A. Halle, K. P. Muller, M. D. Naeem, S. Srinivasan, H. Y. Ng, M. Gutsche, A. Gutmann, B. Spuler, IBM J. Res. Dev. 43, 39 (1999)

[2] National Academy Press, Plasma processing of materials: scientific opportunities and technological challenges, Washington, D.C. (1991)

[3] T. Lucatorto B, T. J. Mcllrath, and J. R. Roberts, Appl. Opt. 18, 2505 (1979)

[4] J. D. Chatterton, G. S. Upadhyaya, J. L. Shohet, J. L. Lauer, R. D. Bathke, and K. Kukkady, J. Appl. Phys. 100, 043306 (2006).

[5] P. D. Chopra and D. W. O. Heddle, J. Phys. B 7, 2421 (1974)

[6] Artzi-Gerlitz, Reit, Kurt D. Benkstein, David L. Lahr, Joshua L. Hertz, Christopher B. Montgomery, John E. Bonevich, Steve Semancik, and Michael J. Tarlov. "*Fabrication and Gas Sensing Performance of Parallel Assemblies of Metal Oxide Nanotubes Supported by Porous Aluminum Oxide Membranes*." Sensors and Actuators B: Chemical 136, 1, 257 (2009)

Chapter 2 – Background

2.1 Capillary-array windows

A traditional technique for transmitting UV and VUV radiation while holding a high-pressure differential is using free-standing thin solid films with differential pumping. However, without the help of differential pumping, films ranging from thicknesses a few nanometers to several micrometers have several drawbacks which are: (1) limited spectral ranges that can be transmitted, and (2) limited pressure differentials can be withstood as reported by previous work.[1] In addition, some of these windows can be easily corroded and contaminated by oxidation and other reactions.

An alternative option is the use of capillary-array windows,[1] an example of which is shown in Figure 2.1, which allows VUV transmission and still holds a pressure differential. In Figure 2.1(a), the dimension of the capillary-array window is 2 x 2 cm in area. The pore size is 50 μm in diameter, which is not visible to the naked eye. An enlarged SEM photograph of this capillary-array window that allow us to see pores through the window is also shown in Figure 2.1(b). With the help of differential pumping, a higher-pressure differential between atmospheric pressure and low vacuum can be achieved for proper operation of various devices. Capillary-array windows with a range of pore sizes in addition to ranges of open area and thickness can provide us with broad spectral transmission capabilities in the VUV range while they are often able to separate higher pressure regions, as reported in previous work.[1]

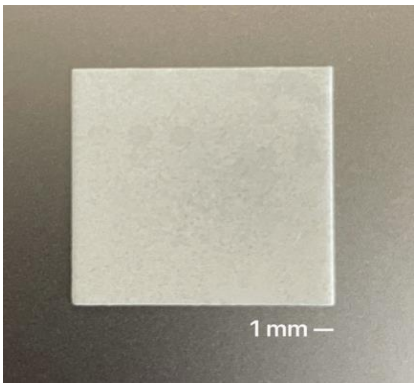

Figure 2.1(a). A capillary-array window sample

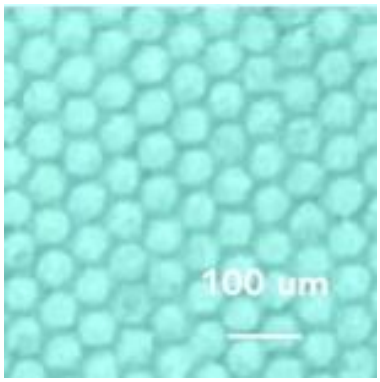

Figure 2.1(b). SEM photograph of a capillary-array window with 50 μm in pore diameter

As per J. D. Chatterton [1], a capillary array with 1 mm thickness, 20 μm in pore diameter and 53% in open area ratio was able to couple approximately 50% of the VUV with a wavelength in a range from 104 to 108 nm into a separate processing chamber with different pressure. Previous work also reported that capillary-array windows made of perforated stainless steel can transmit radiation at 121.6 nm although no details of the properties of the capillary arrays were given. [2] Here, we will explore the transmission of radiation over a wider range of wavelengths through capillary-array windows with different dimensions while still holding a pressure differential.

In this work, three categories of capillary-array windows, which are classified by the dimension of the pores, will be used. They are nanoporous windows [3], microporous windows [5], and milliporous windows, the latter produced with 3D printing.

2.1.1 Nanoporous capillary-array windows

The nanoporous capillary-array windows used in this work were manufactured by Smart Membranes GmbH and are made of alumina. The pores are etched to be parallel and completely straight through the alumina during the manufacturing process. A general layout of the film with some defined quantities is shown in Figure 2.2.

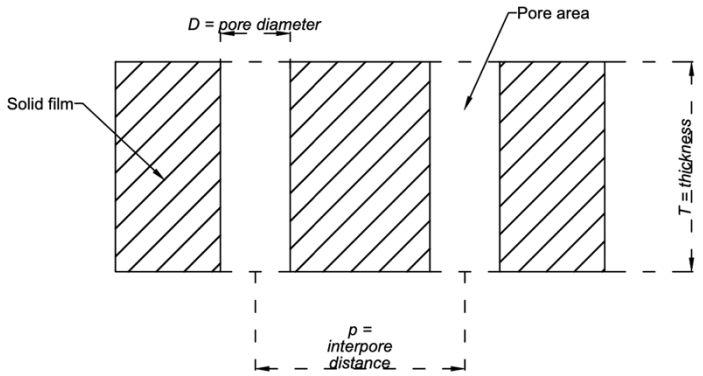

Figure 2.2. General layout of nanoporous alumina film

Figure 2.3 shows two SEM photographs of the capillary-array windows that were used in this project, which are SmartPor25 and SmartPor40. [3] Both of these two are straight-through capillary windows. The thickness, the porosity and the pore dimension of the windows are listed in Table 2.1 below.

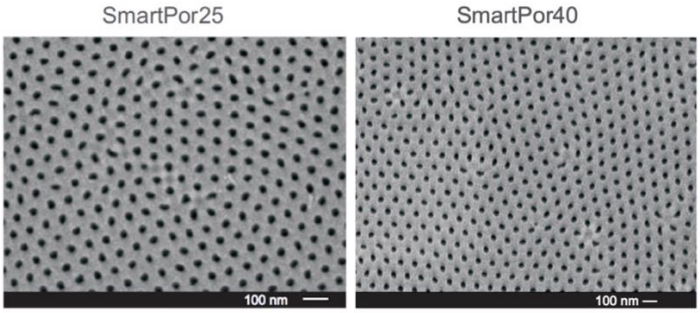

Figure 2.3. SmartPor25 and SmartPor40 [3]

Properties / Windows	Pore Diameter (nm)	Thickness (μm)	Interpore Distance (nm)	Porosity
SmartPor25	40	50	65	34.34%
SmartPor40	90	100	125	47.01%

Table 2.1. Nanoporous straight-through capillary-array window parameters [3]

As per K. Nielsch *et. al*, [4] formation of porous alumina using the anodization of aluminum method [4] will be able to fabricate an alumina window having well-arranged hexagonal arrays with circular pores in the center of each hexagon. The porosity of such a hexagonal structure, P in percentage, can be found using equation (2.1)

$$P = \frac{2\pi}{\sqrt{3}}\left(\frac{r}{D_{int}}\right)^2 \tag{2.1}$$

from reference 4, where r is the radius of the pores in nanometers and D_{int} is the interpore distance in nanometers.

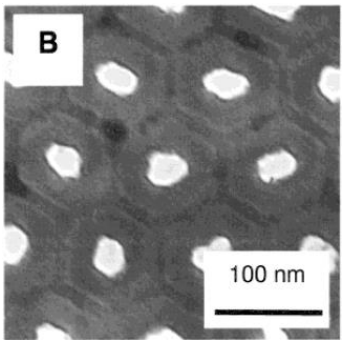

Figure 2.4. Hexagonal nanoporous cells with holes in the center of the hexagons [4]

2.1.2 Microporous capillary-array windows

The microporous capillary-array windows used in this work were fabricated by Collimated Holes, Inc. and made of borosilicate glass. [5] The etchable pores are individually straight through and parallel. The diameter variation along a capillary is typically less than 2%. [5]

Each individual capillary is treated as a unit cell, with the hollow part referred to as the core and the surrounding by the solid medium referred to as the cladding, which are both shown on Figure 2.5.

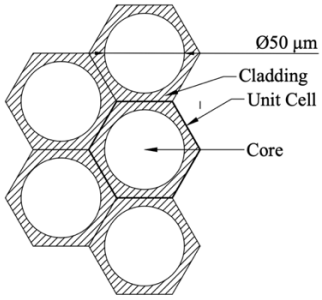

Figure 2.5. Core and Cladding

The open-area ratio (OAR) of a single pore is defined as the ratio of the cross-sectional surface area of the core to that of the entire cross-sectional surface area (core plus cladding). [5] Since the capillaries are evenly distributed along the entire fabricated window, the OAR of the entire window can then be calculated using the following universal expression [5] shown in equation (2.2)

$$OAR = \frac{A_{core}}{A_{core+clad}} \times 100\% = \frac{A_{open}}{A_{total}} \times 100\% \qquad (2.2)$$

where A_{open} represents the open area over the entire window, and A_{total} represents the entire area of the window.

The dimensions of the microporous capillary-array windows used are listed in Table 2.2 below. As will be discussed later, the reason why these four microporous windows were chosen for this work is to undertake the fractional-factorial experimental design, which will be introduced in Section 4.5 of Chapter 4.

An SEM photograph of CHS50T500 taken under the microscope is also shown in Figure 2.6.

Properties / Windows	Pore Diameter (μm)	Thickness (μm)	Porosity (%)
CHS50T500	50	500	60
CHS50T1000	50	1000	50
CHS25T500	25	500	50
CHS25T1000	25	1000	60

Table 2.2. Properties of microporous-glass capillary-array windows

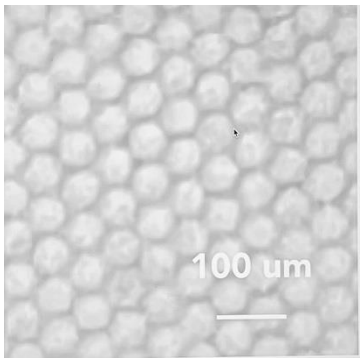

Figure 2.6. Hexagonal holes for glass microporous capillary-array windows

(Photo taken using an optical microscope)

2.1.3 Milliporous capillary-array windows

The resin used for 3D printing is a standard UV-curing photopolymer resin, Elegoo ABS, which is opaque, and UV "prohibited", so that it allows the incident light to be transmitted only through the pores rather than through the solid part of the window. However, to verify how much incident UV and VUV are transmitted through the cladding and how much is transmitted through the pores, the signal loss for transmission through solid 3D-printed windows with different thicknesses will also be measured.

The dimensions of the 3D-printed millimeter-porous capillary-array windows used in this work are listed in Table 2.3. Due to the resolution limit of the 3D printer (Elegoo Mars) that we are using, thinner windows and those with smaller pores cannot be made with this printer. Fortunately, a larger OAR can be achieved by adjusting the interpore distance if needed. (The 3-D printed capillary-array windows were made with the help of Josh Blatz, one of our colleagues in the lab.) In addition, the reason why we chose these parameters of the milliporous capillary-array windows is also due to the designs of the fractional-factorial experiments, which will be introduced in Section 4.5 of Chapter 4.

Properties / Windows	Pore Diameter (μm)	Thickness (μm)	Porosity
3D-1500DT1000	1500	1000	44%
3D-1500DT500	1500	500	20%
3D-1000DT1000	1000	1000	20%
3D-1000DT500	1000	500	44%

Table 2.3. 3D printed milliporous capillary-array window dimensions

2.2 Ultraviolet (UV) and Vacuum-Ultraviolet (VUV) radiation

Optical radiation within the electromagnetic spectrum includes ultraviolet (UV) radiation, visible light, and infrared radiation. UV is defined as that radiation between 100 and 400 nanometers (nm) in wavelength.[6] It is characterized further according to wavelength into long-wave UV (UV-A, 315-400 nm), medium-wave UV (UV-B, 280-315 nm), short-wave UV (UV-C, 200-280 nm), vacuum-ultraviolet (VUV, 100-200 nm), extreme-ultraviolet (EUV, 10-121 nm) etc. [7]

UV radiation is present in sunlight and constitutes about 10% of the total electromagnetic radiation output from the sun. [7] It can be also produced by electric arcs and specialized lights, such as mercury-vapor lamps, tanning lamps, and black lights. [7] The UV radiation that was used in this work is in the range of short-wave UV (UV-C, 200-280 nm), and it is produced by a low-pressure, cold-cathode mercury UV Pen- Ray lamp.

More energetic, vacuum-ultraviolet (VUV, 100-200 nm), ionizes gases so strongly that is mostly absorbed by atmospheric oxygen, while 150-200 nm wavelengths can propagate through nitrogen. [7] Therefore, when detecting the VUV radiation, it is preferred to operate in high-vacuum chambers, or at least in an oxygen-free atmosphere. In this work, the VUV radiation is produced in a vacuum chamber under 20 mTorr by plasma, and the pressure of VUV radiation detecting system is controlled under 10^{-6} torr so that most of the VUV radiation can propagate in the chambers without being absorbed.

Because of its ability to cause chemical reactions and excite fluorescence in materials, ultraviolet radiation has a number of applications in some specific wavelength bands. For example, in the range of 200-400 nm wavelength, UV radiation can be used in disinfection, decontamination of surfaces and water, protein analysis, medical imaging of cells, and various optical sensors. [7] In the semiconductor industry, both the UV and VUV in the range of 30-200 nm wavelength can be used in multiple applications, such as photoionization, ultraviolet photoelectron spectroscopy, and standard integrated circuit manufacture with photolithography, [8] a general term used for techniques that use this radiation to produce patterned thin films of suitable materials over a substrate, such as a silicon wafer, and to protect selected areas of it during subsequent etching, deposition, or implantation operations in integrated circuit manufacturing. Very importantly, the wavelength of radiation used determines the minimum feature size of the integrated circuit.

2.3 Applications of capillary-array window

The capillary-array window has many applications in industry including semiconductor techniques, biotech engineering, and material science. Capillary-array windows can be used for time of flight (TOF) mass spectrometry, neutron detection, microfluidic analysis and so on. [9]

In addition, a method called capillary electrophoresis (CE) [10], uses capillary-array windows to separate ions based on their electrophoretic mobility with an applied voltage. Since the electrophoretic mobility of an ion depends on the charge, the viscosity and the size of the ion, and the rate at which the ion moves being proportional to the intensity of the applied electric field, we have the following facts: (1) the greater strength of the electric field, the faster the ion moves. (2) For two ions with the same charge, but different masses, the smaller one moves faster and exhibits less friction. (3) For two ions of the same mass, the one with greater charge moves faster. [11] Capillary-array windows also have an advantage because of their thin dimensions, which greatly increases its surface to volume ratio, so that it helps to reduce the overheating on one side of the window introduced by a high voltage in capillary electrophoresis (CE). [11]

In the semiconductor industry, capillary-array windows can be also used to minimize charged-particle bombardment effects during plasma processing while letting the plasma generating optical radiation through. Since the charged-particle bombardment effects can likely damage the wafer while photons are being transmitted as well, such as the process of dry etch in the photolithography, in this work, we investigated the effectiveness of the capillary-array windows to partially block the charged particles while still let the photons through.

2.4 Reference

(1). T. Lucatorto B, T. J. Mcllrath, and J. R. Roberts, Appl. Opt. 18, 2505 (1979)

(2) P. D. Chopra and D W O Heddle 1974 *J. Phys. B: Atom. Mol. Phys.* **7** 2421

(3). Smartmembrans GmbH, "SmartPor Nanoporous Alumina FactSheet" Heinrich-Damerow-Str. 4, 06120 Halle, Germany

(4). K. Nielsch, J. Choi, K. Schwirn, R. B. Wehrspohn, U. Gosele, "Self-ordering Regimes of Porous Alumina: The 10% Porosity Rule", American Chemical Society, Nano Let., 2, 677 (2002)

(5) "*Collimated holes product information*" , 2021. Accessed on: April. 27th, 2021. [Online]. Available: http://www.collimatedholes.com/products.html

(6). Richard P. Gallagher, Tim K. Lee, Chris D. Bajdik and Marilyn Borugian, "Ultraviolet radiation", Chronic Diseases in Canada, Supplement 1, Vol 29, 51 (2010)

(7) "*Ultraviolet*", July 26th, 2022. Accessed on: August. 30th, 2022. [Online]. Available: https://en.wikipedia.org/wiki/Ultraviolet

(8) "*Photolithography*", August 23th, 2022. Accessed on: August. 30th, 2022. [Online]. Available: https://en.wikipedia.org/wiki/Photolithography

(9) "*Glass capillary array*", 2022. Accessed on: August. 30th, 2022. [Online]. Available: https://incomusa.com/glass-capillary-array/

(10). F Tagliaro, G Manetto, F Crivellente, F.P Smith, "A brief introduction to capillary electrophoresis", Forensic Science International, Volume 92, Issues 2–3, 75-88 (1998)

(11) "*Capillary Electrophoresis*", July 8th, 2022. Accessed on: August. 30th, 2022. [Online]. Available: https://chem.libretexts.org/Bookshelves/Analytical_Chemistry/Supplemental_Modules_(Analytical_Chemistry)/Instrumental_Analysis/Capillary_Electrophoresis

Chapter 3 – Theoretical Calculations

The capillary-array windows are primarily used here to separate the low-pressure (from 0.001 to 0.1 mTorr) region from relatively high pressure (~20 mTorr) where a VUV source is located while allowing transmission of radiation between regions. Therefore, to determine if a capillary-array window is compatible for this purpose, two parameters need to be considered, which are (1) the pressure differential that can be supported by the window and (2) the optical transmission through the window.

To calculate how much pressure differential a capillary-array window can hold, it is necessary to calculate the gas-flow rate through the capillary-array windows and compare it with the pumping speed.[1] Then, it is also important to know the maximum pressure differential a capillary-array window can hold before failure.

In addition, the calculation of optical-transmission efficiency is needed to determine how much radiation can be transmitted and whether it is optimized for maximum transmission while holding a given pressure differential. To compare the transmission through a capillary-array window made with a solid film that has the same thickness, the optical transmission through solid films will also be calculated in this chapter to develop more reference results for comparison.

3.1 Calculation of gas-flow rate and pressure at break of a capillary-array window

3.1.1 Gas-flow rate

In general, there are three types of gas flow considered in a vacuum system regarding the pressure level. They are viscous flow, transition flow, and molecular flow. [2] Viscous flow occurs at the higher pressures, where the mean free path $\Lambda < 0.09D$, where D represents the diameter of a tube. Under viscous-flow conditions, the gas molecules are colliding with each other more frequently than with the surfaces of the tubes. [2] Under viscous flow, there are two other conditions, turbulent and laminar flow. There is a number, called the Reynolds number, that can be used to determine whether a viscous flow is laminar or turbulent. [4]

The Reynolds number is dimensionless and is defined as [5]

$$\text{Rey} = \frac{v\rho D}{\mu} = 21.2\,\frac{\rho Q}{\mu D} \tag{3.1}$$

where v is the fluid velocity in (m/s), ρ is the fluid density in $(kg/\,m^3)$, D is the diameter in (mm) of the tube, and μ is the dynamic viscosity in $(kg/m\cdot s)$. The fluid velocity is defined as $v = q/A$ with flow rate q in units of (m^3/s), and the tube cross-section $A = \pi(D/2)^2$. The fluid velocity is then calculated to be $v = 21.2\,Q/D^2$ with volumetric flow rate Q in liters per minute (lpm). Therefore, the Reynolds number is calculated to be $\text{Rey} = 21.2(\rho Q/\mu D)$. When the Reynolds number is less than 2300, the flow is in the laminar regime, when the Reynolds number goes over 2300 and less than 4000, it is in the transition regime, and when the Reynolds number is greater than 4000, it is in the turbulent regime. [6] In this work, we used argon gas, which has the density $\rho_{Ar} = 1.86\ (kg/\,m^3)$, and the dynamic viscosity $\mu_{Ar} = 2.22\times10^{-5}\ (kg/m\cdot s)$. Thus, in our case, we have $\text{Rey}_{Ar} = 1780\ (Q/D)$ in our case in terms of the gas flow rate Q in liters per

minute (*lpm*) and the tube diameter D in (*mm*). When the pressure drops still further and the gas flow reaches the lower end of the viscous-flow regime, there is a region where the flow changes from viscous flow to molecular flow. This does not occur at a fixed spatial point. Instead, it transitions from one flow to the other. This region is called the transitional-flow region, and it occurs when $0.09D < \Lambda < D$, where Λ is the mean free path and D represents the diameter of the tube in meters. [2] At the lower-pressure regime, when $\Lambda \gg D$, the gas flow changes to molecular flow. The majority of the molecules do not actually flow straight-through the tube. Instead, the gas molecules collide with the inner surfaces of the tube more often than they collide with other gas molecules. Therefore, the type of flow will be dependent on the magnitude of the pressure differential through a tube. [2]

A capillary-array window can be treated as a window consisting of multiple tubes in parallel. The diameter of the tubes can be in the range of millimeters, micrometers or even nanometers. For calculating the gas-flow rate through an entire window, we can start with a single tube. [7]

The gas flow $Q_1\ (torr \times Liter \times sec^{-1})$ and the gas flow rate $R_1(cm^3 \times sec^{-1})$, over a wide range of conditions, through a single tube of diameter D (cm) and length L (cm) with a pressure P_1 at the high-pressure end and P_2 at the low-pressure end can be calculated by using the expression [7]

$$Q_1\ (torr \times Liter \times sec^{-1}) = \frac{133 \times 75^2 \times 10^{-6} \pi D^4}{128 \eta L} P_{av}\ \Delta P + 10^3 K\ \left(\frac{1 + K_1 D P_{av}}{1 + K_2 D P_{av}}\right) \frac{D^3}{L}\ \Delta P \qquad (3.2a)$$

$$R_1\ (cm^3 \times sec^{-1}) = \frac{\pi P_{av} D^4}{128 \eta L} + \frac{K D^3}{L} \left(\frac{1 + K_1 D P_{av}}{1 + K_2 D P_{av}}\right) \qquad (3.2b)$$

where $P_{av} = (P_1 + P_2)/2\ (torr)$, $\Delta P = P_1 - P_2\ (torr)$, and η is the viscosity of the gas in poises. $\eta_{air} \sim 1.85 \times 10^{-5}\ (Pa \cdot s)$ and. $\eta_{argon} \sim 2.27 \times 10^{-5}\ (Pa \cdot s)$. [18] The constants K, K_1, K_2 are determined with the following three expressions [7]

$$K = \frac{\sqrt{\pi}}{6}\sqrt{\frac{2kT}{m}} \qquad (cm/sec) \tag{3.3}$$

$$K_1 = \frac{7.5 \times 10^{-4}}{\eta}\sqrt{\frac{m}{kT}} \qquad (torr \times cm)^{-1} \tag{3.4}$$

$$K_2 = \quad 1.24K_1 \tag{3.5}$$

where *m* is the molecular mass in grams, *k* is Boltzmann's constant in joules, and *T* is the temperature in degrees *K*, given a room temperature at 300 *K*.

In equation (3.2a), the first term represents the pressure-dependent viscosity flow, which will dominate at higher pressures, and the second term represents molecular flow, which dominates as the average pressure $P_{av} \to 0$. As mentioned, the region that is between the viscous-flow regime and the molecular flow regime is the transitional-flow region. The pressure in the transitional-flow region, where these two terms are roughly equal, is called the transition pressure, and the relationship between the diameter *D* of the tube and the mean free path Λ_{tr} at the transition pressure is given by [7]

$$\Lambda_{tr} = 0.09D \tag{3.6}$$

From the different working conditions of the three gas-flow types mentioned above, the gas flow is the greatest in the viscous-flow region because the gas density is the highest, and the smallest in the molecular-flow region, and in between for the transition-flow region. [3]

Thus, calculating the gas flow of a single tube will help us to understand in which pressure regime the flow along the tube will be. After that, to estimate the total gas flow of the capillary-array window, we need to know the number of tubes *N* in an array of area *A*, which is given by:

$$N = (OAR \times A)/(\pi(D/2)^2) \tag{3.7}$$

where OAR is the open area ratio defined in equation (2.2) in Chapter 2. Therefore, from equations (3.2a) and (3.7), the total gas flow of the array can be obtained by: [7]

$$\begin{aligned} Q_{total\_1} &= Q_1 \times N \\ &= N\frac{133 \times 75^2 \times 10^{-6}\pi D^4}{128\eta L} P_{av}\,\Delta P + 10^3 NK \left(\frac{1 + K_1 D P_{av}}{1 + K_2 D P_{av}}\right)\frac{D^3}{L}\,\Delta P \\ &= \frac{OAR \times A \times D \times \Delta P}{L}\left[\frac{133 \times 75^2 \times 10^{-6} D}{32\eta} P_{av} + \left(\frac{1 + K_1 D P_{av}}{1 + K_2 D P_{av}}\right)\frac{10^3 K}{\pi}\right] \end{aligned} \tag{3.8}$$

From equation (3.8), we notice that the gas flow is proportional to the product of the total open area *A*, the open-area ratio *OAR*, the diameter *D*, and the pressure differential divided by the length *L* which is in turn multiplied by the pressure-dependent term, which can be expressed as a function of $P_{av}D$ by

$$f(P_{av}D) = \frac{133 \times 75^2 \times 10^{-6}}{32\eta} P_{av}D + \left(\frac{1 + K_1 D P_{av}}{1 + K_2 D P_{av}}\right)\frac{10^3 K}{\pi} \tag{3.9}$$

Therefore, with *OAR*, *A*, *D* and *L* being constants, the conductance and $f(P_{av}D)$ are positively related, which means low gas-flow will be achieved when $f(P_{av}D)$ is low.

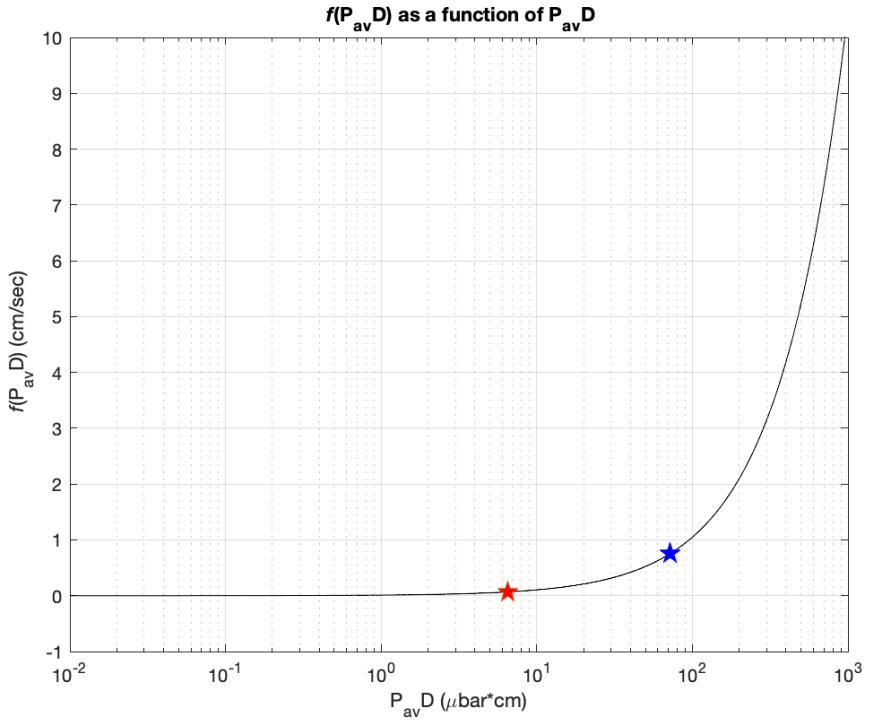

Figure 3.1. $f(P_{av}D)$ as a function of $P_{av}D$

In our case of using argon at the room temperature 300 K, Figure 3.1 shows $f(P_{av}D)$ is plotted as a function of $P_{av}D$. Noticed that the unit of $P_{av}D$ is $\mu bar * cm$. In Figure 3.1, the red star represents the spot where $\Lambda = D$, and the blue star represents the spot where $\Lambda = 0.09D$. Therefore, the left side of the red star is where the molecular-flow regime is located. To the right side of the blue star is where the viscous-flow regime is located. The region between the stars is the transitional-flow regime. From Figure 3.1, we can see the low $f(P_{av}D)$ is achieved in the molecular-flow region, where the condition $\Lambda \gg D$ is applied.

Then, the total gas flow Q_{total_2} through a capillary-array window with molecular flow dominating as $P_{av} \to 0$ now becomes:

$$Q_{total\_2}\,(torr \times Liter \times sec^{-1}) = \frac{OAR \times A \times \Delta P}{L}\left(\frac{1 + K_1 D P_{av}}{1 + K_2 D P_{av}}\right)\frac{10^3 KD}{\pi}$$

$$= 10^3 KD \frac{OAR \times A \times \Delta P}{\pi L} \tag{3.10}$$

The same analysis can be also applied to the calculation of the total gas-flow rate through the entire capillary array. From equations (3.2b) and (3.7), the total gas flow rate R_{total_1} through the capillary array can be obtained by

$$R_{total\_1} = R_1 \times N = N\frac{\pi P_{av} D^4}{128\eta L} + \frac{NKD^3}{L}\left(\frac{1 + K_1 D P_{av}}{1 + K_2 D P_{av}}\right)$$

$$= \frac{OAR \times A \times D}{L}\left[\frac{P_{av} D}{32\eta} + \frac{4K}{\pi}\left(\frac{1 + K_1 D P_{av}}{1 + K_2 D P_{av}}\right)\right] \tag{3.11}$$

Then, the total gas-flow rate R_{total_2} through a capillary-array window with molecular flow dominating as $P_{av} \to 0$ can be calculated by

$$R_{total\_2} = \frac{4K \times OAR \times A \times D}{\pi L} \tag{3.12}$$

Besides using a solid window to sustain a high pressure differential, if we want a capillary-array window to sustain a high-pressure differential with minimum pumping requirements, this requires a low gas-flow rate (R_{total_2}). One way to achieve this is to choose a small tube diameter, a smaller *OAR*, or a long tube length. This length is equal to the thickness of the capillary-array window since the tubes are straight through the window, to assure operation in the molecular-flow region.

Therefore, with the total gas flow Q_{total_2} and the total gas-flow rate R_{total_2} through a capillary-array window shown in equations (3.10) and (3.12), as well as a given pumping speed, we will be able to know if the capillary-array window is able to hold a pressure differential and what the dominant gas-flow type is occurring inside the tubes.

In our ECR system, which will be introduced in Chapter 4, the pressure on one side of the capillary-array window is about 2×10^{-2} Torr, controlled by the pumping rate of a mechanical

pump, a turbo pump, as well as the feed-in gas rate of a mass-flow controller to feed in the argon gas to the chamber that produces VUV radiation. On the other side of the capillary-array window, the pressure is about 10^{-6} Torr, which is controlled by another mechanical pump and turbo pump. Thus, the estimated pressure drop is about 2×10^{-2} Torr when we do the measurements of the VUV radiation transmission.

From equation (3.12), using a milliporous capillary-array window with 1 mm in pore diameter, 1 mm in thickness, OAR 20%, and a total exposed area with 5 mm in radius as an example, the total pumping rate needed for maintaining a pressure differential between 2×10^{-2} and 10^{-6} torr is calculated to be 0.0074 m^3/h. Using the same capillary-array window to hold a pressure differential between atmospheric pressure at 760 torr and a vacuum under the pressure at 2×10^{-2} torr with a total exposed area with 5 mm in radius as an example, the total pumping rate needed for maintaining the pressure differential is calculated to be 36.3032 m^3/h. As will be mentioned in Chapter 4, the mechanical pump that is used in our system can provide with a pumping rate of 110 m^3/h. This means that the gas-flow rate calculated by the above examples for maintaining the pressure differential through the milliporous capillary-array window is in the normal operating range of the mechanical pump. Therefore, the milliporous capillary-array window mentioned above is able to hold the pressure differential.

In addition, as the microporous and nanoporous capillary-array window samples used in this project have much smaller pore diameters and similar thicknesses to the milliporous capillary-array window, when substituting their dimensions to the calculation, the gas-flow rate turns out to be much smaller than the pumping rate provided in our system in the range of 10^{-5} m^3/h. Therefore, we can draw the conclusion that all capillary-array windows used in our

project can sustain the pressure differential mentioned above with the mechanical pump operating in the normal condition.

3.1.2 Pressure at Break

It is challenging to make an accurate calculation for the maximum pressure differential a capillary-array window can withstand before failure, which is called pressure at break, because the maximum pressure differential a capillary-array window can withstand depends on the specific characteristics of the material, the dimensions of the capillary-array window, and the manufacturing process used to produce it. For example, the microstructure of the capillary-array window, the distribution of the pores, manufacturing method, defects, and any other post-processing steps and other forms of material degradation that may have happened will all affect the exact mechanical properties of the porous materials.

In general, the following factors need to be considered when calculating the maximum pressure differential that a capillary-array window can withstand before failure.

(1) Pore size: The maximum pressure differential that a capillary-array window can withstand generally increases with decreasing pore size. However, excessively small pore sizes can lead to clogging and reduced permeability, which can reduce the overall effectiveness of the window.

(2) Thickness of the capillary-array window: The maximum pressure differential that a capillary-array window can withstand generally increases with increasing thickness. However, excessively thick windows can be more brittle and prone to cracking or shattering, especially if the material is not uniform or has internal defects. [20]

(3) Density of the capillary-array window: The maximum pressure differential that a capillary-array window can withstand generally increases with increasing density. However, excessively high-density windows may also be more brittle and prone to cracking or shattering under stress. [20] The density of the capillary-array window can be determined

by the porosity, or open area ratio (OAR), of the window, because the capillary-array window made of Alumina (Al_2O_3) as an example, can be considered as a combination of Alumina and air.

(4) Microstructure and composition of the material: These can affect the mechanical properties of the capillary-array window, such as strength, elasticity, and toughness, and therefore impact its ability to withstand pressure differentials.

(5) Manufacturing process: The manufacturing process used to produce the capillary-array window can affect its microstructure, composition, and overall quality, which can impact its strength and ability to withstand pressure differentials.

(6) Operating conditions: The specific operating conditions of the application, such as temperature, pressure, and chemical environment, can also impact the strength and integrity of the window material and its ability to withstand a pressure differential.

(7) Loading conditions: The way in which the pressure is applied to the capillary-array window can also affect its ability to withstand pressure differential. For example, cyclic loading, high impact loading, or loading from multiple directions can all impact the window's strength and ability to withstand pressure differential. [20]

In industry, a wide range of mechanical testing methods can be used to measure the behavior of a porous material under different stresses directly, using techniques such as compressive testing, Brazilian disc testing, and 3-point bending test. [20] From these methods, we can obtain the stress-strain curve, which describe the relationship between the magnitude of the force applied to the unit area of the material and the deformation (strain) caused by the force. The measurements and the data collection can be performed using an Instron 8562 and Bluehill software, [20] which records

the loadings and measures the deformation. For example, applying a quasistatic compression test, the stress can be calculated from the ratio of the actual load to the cross-sectional area, and the strain can be obtained by measuring the displacement of the crosshead. [20] Therefore, to obtain the most accurate theoretical calculation of the maximum pressure differential that a capillary-array window can withstand before failure without a mechanical testing can be complex.

However, from what has been discovered in previous work, [20], [22], [23] there is a method for an approximate estimation of the maximum pressure differential a capillary-array window can withstand before failure with considering the following factors (1) Pore size of the capillary-array window; (2) Thickness of the capillary-array window; (3) Relative density of the capillary-array window.

Assuming that (1) The pores are distributed uniformly throughout the capillary-array window; (2) The window is under uniaxial stress; (3) The pressure differential is evenly applied to the surface of the capillary-array window, which means the exposed area is not considered in the estimation. With the assumption listed above, the estimation of the maximum pressure differential a capillary-array window can withstand before failure can be determined by

$$\Delta P\ (psi) = \ 18.1979 \times \frac{Den \times T^2}{Dia} + 67.1989 \qquad (3.13)$$

where ΔP is the maximum pressure differential in psi of a capillary-array window can withstand before failure, *Den* is the relative density in $\mathrm{g/cm^3}$ of the capillary-array window made of Alumina (Al_2O_3), T is the thickness in cm of the capillary-array window, and *Dia* is the pore diameter in cm of the capillary-array window. It should be noted that equation (3.13) is a fitted equation obtained from the previous work. [20], [22], [23]

Using the microporous capillary-array windows that have been explored in our project as an example, when applying the equation (3.13) to calculate the maximum pressure differential that these microporous capillary-array windows can withstand before failure, the results of the calculation are shown in Table 3.1 below.

Catogery	Diameter	Thickness	OAR	Relative Density (g/cm3)	Pressure At Break (Psi)
Microporous	25 μm	500 μm	50%	1.976	103.165
	25 μm	1000 μm	60%	1.581	182.283
	50 μm	500 μm	60%	1.581	81.584
	50 μm	1000 μm	50%	1.976	139.120

Table 3.1 Calculation results of pressure at break for microporous capillary-array windows

However, the accuracy of equation (3.13) may depend on other factors, such as the geometry and distribution of the pores, the manufacturing process of the capillary-array window, and the operating conditions under which the capillary-array window is being used. Therefore, equation (3.13) should be considered an estimate. To obtain a more accurate estimate, it may be necessary to perform additional mechanical tests or simulations to evaluate the specific performance characteristics of the capillary-array window. Therefore, physical pressure tests have been implemented for the capillary-array windows, and the experimental results will be presented in Chapter 7 to see how they match the estimation.

3.2 Calculation of optical transmission

In addition to the gas flow through the window and the maximum pressure a capillary-array window can hold before failure, the optical transmission of a capillary-array window consisting of multiple tubes of inner diameter *D* and the length *L* also needs to be calculated. In this work, the following assumptions and approximations have been made for calculating the optical transmission:

(1) Here we consider two light sources, (a) the UV radiation at 253 nm from a mercury UV Pen-Ray lamp and (b) the VUV radiation at 104.8 nm and 106.6 nm from the ECR plasma, which will be introduced in Section 4.1.2 and 4.1.3, respectively. We assume that each of the light sources is a combination of individual point sources, and each individual point source emits spherical waves.

(2) We assume that the spherical wave becomes a plane wave when it hits the capillary-array window. The reason is that the distance between the light source and the capillary-array window is 50 cm, while the wavelength of the radiation of interest is about 100 to 300 nanometers, so the curvature of the wavefront is very small when it hits the capillary-array window. This assumption applies to all the capillary-array windows in our experiment.

(3) We consider the condition that there is an angle between the direction of the propagation of the incident radiation and the capillary-array window surface.

(4) For the capillary-array windows, there are holes (pores) that are defined as nanoporous, microporous, and milliporous. Since the wavelength of the radiation that we are considering is in the UV and VUV range, which is 100 to 300 nm, we calculate the optical transmission through nanoporous windows using wave optics, while we calculate the optical transmission through both microporous and milliporous windows using ray optics because the wavelengths

we are interested in are much smaller than the size of the pores in these microporous and milliporous capillary-array windows.

3.2.1 Calculation of optical transmission through thin solid windows

Before calculating the optical transmission through capillary-array windows with a range of pore sizes, thicknesses, and open areas, etc., we start with the calculation of optical transmission through solid windows to give a reference for how much radiation can transmit through a solid window of a given thickness without any pores. Therefore, when calculating the optical transmission through the capillary-array windows, we can focus on the radiation that only transmits through the pore area.

To calculate how much radiation can be transmitted through a thin solid window, we need to consider the following things:

(1) Reflection at the interface of the free space and the window surface. We need to calculate how much radiation is reflected when it first hits the surface of the solid window.

(2) Propagation loss inside the solid material. The radiation that is successfully transmitted through the interface of the free space and the solid window is going to propagate through the solid material of the window. Because the window is made of dielectric material, that has some loss, then when the radiation propagates through the inside of the solid window, the signal will decrease in amplitude.

(3) Reflection at the interface of the solid window and the free space. When the radiation gets to the end of the solid window, the reflection occurs again, and thus only part of the radiation is transmitted to free space.

3.2.1.1 Reflection at the input interface of free space and the window surface

To start with, the reflection at the input of the window from free space needs to be considered. Let P_{window} be the total power of the incident radiation hitting on the entire solid window.

Applying the law of conservation of energy, the radiated power from a light source can be expressed as

$$P = \int \vec{S} \cdot \, d\vec{A} \tag{3.14}$$

Where $\vec{S}$ is the Poynting vector of the incident radiation as a function of position, and $d\vec{A}$ is a vector differential area element of the solid window surface. Since the solid window is cuboid, we use a rectangular coordinate system as shown in Figure 3.2 to calculate the power that hits the entire solid window.

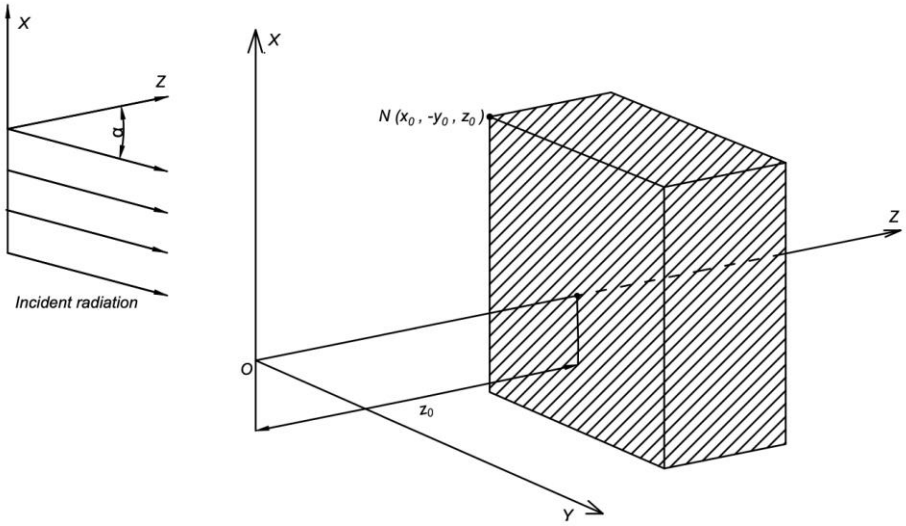

Figure 3.2. Rectangular coordinate system for the solid window

In the rectangular coordinate system shown in Figure 3.2, the origin O is also where the light source is. The Z axis goes through the center of the solid window, and z_0 is the distance between the light source and the solid window. We assume the width of the window to be $2x_0$ and the height of the window to be $2y_0$, therefore the area of the cross-section of the solid window is $4x_0y_0$.

Here, shown in Figure 3.2, we consider that there is an incident angle α on the X-Z plane between the direction of the propagation of the radiation and the surface of the solid window. When the incident angle α is zero, the incident radiation propagates along the Z axis, which means that the incident radiation is perpendicular to the solid window.

Since we have also assumed that the radiation becomes a plane wave at the window surface, which means the power density is uniform over the entire solid window. Therefore, the total power of the incident radiation hitting on the solid window surface, $P_{window\_entrance}$, can be expressed as

$$\begin{aligned} P_{window\_entrance} &= \int \vec{S} \cdot d\vec{A} \\ &= \int_{-x_0}^{x_0} \int_{-y_0}^{y_0} (\vec{S} \cdot \hat{n}) dx dy \\ &= \int_{-x_0}^{x_0} \int_{-y_0}^{y_0} |\vec{S}| (\hat{s} \cdot \hat{n}) dx dy \\ &= |\vec{S}| \int_{-x_0}^{x_0} \int_{-y_0}^{y_0} (\hat{s} \cdot \hat{n}) dx dy \\ &= 4x_0 y_0 |\vec{S}| \cos\alpha \end{aligned} \tag{3.15}$$

In equation (3.15), $\vec{S}$ is the Poynting vector, and $d\vec{A}$ is a vector differential area element of the solid window surface. $|\vec{S}|$ is the power density in the unit of $watts/m^2$, $\hat{n}$ represents the unit vector normal to the solid window surface, and $\hat{s}$ represents the unit vector of the incident Poynting vector. The dot product of $\hat{s}$ and $\hat{n}$ becomes $\cos\alpha$ because there is an incident angle α between the Z-axis and the direction of the propagation of the radiation. The power density $|\vec{S}|$ is a constant because the plane wave has a uniform power density over the entire capillary-array window surface.

After finding $P_{window\_entrance}$ from equation (3.15), which is the total power of the radiation incident on the entire solid window, we need to calculate how much radiation is reflected and how much radiation is transmitted through the interface of the free space and the solid window surface.

Figure 3.3 shows the reflection and the transmission occurring at the interface of free space and the solid window. The incident radiation comes from the upper left, and the reflected radiation goes to the lower left. The transmitted radiation into the solid window goes to the lower right. Here, θ_i is the incident angle, θ_r is the reflected angle, and θ_t is the transmitted angle. n_1 is the refractive index of air in the free space, which is on the outside of the solid window, and n_2 is the refractive index of the material that the solid window is made of, which is alumina in our case.

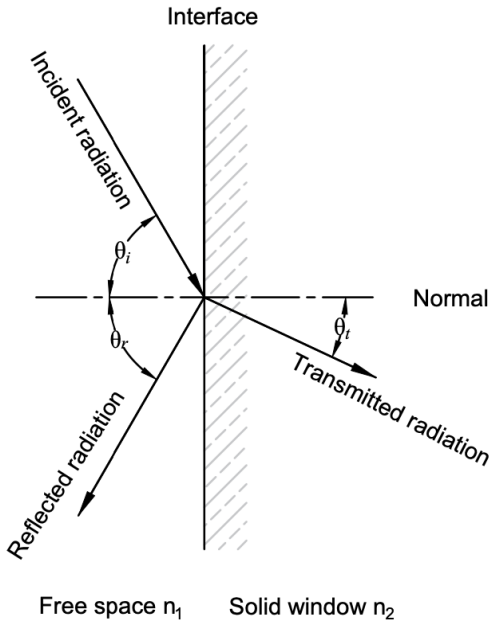

Figure 3.3 Reflection and transmission occur at the interface

Here, we define the reflectance as $R_{re\_entrance}$ to represent how much radiation will be reflected back to free space after the scattering occurs at the interface of the free space and the entrance to the solid window, and the transmittance $T_{tr\_entrance}$ to represent how much radiation is transmitted into the solid window. Starting from the Snell's law of reflection, [8] we have

$$\theta_r = \theta_i \tag{3.16}$$

where θ_i represents for the incident angle of the radiation, and θ_r represents for the reflected angle of the radiation. From the Snell's law of refraction, [8] we have

$$n_1 \sin\theta_i = n_2 \sin\theta_t \tag{3.17}$$

where θ_t is the transmitted angle. n_1 is the refractive index of air in the free space, and n_2 is the refractive index of the material of the solid window.

In our case, the solid window is made of alumina, and we are considering the VUV radiation at 105 nm in wavelength and UV radiation at 253 nm in wavelength. The refractive index of alumina is approximately 1.92 at 104.8 nm in wavelength, 1.97 at 106.6 nm in wavelength and 1.76 at 253 nm in wavelength. [15] With the refractive index of air in the free space, n_1, is considered 1.0, total internal reflection will not occur when the radiation enters the solid window from free space because the refractive index of alumina at either wavelength is greater than the refractive index of air in the free space. However, when the radiation incidences at Brewster angle, [16] it will be perfectly transmitted through the dielectric window surface with no reflection. The Brewster angle is determined by [16]

$$\theta_B = \tan^{-1}\left(\frac{n_2}{n_1}\right) \tag{3.18}$$

where n_2 is the refractive index of the alumina, and n_1 is the refractive index of air in the free space. Given the refractive index of alumina at these wavelengths, we have

$$\theta_B = 62.5° \quad (\lambda = 104.8\ nm)$$

$$\theta_B = 63.1° \quad (\lambda = 106.6\ nm)$$

$$\theta_B = 60.4° \quad (\lambda = 253.6\ nm) \tag{3.19}$$

Therefore, when the incident radiation at certain wavelengths with the corresponds to the Brewster angle listed in equation set (3.19) from the free space, it will be perfectly transmitted into the solid window without any reflection.

Now, besides the Brewster's angle, if the radiation is incident at other angles, a more general case comes from the Fresnel equations, $R_{re\_entrance}$ and $T_{tr\_entrance}$ can be determined by [14]

$$R_{re\_entrance} = \left| \frac{n_1 \cos\theta_i - n_2\sqrt{1 - \left(\frac{n_1}{n_2}\sin\theta_i\right)^2}}{n_1 \cos\theta_i + n_2\sqrt{1 - \left(\frac{n_1}{n_2}\sin\theta_i\right)^2}} \right|^2 \tag{3.20}$$

$$T_{tr\_entrance} = 1 - R_{re} \tag{3.21}$$

Therefore, given an incident angle $\theta_i = \alpha$ and from the equations (3.20) and (3.21), we can determine both the transmittance and the reflectance when the incident radiation hits the solid window surface from free space. Since the total power of the incident radiation hitting on the solid window surface, $P_{window\_entrance}$, has been given in equation (3.15), the power of the radiation that enters the solid window after the scattering occurs at the interface, P_{window_in}, can be determined by

$$P_{window\_in} = T_{tr\_entrance} P_{window\_entrance} \tag{3.22}$$

In addition, if the incident angle is at the Brewster angle, then the power of the radiation that enters the solid window, $T_{tr\_entrance}$ in equation (3.22) will be considered equal to 1.0, and then

$$P_{window\_in} = P_{window\_entrance} \tag{3.23}$$

3.2.1.2 Propagation inside the solid window

After the radiation gets into the solid window, there will be some loss during its propagation inside the solid window. In the rectangular coordinate system shown in Figure 3.2, the general expression for the electric field $\vec{E}(x,y,z)$ can be written as [8]

$$\vec{E}(x,y,z) = \hat{x}E_x(x,y,z) + \hat{y}E_y(x,y,z) + \hat{z}E_z(x,y,z) \tag{3.24}$$

where $E_x(x,y,z)$, $E_y(x,y,z)$, $E_z(x,y,z)$ are the electric field components in the X, Y, and Z directions, and $\hat{x}$, $\hat{y}$, $\hat{z}$ are the unit vectors in the X, Y, and Z direction. Therefore, the ratio of the electric field $\overrightarrow{E_1}(x,y,z)$ after propagating the distance z in the Z direction to the electric field $\overrightarrow{E_0}(x,y,z=z_0)$ at z_0, which is the distance between the light source and the entrance to the solid-window surface as shown in Figure 3.2, can be written as

$$\frac{\overrightarrow{E_1}(x,y,z)}{\overrightarrow{E_0}(x,y,z=z_0)} \sim e^{-j\vec{k}\vec{r}} \tag{3.25}$$

where the wave vector and the distance vector can be written as

$$\vec{k} = (k\sin\alpha\,, 0, k\cos\alpha) \tag{3.26}$$

$$\vec{r} = (z\tan\alpha\,, 0, z) \tag{3.27}$$

where α is the incident angle of the radiation, which in our case, is after the refraction occurs at the entrance to the solid window, the incident angle now becomes $\alpha = \theta_t$, as shown in Figure 3.4. In equation (3.26), k is the propagation constant, which can be expressed as

$$k = \omega\sqrt{\varepsilon_0\varepsilon_r\mu} = \omega\sqrt{\mu\varepsilon_0(\varepsilon_r' - j\varepsilon_r'')} \tag{3.28a}$$

$$k = Re(k) + jIm(k) \tag{3.28b}$$

where $\omega = 2\pi c/\lambda$, c is the speed of light, and λ is the wavelength of the incident radiation. In equation (3.28a), μ is the permeability of the material of the solid window, ε_0 is the permittivity

in vacuum, and ε_r is the relative permittivity of the solid window. Because the solid window is made of alumina, which is a dielectric material, ε_r is imaginary. Thus, it can be written as $\varepsilon_r{}' - j\varepsilon_r{}''$, where $\varepsilon_r{}'$ is the real part, and $\varepsilon_r{}''$ is the imaginary part. Since the propagation constant, k, is also a complex number, it can be also written as what has been shown in equation (3.28b).

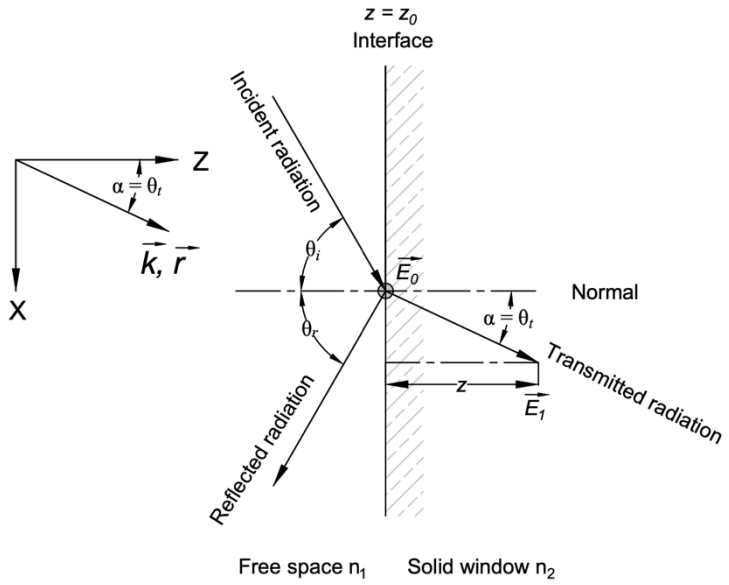

Figure 3.4 Vectors of the electric field at the entrance of the windows

Giving an example at 253.6 nm in wavelength, the permittivity in vacuum $\varepsilon_0 = 8.85 \times 10^{-12}\ F/m$, the relative permittivity ε_r of the solid window made of alumina is $3.1875 - j0.04942$ F/m, [15] and the permeability is $\mu_0 = 4\pi \times 10^{-7}\ H/m$, the propagation constant k can be solved as $4.4255 \times 10^7 - j3.4305 \times 10^5$ (radians/m) from equation (3.28a). Therefore, $Re(k) = 4.4255 \times 10^7$, and $Im(k) = -3.4305 \times 10^5$.

Substituting equations (3.26) and (3.27) into equation (3.25), we have

$$\frac{\overrightarrow{E_1}(x,y,z)}{\overrightarrow{E_0}(x,y,z=z_0)} \sim e^{-jkz(\sin\alpha \tan\alpha + \cos\alpha)} = e^{-jkz/\cos\alpha} \tag{3.29}$$

where the incident angle $\alpha = \theta_t$, and then substituting equation (3.28b) into equation (3.29), we have

$$\frac{\overrightarrow{E_1}(x,y,z)}{\overrightarrow{E_0}(x,y,z=z_0)} \sim e^{-jRe(k)z/\cos\alpha} e^{Im(k)z/\cos\alpha} \tag{3.30}$$

In equation (3.30), it indicates that when the radiation propagates through the solid window, it travels in the Z direction by $e^{-jRe(k)z/\cos\alpha}$ and decays by $e^{Im(k)z/\cos\alpha}$. Therefore, the ratio of the amplitude of the electric field after propagating to the amplitude of the electric field at the entrance of the window can be written as

$$\left|\frac{\overrightarrow{E_1}(x,y,z)}{\overrightarrow{E_0}(x,y,z=z_0)}\right| = e^{Im(k)z/\cos\alpha} \tag{3.31}$$

Now, let L be the thickness of the solid window, when the radiation propagates to the end of the solid window, the decay of the electric field can be written as

$$Decay_E = \left|\frac{\overrightarrow{E_1}(x,y,z=z_0+L)}{\overrightarrow{E_0}(x,y,z=z_0)}\right| = e^{Im(k)L/\cos\alpha} \tag{3.32}$$

Because the power of the electric field is proportional to $\left|\vec{E}\right|^2$, from equation (3.32), the decay of the power of the electric field when the radiation propagating to the end of the solid window can be written as

$$Decay_P = e^{2Im(k)L/\cos\alpha} \tag{3.33}$$

Therefore, the power at the end of the solid window after the propagation, P_{window_end}, can be expressed as

$$P_{window\_end} = P_{window\_in} Decay_P \tag{3.34}$$

where P_{window_in} can be found in equation (3.22), and $Decay_P$ can be obtained by solving the equation (3.33).

Using the UV radiation at 253.6 nm in wavelength and the thickness $50\mu m$ of the solid window as an example, when it is the normal incidence of the radiation, $Decay_P$ is calculated to be $1.2628 \times 10^{-15}\ m^{-1}$. When the UV radiation incidences with a 5-degree angle, $Decay_P$ is calculated to be $1.2107 \times 10^{-15}\ m^{-1}$.

3.2.1.3 Reflection at the interface of the window surface and the free space

When the radiation propagates to the end of the solid window, which means it reaches the interface of the solid window and free space, scattering occurs again. The scattering at the interface of the end of the solid window and free space is similar to the scattering that occurs at the entrance. For computing the reflectance, R_{re_exit}, and the transmittance, T_{tr_exit}, we can use similar calculations mentioned in section 3.2.1.1. They can be determined as

$$R_{re\_exit} = \left| \frac{n_1 \cos\theta_i - n_2\sqrt{1-\left(\frac{n_1}{n_2}\sin\theta_i\right)^2}}{n_1 \cos\theta_i + n_2\sqrt{1-\left(\frac{n_1}{n_2}\sin\theta_i\right)^2}} \right|^2 \tag{3.35}$$

$$T_{tr\_exit} = 1 - R_{re} \tag{3.36}$$

However, at the interface of the end of the solid window and free space, the radiation travels from the solid window into the free space. Therefore, in equations (3.35) and (3.36), n_1 now represents for the refractive index of the material of the solid window, while n_2 represents for the refractive index of air in free space.

In addition, the radiation now travels from inside the dielectric window to free space, total internal reflection may occur at or beyond the critical angle. [17] The critical angle can be determined by [17]

$$\theta_c = \sin^{-1}\left(\frac{n_2}{n_1}\right) \tag{3.37}$$

where n_1 now is the refractive index of the material of the solid window, and n_2 is the refractive index of air in free space. As mentioned in the last section, the refractive index of alumina is approximately 1.92 at 104.8 nm in wavelength, 1.97 at 106.6 nm in wavelength and 1.76 at 253 nm in wavelength. [15] Thus, the critical angle at these wavelengths can be determined by

$$\begin{aligned} \theta_C &= 31.4° \quad (\lambda = 104.8\ nm) \\ \theta_C &= 30.5° \quad (\lambda = 106.6\ nm) \\ \theta_C &= 34.6° \quad (\lambda = 253.6\ nm) \end{aligned} \tag{3.38}$$

Therefore, when the radiation travels to the exit of the solid window at an angle which is greater than the critical angles listed in the equation set (3.38), it will be totally reflected back to the entrance of the solid window, which means there will be no radiation that exits the solid window. If the incident angle of the radiation at the exit of the solid window is less than the critical angle, once we get the reflectance, R_{re_exit}, and the transmittance, T_{tr_exit} from equations (3.35) and (3.36), the power exits the solid window, P_{out}, can be determined by

$$P_{out} = T_{tr\_exit} P_{window\_end} \tag{3.39}$$

where T_{tr_exit} can be found in equation (3.36), and P_{window_end} can be found in equation (3.34).

Therefore, the transmission of the radiation, T, through a solid window can be calculated by

$$T = P_{out}/P_{window\_entrance} \tag{3.40}$$

where P_{out} can be found in equation (3.39), and $P_{window\_entrance}$ can be found in equation (3.15).

We can use a solid alumina window samples that we used for our project as an example to theoretically calculate how much transmission we can get. If we use the UV radiation at 253.6 nm in wavelength to give an example, the optical transmission through a solid window with 100 μm

in thickness is calculated to be 1.3620×10^{-28} in percentage with normal incidence and 1.2501×10^{-28} in percentage with a 5-degree incident angle. The optical transmission ratio through a solid window with $50\ \mu m$ in thickness is calculated to be 1.0786×10^{-13} in percentage with normal incidence and 1.0326×10^{-13} in percentage with a 5-degree incident angle.

In addition, if we use the VUV radiation at 104.8 nm in wavelength to give an example, the optical transmission ratio through a solid window with $1\ \mu m$ in thickness is calculated to be 1.4077×10^{-59} in percentage with normal incidence and 1.1837×10^{-59} in percentage with a 5-degree incident angle. When the thickness of the solid window increases to $5\ \mu m$, the transmission will drop down to 10^{-300} in percentage. This means nearly no VUV radiation at 104.8 nm in wavelength can be transmitted through a micrometer-thick solid window made of alumina.

The results above show us that (1) Given the solid alumina window samples that we used for this project are at least 50 μm in thickness, there will be approximately zero radiation which can be transmitted through the solid windows, either when the wavelength of the radiation is at around 105 nm in the VUV range or at 253.6 nm in the UV range. (2) There is a dramatic loss during the propagation of the radiation inside the solid alumina window, which causes the very low optical transmission through these solid windows. If the thickness of the solid windows is in the range of nanometers, there will be a fair amount of radiation that can be transmitted. Using the theoretical calculations discussed above, if the solid window is 100 nm in thickness, there will be 79.7465% of the UV radiation at 253.6 nm can be transmitted with a normal incidence. Again, the capillary-array window samples that have been used in this project have a thickness in the range of micrometers or millimeters. As a comparison, the solid windows that have the same thickness transmit approximately zero radiation, which means there will be zero radiation that can be transmitted from the solid part of our capillary-array window samples.

3.2.2 Calculation of optical transmission through nanoporous capillary-array windows

The pore diameter of the nanoporous capillary-array windows, which is from 25 to 400 nm, is in the same order as the wavelength of the incident radiation, which is about 100 to 300 nm. Therefore, in this case, each pore in the nanoporous capillary-array window can be treated as an individual cylindrical waveguide with a circular cross-section. So, for these arrays, they may be considered as identical waveguides in parallel.

To calculate how much radiation can be transmitted through such capillary-array windows, we need to consider the following things:

(1) Reflection at the window surface. We need to calculate how much radiation is reflected by the solid window.

(2) Impedance mismatch at the entrance of the waveguide. We need to calculate how much radiation is remains in the waveguide after the impedance mismatch at the entrance. To calculate the impedance mismatch, we need to know a). The permeability and the permittivity of the waveguide b). The cutoff frequency of the waveguide c). the frequency of the incident radiation.

(3) Excited modes of the waveguide. Once the dimension of the circular waveguide and the wavelength of the incident radiation are given, various modes that a waveguide can carry are determined. Thus, we need to calculate the electric and magnetic fields of each mode that is excited.

(4) Coupling to the waveguide. Since only the radiation that can couple to the excited modes can propagate through the waveguide, while for radiation that cannot couple with the

excited modes of the waveguide will be mostly absorbed, we need to calculate how much radiation after the impedance mismatch can be actually coupled to the modes.

(5) Scattering inside the waveguide. The radiation which is successfully coupled into the waveguide can propagate through the waveguide. Only a certain number of modes are excited, and the propagation constant can be obtained for each mode.

(6) Reflection at the exit of the waveguide. When the radiation gets to the exit of the waveguide, the impedance mismatch occurs again, and thus only part of the radiation is transmitted to free space.

(7) Diffraction at the exit of the waveguide. Because of diffraction occurring at the exit of the waveguide, only part of the exiting signal can be collected by the photon detector.

3.2.2.1 Reflection at the window surface

To start with, the reflection at the entrance of the window needs to be considered. Let P_{window} be the total power of the incident radiation hitting the entire capillary-array window including both the solid part of the capillary array and the waveguides. Applying the law of conservation of energy, the radiated power from a light source can be expressed as

$$P = \int \vec{S} \cdot d\vec{A} \tag{3.41}$$

Where $\vec{S}$ is the Poynting vector of the incident radiation as a function of position, and $d\vec{A}$ is a vector differential area element of the capillary-array window surface. Since the nanoporous capillary-array windows are cuboid, we use a rectangular coordinate system as shown in Figure 3.5 to calculate the power that hits the entire window.

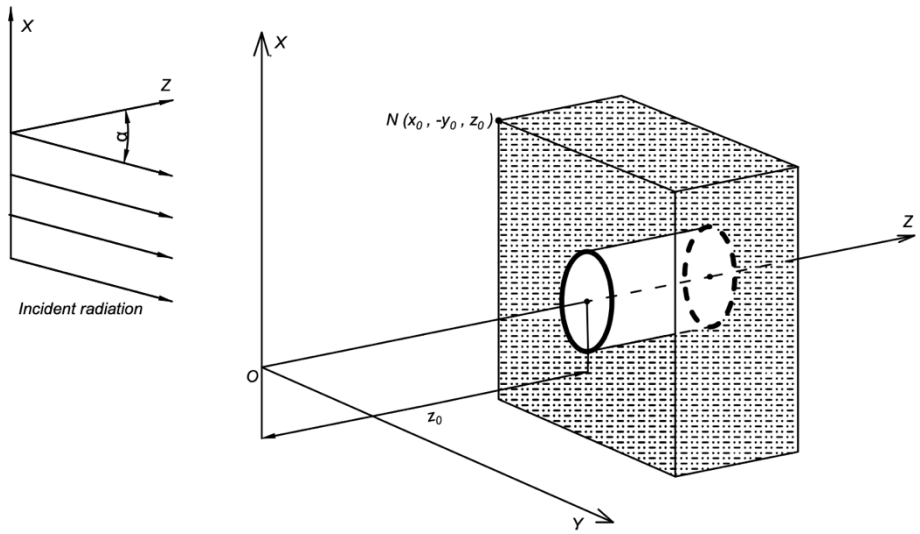

Figure 3.5. Rectangular coordinate system for the capillary-array window

In the rectangular coordinate system shown in Figure 3.5, the origin O is also where the light source is. The Z axis goes through the center of the capillary-array window, and z_0 is the distance between the light source and the capillary-array window. We assume the width of the window to be $2x_0$ and the height of the window to be $2y_0$. Therefore, the area of the cross-section of the window is $4x_0y_0$.

Here, shown in Figure 3.5, we consider that there is an incident angle α on the X-Z plane between the direction of the propagation of the radiation and the surface of the nanoporous capillary-array window. When the incident angle α is zero, the incident radiation propagates along the Z axis, which means that the incident radiation is perpendicular to the capillary-array window.

We have also assumed that the radiation is a plane wave at the capillary-array window surface, which means the power density is uniform over the entire capillary-array window. Therefore, the total power of the incident radiation striking the entire capillary-array window including both the solid window and the waveguides, P_{window}, can be expressed as

$$P_{window} = \int \vec{S} \cdot d\vec{A}$$

$$= \int_{-x_0}^{x_0} \int_{-y_0}^{y_0} (\vec{S} \cdot \hat{n}) dx dy$$

$$= \int_{-x_0}^{x_0} \int_{-y_0}^{y_0} |\vec{S}| (\hat{s} \cdot \hat{n}) dx dy$$

$$= |\vec{S}| \int_{-x_0}^{x_0} \int_{-y_0}^{y_0} (\hat{s} \cdot \hat{n}) dx dy$$

$$= 4x_0 y_0 |\vec{S}| \cos \alpha \qquad (3.42)$$

In equation (3.42), $\vec{S}$ is the Poynting vector, and $d\vec{A}$ is a vector differential area element of the capillary-array window surface. $|\vec{S}|$ is the power density in the units of watts/m^2, $\hat{n}$ represents the unit surface normal to the capillary-array window surface, and $\hat{s}$ represents the unit vector of the incident Poynting vector. The dot product of $\hat{s}$ and $\hat{n}$ becomes $\cos \alpha$ because there is an incident angle α between the Z-axis and the direction of the propagation of the radiation. The power density $|\vec{S}|$ is a constant because the plane wave has a uniform power density over the entire capillary-array window surface.

After finding $P_{window,}$ which is the total power of the radiation incident on the entire capillary-array window from equation (3.37), we need to calculate how much radiation is reflected by both the solid window and by the entrance of the waveguide due to the impedance mismatch.

Let $P_{waveguide\_entrance}$ be the power of the radiation that hits all the waveguides (not the solid window material) over the entire window, and $P_{one\_waveguide\_entrance}$ be the power of the radiation that hits only one single waveguide in the window. Since the incident wave becomes a plane wave when it hits the entrance of the waveguide, we are not considering the phase of the wave but only its amplitude. Since the plane wave has uniform power density over the entire

window, this means each $P_{one\_waveguide\_entrance}$ has the same magnitude, and $P_{waveguide\_entrance}$ can be obtained by multiplying $P_{one\_waveguide\_entrance}$ by the number of waveguides $N_{waveguides}$ in the capillary-array window as shown in equation (3.43).

$$P_{waveguide\_entrance} = N_{waveguides}\, P_{one\_waveguide\_entrance} \tag{3.43}$$

$N_{waveguides}$ is obtained for each capillary-array window, while $P_{one\_waveguide\_entrance}$ can be calculated using the same method we do for calculating P_{window}. Since the waveguides are cylindrical waveguides with circular cross-section, here we use a cylindrical-coordinate system shown in Figure 3.6 to calculate $P_{one\_waveguide\_entrance}$.

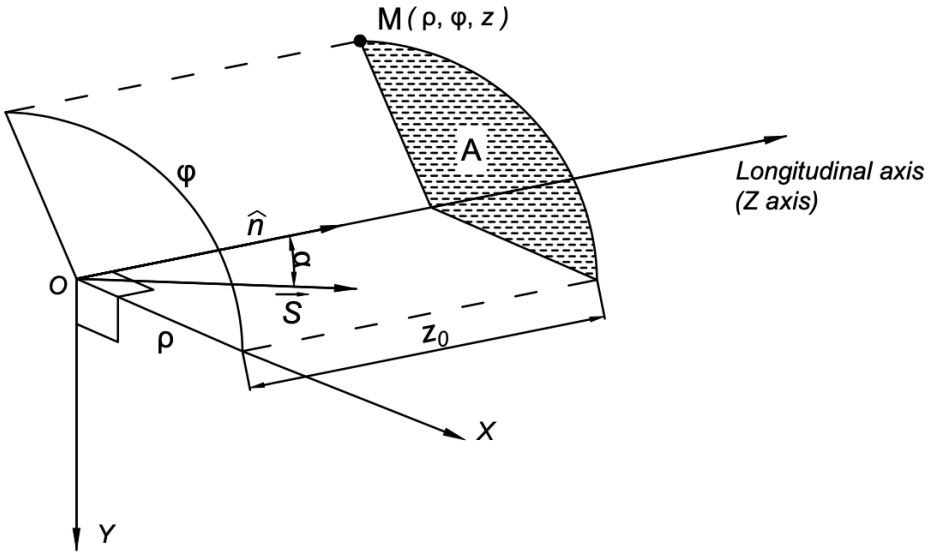

Figure 3.6. Cylindrical coordinate system for one waveguide

In the cylindrical coordinate system shown in Figure 3.6, we can see the following

(1) O is the origin of the cylindrical coordinate that corresponds to the location of the radiation.

(2) ρ is the radial coordinate. When calculating the power entering the waveguide which is at the center of the window, ρ varies from 0 to r_0, where r_0 is the inside radius of the circular waveguide.

(3) φ is the azimuthal coordinate. φ varies from 0 to 2π.

(4) z is the axial coordinate along the longitudinal Z axis. We use z_0 to represent the distance from the light source to the entrance to the capillary-array waveguide, which is 50 cm.

(5) The shaded area A is the cross-sectional area of the entrance of a waveguide. The surface of the entrance of the waveguide is placed paralleled to the plane $Z = 0$.

(6) $\hat{n}$ represents the unit surface normal to the entrance of the waveguide, which is the same as the unit surface normal to the plane $Z = 0$.

(7) $\vec{S}$ is the Poynting vector from the source, which has an angle of α with respect to the direction of the surface normal of the capillary-array window.

Therefore, $P_{one\_waveguide\_entrance}$, the power of the radiation that hits only one single waveguide in the window, can be expressed as

$$
\begin{aligned}
P_{one\_waveguide\_entrance} &= \int \vec{S} \cdot d\vec{A} \\
&= \int_0^{r_0} \int_0^{2\pi} \left(\vec{S} \cdot \hat{n}\right) \rho d\rho d\varphi \\
&= \int_0^{r_0} \int_0^{2\pi} \left|\vec{S}\right| (\hat{s} \cdot \hat{n}) \rho d\rho d\varphi \\
&= \left|\vec{S}\right| \int_0^{r_0} \int_0^{2\pi} (\hat{s} \cdot \hat{n}) \rho d\rho d\varphi \\
&= \pi {r_0}^2 \left|\vec{S}\right| \cos\alpha
\end{aligned}
\tag{3.44}
$$

Therefore, from equations (3.42) and (3.43), we can get $P_{waveguide\_entrance}$, the power of the radiation that hits all the exposable waveguides all over the capillary-array window.

$$P_{waveguide\_entrance} = N_{waveguide}\, \pi {r_0}^2 \left|\vec{S}\right| \cos\alpha \tag{3.45}$$

where we again note that $N_{waveguide}$ is the number of waveguides over the entire capillary-array window.

3.2.2.2 Impedance mismatch at the entrance of the waveguide

When the incident radiation hits the entrance of the waveguide, due to the impedance mismatch, only part of the $P_{waveguide\_entrance}$ can actually enter the waveguide, and the rest of will be reflected from the solid part of the window. Here, we use $P_{waveguide\_in}$ to represent the power that enters the waveguides, and $P_{waveguide\_reflected}$ to represent the power being reflected at the entrance of the waveguides. Thus, $P_{waveguide\_entrance}$ can be expressed as

$$P_{waveguide\_entrance} = P_{waveguide\_in} - P_{waveguide_{reflected}} \tag{3.46}$$

To calculate how much radiation actually enters the waveguide, we need to know the impedance of free space Z_{free} and the impedance of the waveguide Z_w. Then, the power that enters the waveguides $P_{waveguide\_in}$ can be obtained by

$$P_{waveguide\_in} = \left(1 - \frac{Z_w - Z_{free}}{Z_w + Z_{free}}\right) P_{waveguide\_entrance} \tag{3.47}$$

Where Z_{free} is 376.73Ω, and Z_w can be determined by the following equation [8]

$$Z_w = \frac{\sqrt{\frac{\mu}{\varepsilon}}}{\sqrt{1 - \left(\frac{f_c}{f}\right)^2}} \tag{3.48}$$

where μ is the permeability of the waveguide, and ε is the permittivity of the waveguide, f_c is the cut-off frequency of the waveguide, and f is the frequency of the radiation. Here, f_c has different values when different modes are exited in the waveguide. Starting with TE modes, the cut-off frequency can be expressed as [8]

$$f_c = \frac{\chi'_{mn}}{2\pi a\sqrt{\mu\varepsilon}} \tag{3.49}$$

where χ'_{mn} is the *n*th zero (n = 1,2,3……) of the derivative of the Bessel function J_m of the first kind of order m (m = 0,1,2,3……), a is the radius of the cross-section of the cylindrical waveguide, μ is the permeability of the waveguide, and ε is the permittivity of the waveguide. In our case, we assume air is in the waveguide, so $\mu_0 = 4\pi \times 10^{-7}\ H/m, \varepsilon_0 = 8.85 \times 10^{-12}$ F/m. Then, the cut-off wavelength can be expressed as

$$\lambda_c = \frac{c}{f_c} \tag{3.50}$$

where c is the speed of light, which is $3\times 10^8\ m/s$.

For *TE* modes, $\chi'_{01} = 3.8318$, $\chi'_{11} = 1.8412$, $\chi'_{21} = 3.0542$, $\chi'_{02} = 7.0156$ [8] Using the radius $a = 50\ nm$ from one of our nanoporous capillary-array window as an example, the cut-off frequencies and the cut-off wavelengths of these *TE* modes can be determined using equations (3.48) and (3.49)

$$f_{c01} = 3.6574 * 10^{15}\ Hz, \qquad \lambda_{c01} = 82.03\ nm \tag{3.51}$$

$$f_{c11} = 1.7574 * 10^{15}\ Hz, \qquad \lambda_{c11} = 170.71\ nm \tag{3.52}$$

$$f_{c21} = 2.9152 * 10^{15}\ Hz, \qquad \lambda_{c21} = 102.91\ nm \tag{3.53}$$

$$f_{c02} = 1.7582 * 10^{15}\ Hz, \qquad \lambda_{c02} = 44.80\ nm \tag{3.54}$$

In our case, the wavelengths of the radiation we are interested in are 104.8 nm and 106.6 nm. Therefore, from examining the cutoff wavelengths obtained in equations (3.52) and (3.53), only the TE_{11} mode can be excited in the waveguide with the pore radius 50 nm.

We can do the same calculations to get the excited *TM* modes of the waveguide. The cut-off frequency of the *TM* modes can be expressed as [8]

$$f_c = \frac{\chi_{mn}}{2\pi a\sqrt{\mu\varepsilon}} \tag{3.55}$$

where χ_{mn} is the *n*th zero (n = 1,2,3……) of the derivative of the Bessel function J_m of the first kind of order m (m = 0,1,2,3……) of the *TM* modes, a is the radius of the cross-section of the cylindrical waveguide, μ is the permeability of the waveguide, and ε is the permittivity of the waveguide. For *TM* modes, $\chi_{01} = 2.4049, \chi_{11} = 3.8318, \chi_{21} = 5.1357, \chi_{02} = 5.5201$.[8] Using equations (3.55) and (3.50), with $\mu_0 = 4\pi \times 10^{-7}\ H/m$, $\varepsilon_0 = 8.85 \times 10^{-12}$ F/m, and the radius $a = 50\ nm$ of a waveguide, the cut-off frequencies and the cut-off wavelengths of these *TM* modes can be determined by

$$f_{c01} = 2.2955 * 10^{15}\ Hz, \qquad \lambda_{c01} = 130.69\ nm \tag{3.56}$$

$$f_{c11} = 3.6574 * 10^{15}\ Hz, \qquad \lambda_{c11} = 82.03\ nm \tag{3.57}$$

$$f_{c21} = 4.9020 * 10^{15}\ Hz, \qquad \lambda_{c01} = 61.20\ nm \tag{3.58}$$

$$f_{c02} = 5.2689 * 10^{15}\ Hz, \qquad \lambda_{c02} = 56.94\ nm \tag{3.59}$$

In our case, the wavelengths of the radiation we are interested in are 104.8 nm and 106.6 nm. Thus, from the cutoff wavelengths obtained from equations (3.56) and (3.57), only the TM_{01} mode can be excited in the waveguide with the pore radius 50 nm.

Therefore, from what has been calculated above, we can determine how much radiation enters all the waveguides over the entire capillary-array window. Using the wavelength of the

radiation at 104.8 nm and the cut-off wavelengths of both *TE* and *TM* modes of a waveguide with a 50 nm pore radius as an example, the coefficient in the brackets in equation (3.47) is calculated to be 0.8822 for the TE_{11} mode and 0.7479 for the TM_{01} mode. This means 88% of the TE_{11} mode and 75% of the TM_{01} mode will start propagating inside the waveguide, and the rest (12% and 25%) of these two excited modes is reflected back to the free space due to the impedance mismatch.

3.2.2.3 Excited modes of the waveguide

In a waveguide system, we are looking for solutions of Maxwell's equations that are propagating along the guide direction and are confined to the waveguide structure. The electric and magnetic fields can be written as [9]

$$\vec{E}(x,y,z) = \vec{E}(x,y)e^{-j\beta z} \tag{3.60}$$

$$\vec{H}(x,y,z) = \vec{H}(x,y)e^{-j\beta z} \tag{3.61}$$

where β is the propagation constant along the guide direction, and $\vec{E}(x,y)$ and $\vec{H}(x,y)$ are the vector amplitudes. Here, we can decompose Maxwell's equations into components that are longitudinal, that is, along the z-direction, and components that are transverse, along the x, y directions. Thus, the phasor amplitude $\vec{E}(x,y)$ can be written as:

$$\begin{aligned}\vec{E}(x,y) &= \hat{x}E_x(x,y) + \hat{y}E_y(x,y) + \hat{z}E_z(x,y) \\ &= \vec{E}_T(x,y) + \hat{z}E_z(x,y)\end{aligned} \tag{3.62}$$

where $\vec{E}_T(x,y)$ represents for the transverse component of the phasor amplitude of the electric field, and $\vec{E}_Z(x,y)$ represents for the longitudinal component of the phasor amplitude of the electric field.

The Laplace gradient operator can be also decomposed as:

$$\nabla = \hat{x}\partial_x + \hat{y}\partial_y + \hat{z}\partial_z$$

$$= \nabla_T + \hat{z}\partial_z$$

$$= \nabla_T - j\beta\hat{z} \tag{3.63}$$

where ∇_T is the Laplace gradient operator on the transverse plane, and the reason why we have $\partial_z = -j\beta$ is because we assume z-dependence as shown in equations (3.63).

Therefore, we can introduce these decompositions into the Maxwell's equations, and thus we have: [9]

$$\nabla \times \vec{E} = -j\omega\mu\vec{H} \quad \rightarrow \quad (\nabla_T - j\beta\hat{z}) \times \left(\vec{E}_T + \hat{z}E_z\right) = -j\omega\mu\left(\vec{H}_T + \hat{z}H_z\right)$$

$$\nabla \times \vec{H} = j\omega\varepsilon\vec{E} \quad \rightarrow \quad (\nabla_T - j\beta\hat{z}) \times \left(\vec{H}_T + \hat{z}H_z\right) = j\omega\varepsilon\left(\vec{E}_T + \hat{z}E_z\right)$$

$$\nabla \cdot \vec{E} = 0 \quad \rightarrow \quad (\nabla_T - j\beta\hat{z}) \cdot \left(\vec{E}_T + \hat{z}E_z\right) = 0$$

$$\nabla \cdot \vec{H} = 0 \quad \rightarrow \quad (\nabla_T - j\beta\hat{z}) \cdot \left(\vec{H}_T + \hat{z}H_z\right) = 0 \tag{3.64}$$

where μ is the permeability of the waveguide, and ε is the permittivity of the waveguide. In the set of equations (3.64), ∇_T is the Laplace gradient operator on the transverse plane, $\vec{E}_T$ and $\vec{H}_T$ are the transverse field components, and E_z and H_z are the longitudinal field components. We can obtain the equivalent set of Maxwell's equations from (3.65) as follows: [9]

$$\nabla_T E_z \times \hat{z} - j\beta\hat{z} \times \vec{E}_T = -j\omega\mu\vec{H}_T$$

$$\nabla_T H_z \times \hat{z} - j\beta\hat{z} \times \vec{H}_T = j\omega\varepsilon\vec{E}_T$$

$$\nabla_T \times \vec{E}_T + j\omega\mu\hat{z}H_z = 0$$

$$\nabla_T \times \vec{H}_T - j\omega\varepsilon\hat{z}E_z = 0$$

$$\nabla_T \cdot \vec{E}_T - j\beta E_z = 0$$

$$\nabla_T \cdot \vec{H}_T - j\beta H_z = 0 \tag{3.65}$$

From the equation set (3.65) above, the transverse field components $\vec{E}_T$ and $\vec{H}_T$ can be expressed in terms of the longitudinal field components E_z and H_z as follows: [9]

$$\vec{E}_T = -\frac{j\beta}{k_c^2}(\nabla_T E_z - \eta_{TE}\hat{z} \times \nabla_T H_z)$$

$$\vec{H}_T = -\frac{j\beta}{k_c^2}\left(\nabla_T H_z - \frac{1}{\eta_{TM}}\hat{z} \times \nabla_T E_z\right) \tag{3.66}$$

where k_c is the cutoff wavenumber defined as: [9]

$$k_c^2 = \omega^2 \varepsilon\mu - \beta^2 \tag{3.67}$$

where μ is the permeability of the waveguide, and ε is the permittivity of the waveguide. In addition, in the equation set (3.66), η_{TE} and η_{TM} are the transverse impedances for the *TE* modes and *TM* modes carried by the waveguide, which can be determined by: [9]

$$\eta_{TE} = \frac{\omega\mu}{\beta}, \quad \eta_{TM} = \frac{\beta}{\omega\varepsilon} \tag{3.68}$$

Since we are using a cylindrical coordinate system for the waveguide as mentioned in Figure 3.6, the transverse gradient and Laplace operator in cylindrical coordinates become:

$$\nabla_T = \hat{\rho}\frac{\partial}{\partial\rho} + \hat{\varphi}\frac{1}{\rho}\frac{\partial}{\partial\varphi} \quad \text{so that} \quad \nabla_T^2 = \frac{1}{\rho}\frac{\partial}{\partial\rho}\left(\rho\frac{\partial}{\partial\rho}\right) + \frac{1}{\rho^2}\frac{\partial^2}{\partial\varphi^2} \tag{3.69}$$

Now, the transverse field components $\vec{E}_T$ and $\vec{H}_T$ expressed in the set of equations (3.66) can be also written as follows in a cylindrical coordinate system with the decomposition of transverse vectors $\vec{E}_T = \hat{\rho}E_\rho + \hat{\varphi}E_\varphi$ and $\vec{H}_T = \hat{\rho}H_\rho + \hat{\varphi}H_\varphi$:

$$E_\rho = -\frac{j\beta}{k_c^2}\left(\partial_\rho E_z - \eta_{TE}\frac{1}{\rho}\partial_\varphi H_z\right)$$

$$E_\varphi = -\frac{j\beta}{k_c^2}\left(\frac{1}{\rho}\partial_\varphi E_z + \eta_{TE}\partial_\rho H_z\right)$$

$$H_\rho = -\frac{j\beta}{k_c^2}\left(\partial_\rho H_z + \frac{1}{\eta_{TM}}\partial_\varphi E_z\right)$$

$$H_\varphi = -\frac{j\beta}{k_c^2}\left(\frac{1}{\rho}\partial_\varphi H_z + \frac{1}{\eta_{TM}}\partial_\rho E_z\right) \tag{3.70}$$

In addition, to satisfy all the last four equations in the set of equations (3.65), the longitudinal fields $E_z(x,y)$ and $H_z(x,y)$ must satisfy the two-dimensional Helmholtz equations: [9]

$$\nabla_T^2 E_z + k_c^2 E_z = 0$$

$$\nabla_T^2 H_z + k_c^2 H_z = 0 \tag{3.71}$$

and they can be written as follows in a cylindrical coordinate system:

$$\frac{1}{\rho}\frac{\partial}{\partial\rho}\left(\rho\frac{\partial E_z}{\partial\rho}\right) + \frac{1}{\rho^2}\frac{\partial^2 E_z}{\partial\varphi^2} + k_c^2 E_z = 0$$

$$\frac{1}{\rho}\frac{\partial}{\partial\rho}\left(\rho\frac{\partial H_z}{\partial\rho}\right) + \frac{1}{\rho^2}\frac{\partial^2 H_z}{\partial\varphi^2} + k_c^2 H_z = 0 \tag{3.72}$$

From the calculations above, we can obtain the electric and magnetic field of each mode that is excited in the waveguide.

3.2.2.4 Coupling to the waveguide

For the incident wave at the entrance of the waveguide after the impedance mismatch occurs, the transverse electric field components $\vec{E}_{T\_inc}$ and $\vec{H}_{T\_inc}$ can be expressed as follows in a cylindrical coordinate system: [10]

$$\vec{E}_{T\_inc}(\rho,\varphi) = \sum_j a_j \vec{E}_{Tj}(\rho,\varphi) + \vec{E}_{Tr}(\rho,\varphi)$$

$$\vec{H}_{T\_inc}(\rho,\varphi) = \sum_j a_j \vec{H}_{Tj}(\rho,\varphi) + \vec{H}_{Tr}(\rho,\varphi) \tag{3.73}$$

In the equation set (3.73), for all values of ρ and φ, the constants a_j are the modal amplitudes, and $j = 1,2,3 \ldots . M$, where M is the maximum number of modes that are excited in the waveguide. Here, $\vec{E}_{Tj}$ and $\vec{H}_{Tj}$ are the transverse electric and magnetic field components of each excited mode, which can be obtained from the equation sets (3.70) and (3.72) of the section 3.2.2.3. Since the radiation only couples to the excited modes, which become the summation terms of the equation set (3.73), these modes will propagate inside the waveguide, while the transverse portions of the radiation fields at $z = 0$ are denoted by the terms $\vec{E}_{Tr}$ and $\vec{H}_{Tr}$.

The modal amplitudes a_j can be expressed as: [10]

$$a_j = \frac{1}{2N_j}\int \vec{E}_{T\_inc} \times \vec{H}^*_{Tj} \cdot \hat{z}dA = \frac{1}{2N_j}\int \vec{E}^*_{Tj} \times \vec{H}_{T\_inc} \cdot \hat{z}dA \qquad (3.74)$$

where $\hat{z}$ is the unit vector that is parallel to the waveguide axis, which is also along the guiding direction, and $*$ denotes the complex conjugate. The N_j is the normalized power of each mode that can be carried by the waveguide, which can be determined by [10]

$$N_j = \int \vec{E}_{Tj} \times \vec{H}^*_{Tj} \cdot \hat{z}dA \qquad (3.75)$$

Here in the calculations, we use $N_j = 1 = 100\%$ to represent the normalized power of each mode that is excited in the waveguide. Then, when we determine the summation of the power of every excited mode in the waveguide with respect to the normalization N_j, we will get how much percent of the power of the incident radiation can be coupled into the waveguide.

The transverse electric field component $\vec{E}_{T\_inc}$ can be written as follows in a cylindrical coordinate system:

$$\vec{E}_{T\_inc} = E_0 e^{-j(k_\rho \hat{\rho} + k_\varphi \hat{\varphi})} \qquad (3.76)$$

where E_0 is the amplitude factor, k_ρ and k_φ are the wavenumbers on the transverse plane, which have the values of

$$k_\rho = k_0 \sin\alpha, \quad k_\varphi = \frac{\pi}{2} k_0 \tag{3.77}$$

where $k_0 = 2\pi/\lambda_0$, and λ_0 is the wavelength of the incident radiation. In equation (3.77), α is the incident angle of the radiation, which was defined in Figure 3.5 of Section 3.2.2.1.

The transverse electric-field component defined in equation (3.76) can be also written as follows in a cylindrical coordinate system with the decomposition of transverse vectors:

$$\vec{E}_{T\_inc} = \hat{\rho} E_{\rho\_inc} + \hat{\varphi} E_{\varphi\_inc} \tag{3.78}$$

where

$$E_{\rho\_inc} = \frac{\cos\alpha}{2} \left|\vec{E}_{T\_inc}\right| \qquad E_{\varphi\_inc} = \frac{4\cos\alpha}{\pi} \left|\vec{E}_{T\_inc}\right| \tag{3.79}$$

Substituting equation (3.78) into equation (3.74), the mode amplitudes a_j can be determined by the following:

$$\begin{aligned} a_j &= \frac{1}{2N_j} \int \left(\hat{\rho} E_{\rho\_inc} + \hat{\varphi} E_{\varphi\_inc}\right) \times \vec{H}^*_{Tj} \cdot \hat{z} dA \\ &\cong \frac{1}{2N_j} \iint \begin{vmatrix} \hat{\rho} & \hat{\varphi} & \hat{z} \\ E_{\rho\_inc} & E_{\varphi\_inc} & 0 \\ H_{\rho j} & H_{\varphi j} & 0 \end{vmatrix} \hat{z} d\rho d\varphi \\ &= \frac{1}{2N_j} \iint \left(E_{\rho\_inc} \cdot H^*_{\varphi j} - E_{\varphi\_inc} \cdot H^*_{\rho j}\right) (\hat{z} \cdot \hat{z}) d\rho d\varphi \\ &= \frac{1}{2N_j} \iint \left(E_{\rho\_inc} \cdot H^*_{\varphi j} - E_{\varphi\_inc} \cdot H^*_{\rho j}\right) d\rho d\varphi \end{aligned} \tag{3.80}$$

where E_{ρ_inc} and E_{φ_inc} can be found from equation set (3.79), and $H^*_{\varphi j}$ and $H^*_{\rho j}$ can be obtained by each excited mode from equation (3.70).

Since we are only considering the excited modes propagating through the waveguide, the electric and magnetic field that cannot be coupled into the waveguide, which are denoted by the terms $\vec{E}_{Tr}(\rho,\varphi)$ and $\vec{H}_{Tr}(\rho,\varphi)$ in equation (3.73) can be ignored. Now, equation (3.73) becomes the following for calculating the transverse electric field components $\vec{E}_{T\_coupled}$ and $\vec{H}_{T\_coupled}$ of all excited modes:

$$\vec{E}_{T\_coupled}(\rho,\varphi) = \sum_j a_j \vec{E}_{Tj}(\rho,\varphi)$$

$$\vec{H}_{T\_coupled}(\rho,\varphi) = \sum_j a_j \vec{H}_{Tj}(\rho,\varphi) \tag{3.81}$$

The normalized amplitude of the total power that is coupled into the waveguide $P_{coupled}$ in the guided portion of the fields can be determined by: [10]

$$P_{coupled} = \sum_j P_j = \sum_j |a_j|^2 N_j \tag{3.82}$$

where P_j is the power of each excited mode in the waveguide.

3.2.2.5 Scattering inside the waveguide

From the last section, we have calculated how much of the external electric and magnetic fields can be coupled into the waveguide at the waveguide entrance, as well as the power of the electric field from equation (3.80). Now, we need to know how much radiation is lost during the propagation inside the waveguide and how much radiation is left when it reaches the exit of the waveguide.

Let E_z be the longitudinal electric field component at a point inside the waveguide, it must satisfy the two-dimensional Helmholtz equation

$$\nabla_T^2 E_z + \varepsilon k_0^2 E_z = 0 \tag{3.83}$$

where ∇_T is the Laplace gradient operator on the transverse plane, ε is the permittivity of the material of the waveguide, and $k_0 = 2\pi/\lambda_0$, which is the wave number. λ_0 is the wavelength of the incident radiation. Here, E_z can be written as

$$E_z = E_z(Z = 0)e^{j\beta_z z} \tag{3.84}$$

where $E_z(Z = 0)$ represents the longitudinal electric-field component on the surface $Z = 0$, which is the transverse plane at the entrance of the waveguide. Here, β_z is the propagation constant along the Z direction, which is the guide direction.

In a cylindrical coordinate system mentioned in Figure 3.6 of this section, substituting equation (3.84) into equation (3.83), we have the following

$$\left[\left(\frac{\partial^2}{\partial \rho^2} + \frac{\partial^2}{\partial \varphi^2} - \beta_z^2\right) + \varepsilon k_0^2\right] E_z(Z = 0) = 0 \tag{3.85}$$

Therefore, we can find that

$$\left(\frac{\partial^2}{\partial \rho^2} + \frac{\partial^2}{\partial \varphi^2} + \varepsilon k_0^2\right) E_z(Z = 0) = \beta_z^2 E_z(Z = 0) \tag{3.86}$$

From equation (3.86), the propagation constant β_z along the Z direction can be determined by solving this partial-differential-equation problem. This equation can be converted to a problem of finding its eigenvalue. Therefore, the propagation constant corresponding to each mode that is excited in the waveguide can be found.

Using one of the nanoporous capillary-array window samples with a pore radius of 50 nm and the wavelength 104.8 nm of the incident VUV radiation as an example, the modes and their corresponding propagation constant can be determined by solving the differential equation (3.86).

Referring to the calculations in Section 3.2.2.2, the electric and magnetic field components of the TE_{11} of this waveguide with a 50 nm pore radius are shown below in Figure 3.7 as an example. In each subplot of the Figure 3.7, the green or blue squares around the circular hole in the middle represents for the solid window part, and the circular hole represents for the entrance of a single waveguide. From Figure 3.7, we can see the pattern of the excited TE_{11} mode, including the electric and magnetic field of the mode inside the waveguide, which is shown in the circular hole. There is no plot showing for E_z because $E_z = 0$ for the TE mode. The propagation constant β_z of this TE_{11} mode is calculated to be:

$$\beta_z = (0.69466 + 0.08834j)k_0 \tag{3.87}$$

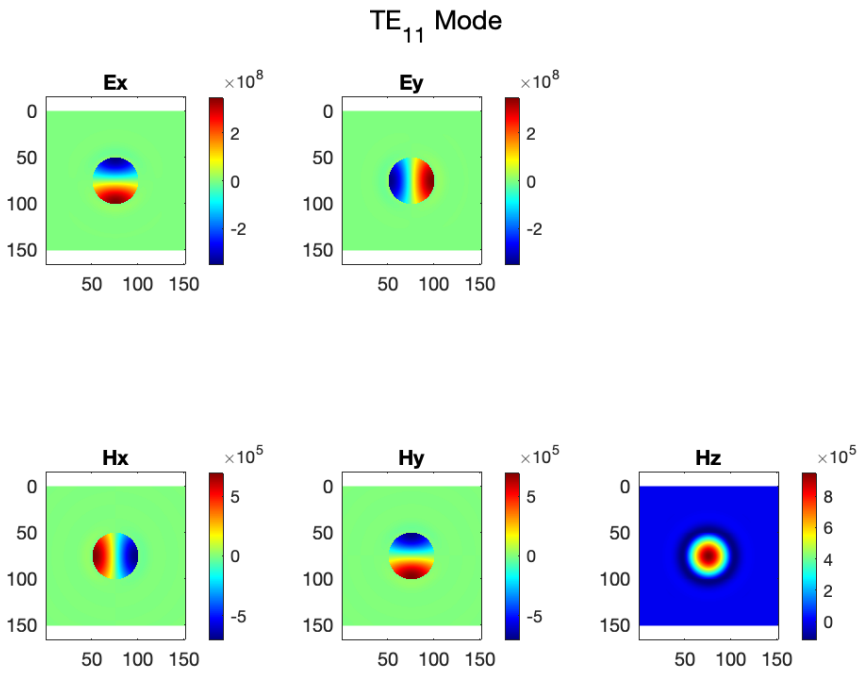

Figure 3.7 Electric and magnetic field components of TE_{11} mode of a waveguide with a 50 nm pore radius

By calculating the propagation constant β_z each excited mode in a waveguide, we will be able to determine how much radiation will be left after propagating a certain distance inside the waveguide or how long the waveguide can be if we would like to have a certain amount of radiation left at the exit.

Similar to equation (3.84), the longitudinal electric field component E_z at the exit of the waveguide can be written as:

$$E_z(Z = L) = E_z(Z = 0)e^{j\beta_z L} \tag{3.88}$$

where L represents the total length of the waveguide. We can also write a similar formula for the modal amplitudes a_{j_exit} at the exit of the waveguide:

$$a_{j\_exit} = a_j e^{j\beta_z L} \tag{3.89}$$

where a_j is the mode amplitude of each excited mode at the entrance of the waveguide, and the calculation of a_j is mentioned in the last section 3.2.2.4 from equation (3.74) to (3.80).

Mentioned in equation (3.82) of the last section 3.2.2.4, $P_{coupled}$ is known as the magnitude of power of the radiation that can be coupled into the waveguide. Now with known mode amplitudes a_{j_exit} at the exit of the waveguide, we can calculate the power of the radiation, which has been coupled into the waveguide, at the exit of the waveguide after propagating inside it:

$$P_{coupled\_exit} = \sum_j \left|a_{j\_exit}\right|^2 N_j \tag{3.90}$$

3.2.2.6 Reflection at the exit of the waveguide

As mentioned in section 3.2.2.2, due to the impedance mismatch, reflection also occurs at the exit of the waveguides. When the radiation gets to the exit of the waveguides, some of it will be reflected back into the waveguide, and some of it will be transmitted out into free space. Let

$P_{exit\_outside}$ be the power that exits the waveguide after the impedance mismatch, so it can be calculated by

$$P_{exit\_outside} = \left|1 - \frac{Z_{free} - Z_w}{Z_{free} + Z_w}\right| P_{exit\_inside} \tag{3.91}$$

where Z_{free} is the impedance of free space, which is 376.73Ω, and Z_w is the impedance inside the waveguide, which can be calculated from equation (3.48) for a given mode. P_{exit_inside} is the power that hits the exit of the waveguide from inside of the waveguide, which is actually the coupled power of the radiation, $P_{coupled\_exit}$, at the exit of the waveguide after propagating inside it. Thus, equation (3.91) can be written as:

$$P_{exit\_outside} = \left|1 - \frac{Z_{free} - Z_w}{Z_{free} + Z_w}\right| P_{coupled\_exit} \tag{3.92}$$

The same process will occur again when the reflected radiation gets back to the entrance of the waveguides, and some will again travel forward to the exit of the waveguides, which we call secondary-reflected radiation in our case. This secondary-reflected radiation will be neglected because we assume its intensity is very small, and this is because (1) at the exit of the waveguide, as shown in equation (3.92) and the results obtained from the calculations mentioned in the previous sections, after the loss during a long travel inside the waveguide, for the radiation that is left and hits the exit of the waveguide from inside the waveguide, approximately 12% of the TE_{11} mode and 25% of the TM_{01} mode can be reflected back toward the entrance of the waveguide (negative Z direction); (2) For this reflected radiation which travels backward, after the propagation loss, when they get back to the entrance, less can get reflected to the positive Z direction. (3) When the secondary reflected radiation from the entrance gets to the exit of the

waveguide again, there will be nothing left. Therefore, we will neglect the secondary-reflected radiation.

Once we get the power that exits the waveguide after the impedance mismatch $P_{exit\_outside}$ from equation (3.92), we can get the optical transmission (T) through the entire nanoporous capillary-array window by

$$T = P_{exit\_outside} / P_{window} \tag{3.93}$$

where P_{window} is the power of the radiation that hits the entire surface of the capillary-array window, which can be obtained from equation (3.42) in section 3.2.2.1. For example, a T value of 0.1 means that 10% of the power injected into the waveguide by the source passed through the capillary-array window.

3.2.2.7 Diffraction at the exit of the waveguide

When the radiation gets to the exit of the waveguides, diffraction also occurs. In this case, at the exit of the waveguide, the mode structure will be the form of the radiation leaving the waveguide.

Here we introduce a constant called the Fraunhofer distance [36], which is defined as $d_F = 2D^2/\lambda_0$. This provides the limit between the near and far field of the diffraction, where D is the diameter of the tube, and λ_0 is the wavelength of the radiation. Using a nanoporous capillary-array window with a pore diameter of 100 nm and a radiation with a wavelength of 105 nm as an example, the Fraunhofer distance d_F is calculated to be 190 nm. In our experiment, the photon detector is 20 cm away from the exit of the capillary-array window, which is much greater than the Fraunhofer distance, thus, only the far field of the radiation is considered for calculating the diffraction at the exit of the nanoporous capillary-array windows.

In the far field, the radiation has a relatively uniform-wave pattern. [12] The amplitude of the both the electric and magnetic fields falls off as $1/l$, where l is the distance between the detector surface and the radiation source. In our case, l is the distance between the photon detector surface and the exit of the waveguide. This means that the total power per unit area at a distance r is proportional to $1/l^2$, and the far-field radiation from a waveguide becomes a spherical wave and then a plane wave.

Therefore, when calculating how much radiation can be detected by the photon detector, once we obtain the power that exits the waveguide after the impedance mismatch $P_{exit\_outside}$ from equation (3.92) and the distance between the exit of the waveguide and the photon detector, we can calculate the how much the power of the radiation is when it hits the photon detector. The power of the radiation that collected by the photon detector, $P_{detector}$, can be calculated by

$$P_{detector} = \frac{A_{detector}}{4\pi l^2} P_{exit\_outside} \tag{3.94}$$

where $A_{detector}$ is the area of the photon detector that collects the radiation, and l is the distance between the exit of the waveguide and the photon detector. In our case, the photon detector is about 20 cm away from the exit of the waveguide. $P_{exit\_outside}$ is the power that exits the waveguide after the impedance mismatch, which can be found from equation (3.92).

3.2.3 Calculation of optical transmission through microporous and milliporous capillary-array windows

When we calculate the optical transmission through microporous and milliporous capillary-array windows, because the size of the pores on the capillary-array window is in micrometers and even millimeters, which is much greater than the wavelength of the radiation, which is about 100 to 250 nm, we will use ray optics to calculate the transmission instead of treating the problem using wave optics (waveguides).

Due to the fact that the size of the pores is much greater than the wavelength of the incident radiation, we make the following assumptions and approximations for calculating the optical transmission through microporous and milliporous capillary-array windows:

(1) As mentioned in the very beginning of section 3.2, we assume that before the radiation enters the capillary-array window, it becomes a plane wave.

(2) When the plane wave hits the surface of the entrance of the pores, the radiation which hits the solid material of the window will be reflected, while the radiation which doesn't hit the solid material will go inside the pores.

(3) The scattering occurring at the inside wall of the pores can be neglected based on the calculations shown in section 3.2.1 for the optical transmission through solid windows, which means that the radiation impinging on the pore walls is assumed all lost.

(4) Only the radiation that doesn't hit the inside wall of the pore during the propagation can be transmitted through the pore.

Therefore, when calculating the optical transmission through microporous and milliporous capillary-array windows, only the following needs to be considered: (1) The reflection by the solid material at the entrance of the window surface (2) The loss during the propagation inside the pore.

3.2.3.1 Reflection at the entrance of the window surface

We proceed in the same way as calculating the optical transmission through nanoporous capillary-array windows mentioned in the last section 3.2.2. First, we need to calculate the reflection at the entrance of the window surface.

As mentioned in equation (3.42) of section 3.2.2, the total power of the incident radiation hitting on the entire capillary-array window including both the solid window and the pores, P_{window}, can be expressed as

$$P_{window} = 4x_0 y_0 |\vec{S}| \cos \alpha \tag{3.95}$$

Here, $\vec{S}$ is the Poynting vector to the capillary-array window surface and $|\vec{S}|$ is the power density in the units of watts$/\mathrm{m}^2$. The power density $|\vec{S}|$ is a constant because the plane wave has a uniform power density over the entire capillary-array window surface. As shown in Figure 3.2, we assume the width of the window to be $2x_0$ and the height of the window to be $2y_0$, therefore the area of the cross-section of the window is $4x_0 y_0$. We also consider that there is an incident angle α on the X-Z plane between the direction of the propagation of the radiation and the surface of the microporous and milliporous capillary-array window. When the incident angle α is zero, the incident radiation propagates along the Z axis, which means that the incident radiation is perpendicular to the capillary-array window.

Similarly, from equation (3.45) in section 3.2.2, we can get $P_{pore\_entrance}$, the power of the radiation that hits all the pores all over the capillary-array window as the following

$$P_{pore\_entrance} = N_{pore}\, \pi {r_0}^2 |\vec{S}| \cos \alpha \tag{3.96}$$

where we again note that N_{pore} is the number of pores over the entire capillary-array window, and $\pi {r_0}^2$ is the area of cross-section of each individual pore. $|\vec{S}|$ is the power density in the unit of $watts/m^2$, and α is the incident angle of the radiation.

From these two equations above, we will be able to calculate a). how much radiation hits the entire capillary-array window b). how much radiation hits the entrance of the pores. Here again, the pores are not treated as waveguides. In addition, the reflection due to the impedance mismatch between the free space and inside the waveguide is also unnecessary to consider for this case, because the size of the pores in these microporous and milliporous capillary-array windows is much larger than the wavelength of the radiation.

3.2.3.2 Loss during the propagation inside the pore

After we know how much radiation enters the pores, we need to calculate how much of it gets lost based on the assumptions that (1) The radiation which hits the inside wall of the pores is considered all lost. (2) Only the radiation that doesn't hit the inside wall of the pores is transmitted.

Starting from a single pore from all pores over the window, we can place the pore in a rectangular coordinate system as shown in Figure 3.8.

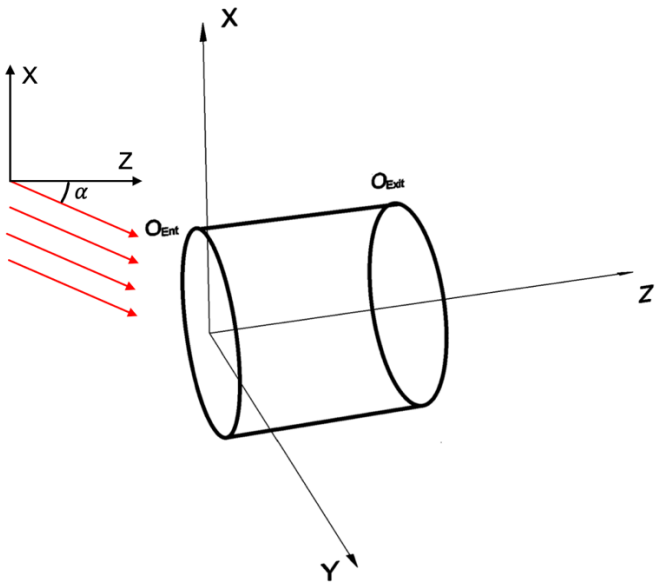

Figure 3.8 Single pore in a rectangular coordinate system

In Figure 3.8, the pore entrance is placed at the $Z = 0$ plane and centered at the original point of the coordinate system. The pore is along the *Z* axis, and the exit of the pore is parallel to the entrance. The propagation of the radiation is also along the *Z* axis, and the incident radiation, which is denoted as an array of red arrows, has an angle α on the X-Z plane. Here, we use O_{Ent} to denote the entrance of the pore and O_{Exit} to denote the exit of the pore.

Because there is an incident angle α, the surface that the incident radiation normal to is no longer the $Z = 0$ plane. Therefore, in Figure 3.9, we introduce a new surface *S1*, where the incident radiation is normal to this surface *S1*. Then, the entrance of the pore O_{Ent} has its projection on surface *S1*, which is denoted as $O_{Ent\ 1}$. Same for the exit of the pore O_{Exit}, surface *S2* is parallel to surface *S1*, and $O_{Exit\ 2}$ is the projection of O_{Exit} on surface *S2*. In addition, the projection of the entrance of the pore O_{Ent} also has its projection on surface *S2*, which is denoted as $O_{Ent\ 2}$.

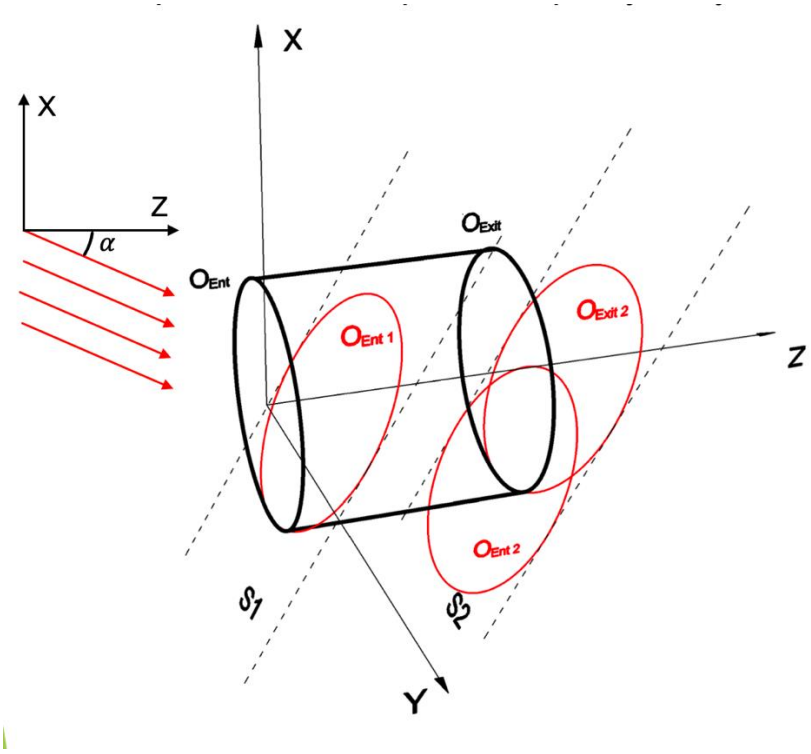

Figure 3.9 Projections on the normal surfaces

Recall that the assumptions for calculating the optical transmission through the pore are that: (1) The radiation which hits the inside wall of the pores is considered all lost. (2) Only the radiation that doesn't hit the inside wall of the pores is transmitted. Thus, from Figure 3.6, we can see that only the photon flux through the overlap area of $O_{Ent\ 2}$ and $O_{Exit\ 2}$ can be transmitted through the pore. Therefore, similarly to equation (3.83), the power of the radiation that gets to the exit of the pore can be written as

$$P_{pore\_exit} = N_{pore}\ A_{overlap} \left|\vec{S}\right| \tag{3.97}$$

where $A_{overlap}$ denotes the overlap area.

Therefore, calculating the overlap area $A_{overlap}$ of $O_{Ent\ 2}$ and $O_{Exit\ 2}$ is vital to determine the power of the radiation that gets to the exit of the pores. Figure 3.10 shows the projections $O_{Ent\ 2}$ and $O_{Exit\ 2}$ on surface *S2* looking from the direction of the incident radiation.

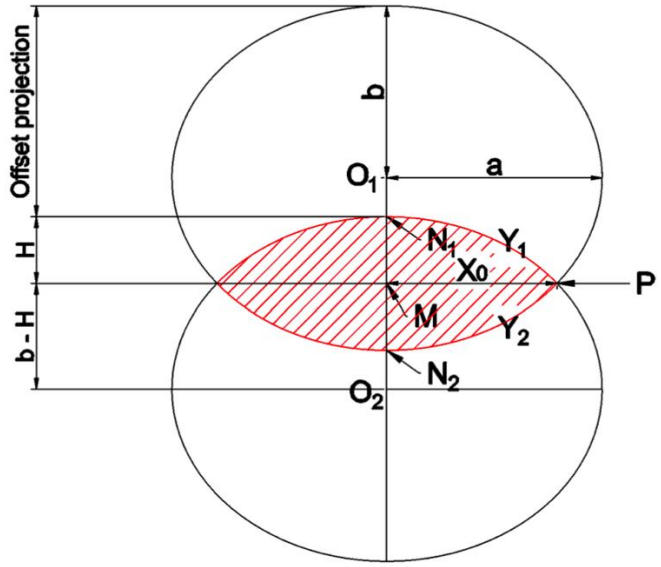

Figure 3.10 Projections on the surface *S2*

In Figure 3.10, there are actually ellipses. The upper ellipse is the $O_{Exit\ 2}$, and the lower one is $O_{Ent\ 2}$. Since there is an incident angle α on the X-Z plane, both the entrance and the exit circle O_{Ent} and O_{Exit} become ellipses, where the longest radius a and the shortest radius b of the ellipse are:

$$a = r_0$$

$$b = r_0 \cos\alpha \tag{3.98}$$

These two ellipses are exactly at the same size because they are the projections of the entrance and the exit of the pore, which are supposed to be the same size. This means these two ellipses $O_{Ent\ 2}$ and $O_{Exit\ 2}$ have the same the longest radius a and the shortest radius b.

In Figure 3.10, O_1 and O_2 denote the center of each ellipse. N_1 is the top of the ellipse $O_{Ent\ 2}$, and N_2 is the bottom of the ellipse $O_{Exit\ 2}$. M is in the middle of N_1 and N_2, and P is one of the intersections of these two ellipses. Here we use X_0 to denote the distance between the points M and P. Y_1 and Y_2 are the upper and lower boundary of the dashed overlap area. The offset projection is defined as the projection on the surface *S2* of the offset of the top point of each circle O_{Ent} and O_{Exit}. The offset projection depends on the incident angle of the radiation as well as the length L of the pore, which can be determined by

$$Offset\ projection = L \tan\alpha \cos\alpha \tag{3.99}$$

In Figure 3.10, we use H to denote the distance between the points M and N_1, then the distance between the points M and O_2 becomes $b - H$. Due to the fact that the ellipse O_2 has the same size as the ellipse O_1, and there are offset by the distance offset projection, we have the following relationship:

$$O_1N_2 + O_2N_1 = O_1O_2 + N_1N_2 \tag{3.100}$$

where O_1N_2 and O_2N_1 are the shortest radius of the ellipse, which is b, and O_1O_2 is equal to the offset projection, and N_1N_2 can be denoted as *2H*, thus, substituting equation (3.99), equation (3.100) can be written as

$$b + b = L \tan\alpha \cos\alpha + 2H$$

$$b - H = \frac{1}{2} L \tan\alpha \cos\alpha \tag{3.101}$$

In addition, because point P of these two ellipses is the intersection of these two ellipses, its coordinates should satisfy the ellipse function, which is

$$\frac{x^2}{a^2} + \frac{y^2}{b^2} = 1 \tag{3.102}$$

where a is the longest radius and b is the shortest radius of the ellipse, which can be found in equation (3.98).

The coordinates of the point P can be written as $(X_0, b-H)$, therefore, substituting its coordinates into equation (3.102), we have

$$\frac{X_0^2}{a^2} + \frac{(b-H)^2}{b^2} = 1 \tag{3.103}$$

From equation (3.103), the value of X_0 can be solved. Therefore, the dashed overlap area $A_{overlap}$ can be determined by

$$A_{overlap} = \int_{-X_0}^{X_0} (Y_1 - Y_2)dx \tag{3.104}$$

where Y_1 and Y_2 can be found from the ellipse equation.

Now we can substitute equation (3.104) into the equation (3.97), the power of the radiation that gets to the exit of the pores can be written as

$$P_{pore\_exit} = N_{pore} \left|\vec{S}\right| \int_{-X_0}^{X_0} (Y_1 - Y_2)dx \tag{3.105}$$

Therefore, the optical transmission through the microporous and the milliporous capillary-array windows can be determined by the power of the radiation hitting the entire capillary-array window and the power of the radiation that gets to the exit of the pores

$$T = P_{pore\_exit} / P_{window} \tag{3.106}$$

where P_{window} is the power of the radiation that hits the entrance of the entire capillary-array window surface, which can be obtained from equation (3.95) in section 3.2.3, and P_{pore_exit} is the power of the radiation that gets to the exit of the pores of the capillary-array window, which can be found from equation (3.105).

3.3 Reference

(1) C. M. Van Atta, *Vacuum Science and Engineering* (McGraw-Hill, New York, 1965), p. 34*ff*

(2) "*Gas Molecules and Gas Flow*", Sept 11th, 2013. Accessed on: May 25th, 2021. [Online] https://vacaero.com/information-resources/vacuum-pump-technology-education-and-training/9364-gas-molecules-and-gas-flow.html

(3) "*Conductance in Vacuum Pumping Systems*", Oct 12th, 2015. Accessed on: May 25th, 2021. [Online] https://vacaero.com/information-resources/vacuum-pump-technology-education-and-training/1025-conductance-in-vacuum-pumping-systems.html

(4) "*Reynolds number*", 9th, September 2021. Accessed on: September 15th, 2021. [Online] https://en.wikipedia.org/wiki/Reynolds_number

(5) Dong Jun Jin, Han S. Uhm and Guangsup Cho, "*Influence of the gas-flow Reynolds number on a plasma column in a glass tube*", Phys. Plasmas **20**, 083513 (2013)

(6) "*What is Reynolds Number?*", 3rd, September, 2021, Accessed on: November 17th, 2021. [Online] https://www.simscale.com/docs/simwiki/numerics-background/what-is-the-reynolds-number/

(7) T. Lucatorto B, T. J. Mcllrath, and J. R. Roberts, Appl. Opt. 18, 2505 (1979)

(8) Constantine A. Balanis, *Advanced Engineering Electromagnetics, 2nd Edition*, (John Wiley & Sons, Inc, 2009) p. 365-370, p. 483-495

(9) Sophocles J. Orfanidis, *Electromagnetic Waves and Antennas* (Piscataway, NJ, 2016), p. 363

(10) A.W. Snyder, J. Love, *Optical Waveguide Theory* ((Science Paperbacks, 190) - Springer (1983)), p.421

(11) "*Finite difference method*", 23rd, August 2022. Accessed on: September 28th, 2022. [Online] https://en.wikipedia.org/wiki/Finite_difference_method

(12) "*Near and far field*", 23rd, January, 2022, Accessed on: February 19th, 2022. [Online] https://en.wikipedia.org/wiki/Near_and_far_field

(13) "*Fraunhofer distance*", 20th, March, 2019, Accessed on: November 16th, 2021. [Online] https://en.wikipedia.org/wiki/Fraunhofer_distance

(14) "*Fresnel equations*", 21st, December, 2021, Accessed on: February 10th, 2022. [Online] https://en.wikipedia.org/wiki/Fresnel_equations

(15) "*Refractive index info*", 2022, Accessed on: October 10th, 2022. [Online] https://refractiveindex.info

(16) "*Brewster's angle*", 26th, October, 2022, Accessed on: November 4th, 2022. [Online] https://en.wikipedia.org/wiki/Brewster%27s_angle

(17) "*Total internal reflection*", 19th, October, 2022, Accessed on: November 4th, 2022. [Online] https://en.wikipedia.org/wiki/Total_internal_reflection

(18) Engineering ToolBox, (2014). "*Gases - Dynamic Viscosities*". Accessed on: Dec 4th, 2022. [online] Available at: https://www.engineeringtoolbox.com/gases-absolute-dynamic-viscosity-d_1888.html

(19). Z. Y. Deng, T. Fukasawa, and M. Ando, "Microstructure and Mechanical Properties of Porous Alumina Ceramics Fabricated by the Decomposition of Aluminum Hydroxide", J. Am. Ceram. Soc., **84** [11] 2638-44 (2001)

(20). B. Seeber, U. T. Gonzenbach, and L. Gauckler, "Mechanical properties of highly porous alumina foams", Journal of Material Research, 28(17):2281-2287. DOI: 10.1557/jmr.2013.102, (2013)

(21). S. C. Nanjangud, R. Brezny, D. J. Green, "Strength and Young's Modulus Behavior of a Partially Sintered Porous Alumina", J. Am. Ceram. Soc., **78** [1] 266-68 (1995)

(22) "*Young–Laplace equation*", 23rd, January, 2023, Accessed on: February 23rd, 2022. [Online] https://en.wikipedia.org/wiki/Young–Laplace_equation

(23). Aslam, Shahid. (2006). "Chapter 4. Bolometer Design", Research Gate, **4-8** (2006)

Chapter 4 – Experimental Setups and Methods

4.1 Experimental setups for optical transmission measurements

4.1.1 Window holder

A fixture to position the capillary-array windows has been constructed using three pieces of polymethylmethacrylate (PMMA) plastic, which is shown in Figure 4.1. Figure 4.1 (A) is the front view of the window holder, and Figure 4.1 (B) is the side view. PMMA was chosen as the material of the window holder. Previous work showed that PMMA blocks light at wavelengths below about 300 nm, which is in the range of wavelengths of UV and VUV that are examined in this work. [1] The PMMA piece in the middle is a u-shaped window sample holder (b), which is held together between the front (a) and the back (c) PMMA plates, all being arranged to allow the window to be slid into the u-shaped holder.

The front and back PMMA plates have a single circular hole in the center to let the VUV pass through. There are two sets of the front and back PMMA plates, and each of them has a circular hole with radius either 4 or 5 mm in diameter so that we can have different exposed areas for experimental-design uses.

The top of the window holder is attached to an angular translator. With the help of the angular translator, we will be able to rotate the capillary-array window holder when it is placed inside the vacuum chamber to give multiple incident angles of the radiation. Once the window sample is installed in the holder, the system is ready for measurements to be made.

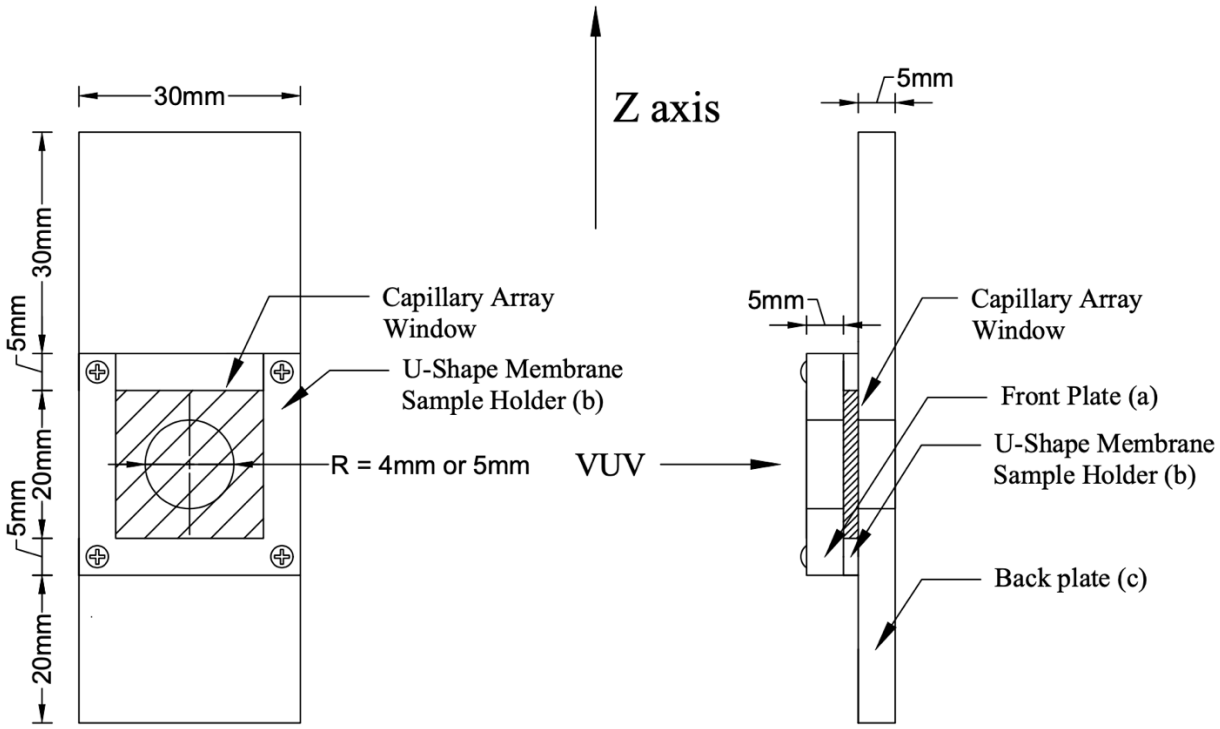

(A) Front view (B) Side view

Figure 4.1. Window sample holder for VUV-transmission measurements

4.1.2 UV-light source

The UV lamp used as a UV source here is a low-pressure, cold-cathode mercury UV Pen-Ray lamp, 11SC-1 from Laser Components S.A.S France, made of double-bore quartz tubing. [2] The power supply for this lamp provides an 800V starting voltage varying at 60Hz and a 270 V operating voltage. The graph below, Figure 4.2 (A), illustrates the relative emission intensities of the UV spectrum.[2] Note that the vertical scale is not linear. Figure 4.2 (B) on the right side is a picture of a UV lamp. [2]

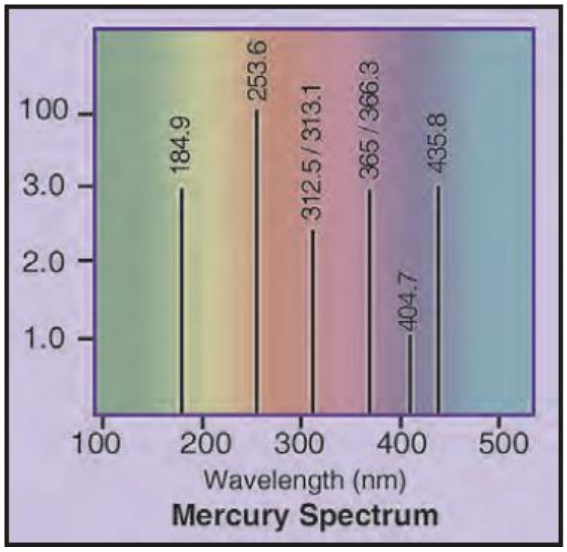

Figure 4.2 (A). Mercury UV Lamp spectrum [2]

Figure 4.2 (B). Mercury UV lamp [2]

From the spectrum shown in Figure 4.2 (A), we can see that the UV peak at 253.6 nm is approximately thirty times larger than the other peaks. Therefore, we use the peak at 253.6 nm to measure the UV transmission through capillary-array windows and solid windows.

4.1.3 VUV source: Electron Cyclotron Resonance (ECR) plasma

Figure 4.3 shows the ECR reactor setup used to generate an argon plasma to be used as a VUV source.

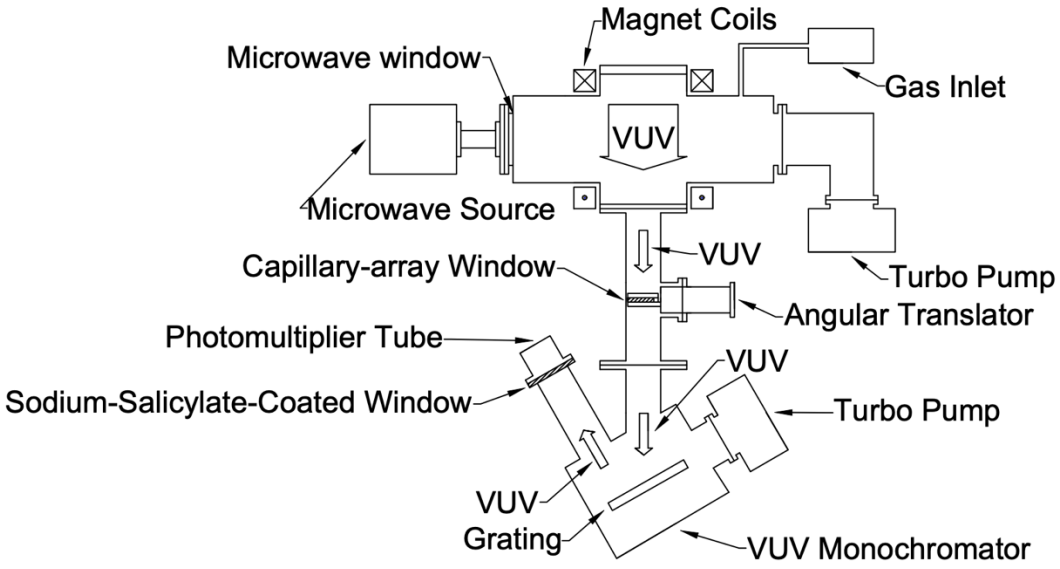

Figure 4.3. Electron-cyclotron-resonance and monochromator

When the plasma is turned on in the ECR chamber, the VUV generated in the plasma passes through the capillary-array window and travels to the monochromator, where it is spread into its spectrum by the grating in the VUV monochromator (McPherson 234/302). The VUV radiation coming from the plasma varies at the line frequency, which is 60 Hz. This variation is one of the reasons why signal processing methods need to be used to suppress the 60 Hz variation, which will be discussed in detail in Section 4.1.4. The radiation, as described earlier, then travels to a quartz window, whose inside is coated with sodium salicylate that fluoresces in the visible such that it can be detected by the photomultiplier tube (PMT) (Hamamatsu R3896). [3]

The ECR and the monochromator chamber are pumped down to 10^{-6} Torr and then argon gas is fed into the ECR chamber using a mass-flow controller (Unit Instruments UFC-1400) to a chamber pressure of 20±1 mtorr. This condition was found to give us the highest magnitude of the argon peaks. The argon plasma is generated in the ECR chamber using a 2.45 GHz, 2 kW microwave-magnetron source. The current through the magnet coils is 1000A. The VUV vacuum monochromator is connected to the ECR chamber. The cyclotron-resonance location inside the ECR chamber is shown in Figure 4.4. [4] Please note that the direction of Figure 4.4 is rotated 90 degrees from Figure 4.3.

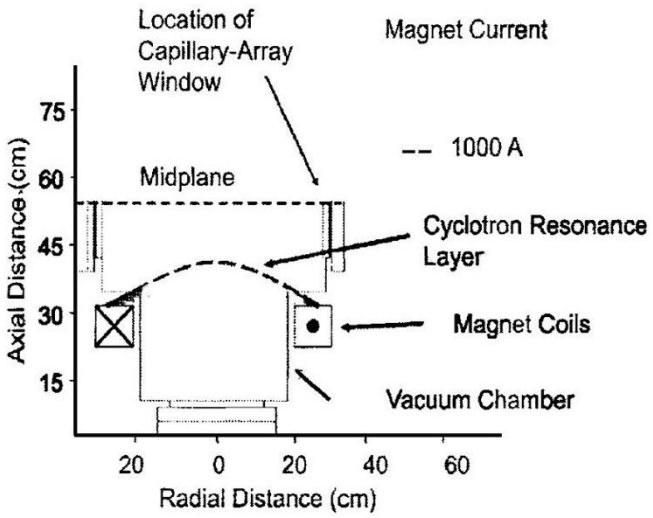

Figure 4.4. Resonance location in the ECR chamber [4]

Additionally, the capillary-array window with its holder is attached to the angular translator, discussed previously, which is placed between the ECR chamber and the VUV vacuum monochromator, which is shown in the middle of Figure 4.3. Using the angular translator, the window then can be rotated to align the VUV beam with the holes on the window. At the output of the VUV monochromator, the PMT detects the visible photons from the fluorescence of the

sodium-salicylate-coated glass window placed between the PMT and the monochromator as shown in Figure 4.3. Sodium salycilate is a wavelength converter in the VUV-spectral region, which can fluoresce in a band between 350-550 nm when it is excited by radiant energy of wavelengths shorter than 350 nm. [5] The PMT used has a wide spectral response between 185 and 900 nm. [6] The reason for using the combination of sodium salycilate plus the PMT is that for initial experiments, the argon peaks at 104.8 nm and 106.6 nm were used as examples for measuring the VUV transmission, which can't be detected directly by the PMT because the glass window does not allow the transmission of VUV radiation. However, it does allow visible light from the sodium salycilate. The PMT was cooled with dry ice to reduce thermal noise, and a 1000V DC bias was applied to the PMT. The photon current coming from the PMT is measured with a Keithley 6487 picoammeter.

4.1.4 Signal collection and data processing

For all of the optical measurements, a set of 1000 data points for each wavelength was collected at a sampling rate of 60 Hz and then stored in the buffer of the picoammeter. Then, a Fast-Fourier Transform (FFT) algorithm was used to convert each data set to the frequency domain from the time domain. An extreme low-pass filter (LPF), with a cut-off frequency of zero Hz, was applied to remove noise and other stray signals. Finally, the data was converted back to the time domain, which resulted in the determinization of the mean value over all data points in the set for each wavelength.

A scan with respect to wavelength was made by setting a wavelength-step to be 0.02 nm, which was determined to give sufficient resolution. Otherwise, for example, when we measured the VUV peaks from argon plasma at 104.8 and 106.6 nm, the peaks could not be detected if we set the wavelength step to be 1 nm or wider.

Using this method of signal collection and data processing, for the UV measurements, the scans were done from 251 nm to 256 nm to cover the UV peak at 253.6 nm with 0.02 nm as the wavelength step. For the VUV measurements, the scans were done from 103.5 nm to 108 nm to cover the VUV peaks at 104.8 and 106.6 nm with the same wavelength step.

4.2 Experimental setups for pressure tests

Pressure tests of the capillary-array windows were performed to get a general estimation on how much pressure differential these capillary-array and/or solid windows can hold before breaking.

Experimentally, a pressure-test system was developed to perform these tests as shown in Figure 4.5.

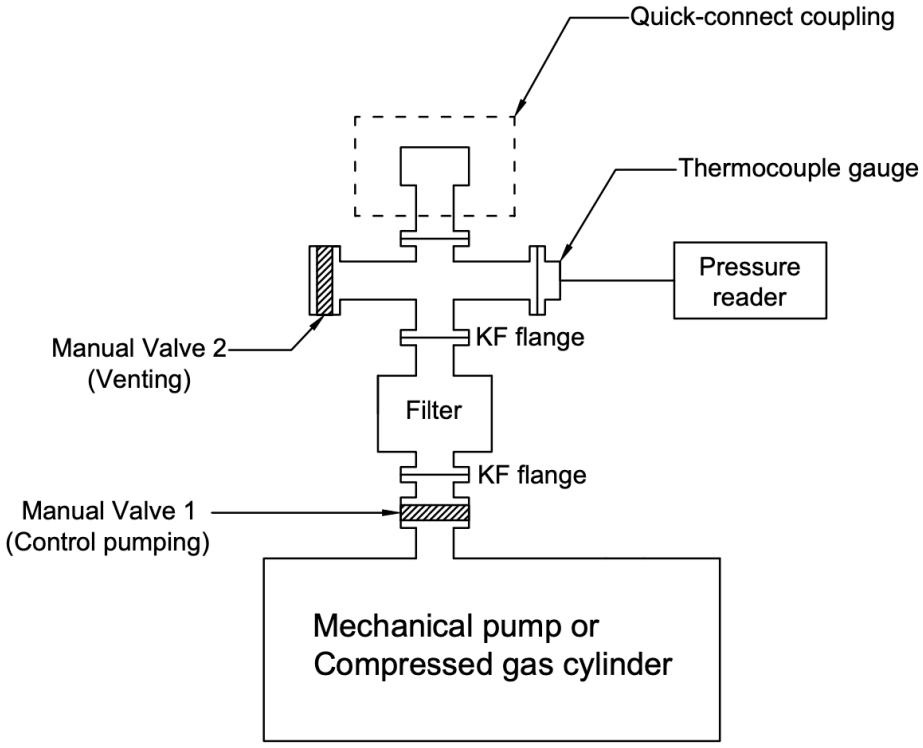

Figure 4.5 Pressure test system

We used the pressure-test system shown in Figure 4.5 to test if the capillary-array window samples can hold the pressure differential between the atmospheric pressure and vacuum pressure in the range of millitorr. In Figure 4.5, a mechanical pump was used to provide vacuum inside the

system, which can pump the system down to around 50 mtorr while the outside of the system is at atmospheric pressure at 760 torr. The mechanical pump used in pressure tests is a Leybold oil sealed vacuum pump TRIVAC D 90 L, which can provide a pumping rate at 110 m^3/h. [14] There is a manual valve placed at the inlet of the mechanical pump to control the pumping rate of the mechanical pump. With utilizing the pressure tests using the pressure-test system shown in Figure 4.5, the absolute pressure differential that applied to the capillary-array windows would be no more than 760 torr, which is one atmosphere. Therefore, in order to estimate the maximum pressure differential that a capillary-array window can hold if it survives from the first round of test over a pressure differential of 760 torr, the further pressure tests will be performed by switching the mechanical pump with a gas-feed-in system and fill the system with nitrogen gas. When feeding in the nitrogen gas into the system while still keeping the outside at the atmospheric pressure, in this way we will be able to control the absolute pressure differential across the capillary-array window and set it to be greater than one atmosphere.

The filter in front of manual valve 1, shown in Figure 4.5, is a Coaxial Trap, 4" Body, NW40, made by MDC precision as shown in Figure 4.6. [7] The filter can remove any possible debris down to 5 μm in diameter from either the breaking capillary-array windows or solid windows during the process of the pressure test.

Figure 4.6 Coaxial Trap, 4" Body, NW40, Filter [7]

In Figure 4.5, on the top of the filter, there is a cross structure with: (1) A manual valve on the left side, which is used to vent the entire pressure test system back to atmospheric pressure after finishing the test. (2) A thermocouple gauge connecting to a pressure reader, which allows us to monitor the real-time pressure inside the pressure test system. (3) A quick-connect coupling, where either the capillary-array windows or solid windows were placed for the pressure test. The quick-connect coupling is shown in Figure 4.7.

Figure 4.7. Quick-Connect Couplings [8]

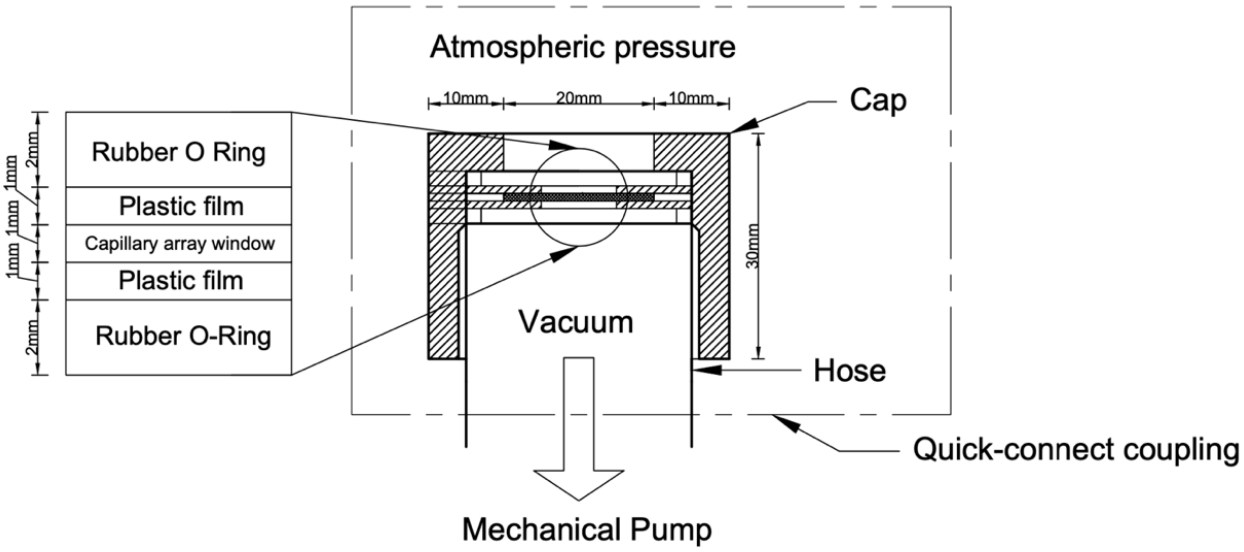

Figure 4.8. Side view of the quick-connect coupling

Figure 4.8 shows a side view of the quick-connect coupling device on the right side of the Figure and an enlarged region of the inside arrangement of the quick-connect coupling on the left side. There are two rubber O rings oriented horizontally between the cap and the vacuum hose. A piece of capillary-array window sandwiched between two polymethylmethacrylate (PMMA)

plastic films with a hole of 10 mm in diameter in the center of each of the films was then placed between the O rings. The area of this hole will be used as the exposed area for the pressure test.

4.3 Statistical Experimental design

To study the UV and VUV transmission efficiency with respect to the pore diameter, thickness, percentage of the open area, the total exposed area of the capillary-array window, and the angle and the wavelength of the incident radiation, multiple measurements need to be made. Thus, statistical experimental design has been applied to our experiments to (1) minimize the number of trials of the experiments. The reason why fewer runs of experiments are preferred in this project is because of the consumption of time and cost of the experiments. If fewer trials of the experiments can lead to the similar results, it will save much time and cost. (2) obtain the maximum optical transmission through capillary-array windows with the optimized choice of factors that we are considering.

A full-factorial design [11] is firstly discussed in this section, followed by a fractional-factorial design.[11] Applying the fractional-factorial design methods to implement the experiments allows us to get the similar results to what we can get from a full set of experiments, but with a smaller number of experimental trials. Next, an advanced factorial-design method is introduced to show us how to implement the experiments with minimized number of trials. This advanced factorial-design method is also compared with a regular fractional-factorial design to show that the advanced method has a much better efficiency on minimizing the experimental trials than a regular fractional-factorial design. Then, the optimization method is discussed to show how we analyze the experimental results obtained with the factorial designs and how it can lead us to the maximum experimental response. Last, we are discussing how we are applying the factorial design method to our experiment of measuring the optical transmission through all the capillary-array windows. The variable factors for the experiments are chosen based on the theoretical factorial design models that were discussed above.

4.3.1 Full-factorial design

A full-factorial experiment is an experiment whose design consists of two or more factors, each with discrete possible values or "levels", and whose experimental units take on all combinations of these levels across all such factors. [9] When we design factorial experiments, it allows us to study the effect of each factor on the response variable, which in this case is the efficiency of transmission of the radiation through the capillary array window, and the effects of interactions between factors on the response variable. In this project, we consider six different factors, which are pore diameter, thickness, open-area ratio (OAR) of the capillary-array window, the total exposed area, as well as the angle and the wavelength of the incident radiation including both UV and VUV. Again, the response variable is the transmission efficiency.

The notation used to denote factorial experiments conveys the number of factors and the number of levels of each factor. For example, a 2^6 factorial design has six factors, and each of the factors has two levels. Therefore, we have $2^6 = 64$ experimental conditions. Another example is that a $2^5 3$ factorial design, where $2^5 3$ indicates that this factorial design has six factors, but five have two levels and one has three levels. Thus, there are $2^5 \times 3 = 96$ experimental conditions.

A full-factorial design can be analyzed by the mean and variance of the factors to predict the optimized response variable. [10] A factorial experimental analysis studies the main effect (ME) of each factor, which indicates the major effect on the response variable resulting from an individual factor, and the interactions (INT) between factors, which imply the effect on the response variable resulting from the combination of the factors. [11]

Starting from the main effect (ME) of each factor, the ME of a factor A with two levels, low $(-)$ and high $(+)$ can be expressed as [11]

$$ME(A) = \bar{z}(A+) - \bar{z}(A-) \tag{4.1}$$

where $\bar{z}(A+)$ represents the average response for all possible combinations of the other factors' conditions when A is a high level, while $\bar{z}(A-)$ represents for the average response when A is at a low level.

After knowing the main effect from one single factor while holding the other factors constant, the interaction (INT) between the factors also needs to be considered, which means the response collected from changing multiple factors at a time. To start with, we look at the interaction between two factors, which is called the two-factor interaction. To determine the two-factor interaction effect, the calculation of the conditional main effect is needed. It is defined as follows: when there is another factor B with two levels, low $(-)$ and high $(+)$, the conditional main effect of B at the high $(+)$ level of A can be determined as [11]

$$ME(B|A+) = \bar{z}(B+|A+) - \bar{z}(B-|A+) \tag{4.2}$$

where the vertical line inside the parenthesis represents for the conditions. For example, $\bar{z}(B+|A+)$ represents for the average of all the response values observed at B+ under the condition of + level of A. Then the conditional main effect of B at low $(-)$ level of A can be determined as [11]

$$ME(B|A-) = \bar{z}(B+|A-) - \bar{z}(B-|A-) \tag{4.3}$$

The interaction (INT) effect between A and B is defined as [11]

$$\begin{aligned} INT(A,B) &= \frac{1}{2} \times \{ME(B|A+) - ME(B|A-)\} \\ &= \frac{1}{2} \times \{ME(B|A+) - ME(B|A-)\} \\ &= \frac{1}{2} \times \{\bar{z}(A+|B+) + \bar{z}(A-|B-)\} - \frac{1}{2} \times \{\bar{z}(A+|B-) + \bar{z}(A-|B+)\} \end{aligned} \tag{4.4}$$

From what has been calculated, we can obtain the effect on the response variable resulting from each single factor, as well as from the interactions between two factors. However, when there are more than two factors in a factorial design, for example, three factors, the effect coming from the interactions between all these three factors will be needed to know how the response variable is going to change when these three factors vary simultaneously. Therefore, when there is a third factor C with two levels, low $(-)$ and high $(+)$, the three-factor interaction effect of A, B and C can be expressed as [11]

$$INT(A,B,C) = \frac{1}{2}INT(A,B|C+) - \frac{1}{2}INT(A,B|C-)$$
$$= \frac{1}{2}INT(A,C|B+) - \frac{1}{2}INT(A,C|B-)$$
$$= \frac{1}{2}INT(B,C|A+) - \frac{1}{2}INT(B,C|A-) \quad (4.5)$$

A more general multiple-factor interaction effect can be expressed as equation (4.6), [11] and it gives us the idea of how the response will be changed when we vary all of these factors simultaneously.

$$INT(A_1, A_2, \dots A_k) = \frac{1}{2}INT(A_1, A_2, \dots A_{k-1}|A_k+) - \frac{1}{2}INT(A_1, A_2, \dots A_{k-1}|A_k-) \quad (4.6)$$

where k indicates how many factors that we are considering when we calculate the interaction effect.

The magnitude of the main effects and the interactions indicates how the factors affect the response variable. The higher the magnitude of the effect or the interaction effect is, the greater the effect on the response variable will be obtained while changing the factor or changing the combination of the factors. When the main effects or the interaction effects are positive, it indicates that increasing the factor or the interaction, the latter of which means increasing several factors

simultaneously, will result in an increase of the response variable. When the effects are negative, the response variable will decrease when increasing the levels of a single factor or an interaction.

From the experimental results of the factorial design for this project and the analysis of a factorial design, we will get general ideas of: (a) Whether we can get a higher or lower response when we change each of the factors or a combination of factors. (b) How much the amplitude of the response will be affected when we change each of the factor or the combination of factors.

4.3.2 Fractional-factorial design

Because 2^k full-factorial designs require that 2^k runs be performed, full-factorial designs are seldom used in practice, while fractional-factorial designs, which consist of a subset or fraction of factorial designs are commonly used. [11]

Using a six-factor experiment as an example, a full-factorial-design requires 2^6 trials of the experiments, while a half-fractional-design only needs half that number of trials. This half-fractional-factorial design is referred as a 2^{6-1} design, where 6 denotes the number of factors, and $2^{-1} = 1/2$ denotes the fraction. Therefore, there will be 32 runs totally. The key is how the fraction should be chosen.

To start with, an example of a half-fractional-factorial design with six factors is given as follows. The factor *F* is assigned to the column that equals the product of the columns for factors *A, B, C, D* and *E*, which is shown in Table 4.1. That is, each entry in the column for F is the product of the corresponding entries in the columns for *A, B, C, D* and *E*. In Table 4.1, + and − represent for the high level (+) and low level (−) of each factor, respectively.

#	A	B	C	D	E	F
1	+	+	+	+	+	+
2	+	+	-	+	+	-
3	+	-	+	+	+	-
4	+	-	-	+	+	+
5	-	+	+	+	+	-
6	-	+	-	+	+	+
7	-	-	+	+	+	+
8	-	-	-	+	+	-
9	+	+	+	-	+	-
10	+	+	-	-	+	+
11	+	-	+	-	+	+
12	+	-	-	-	+	-
13	-	+	+	-	+	+
14	-	+	-	-	+	-
15	-	-	+	-	+	-
16	-	-	-	-	+	+
17	+	+	+	+	-	-
18	+	+	-	+	-	+
19	+	-	+	+	-	+
20	+	-	-	+	-	-
21	-	+	+	+	-	+
22	-	+	-	+	-	-
23	-	-	+	+	-	-
24	-	-	-	+	-	+
25	+	+	+	-	-	+
26	+	+	-	-	-	-
27	+	-	+	-	-	-
28	+	-	-	-	-	+
29	-	+	+	-	-	-
30	-	+	-	-	-	+
31	-	-	+	-	-	+
32	-	-	-	-	-	-

Table 4.1. Design matrix for six factors of a half-factorial design

Based on this design assumption, the main effect of factor F is said to be aliased with the interaction $ABCDE$, which following the sign multiplying rules as listed in Table 4.1. This aliasing relation is denoted by equation (4.7),

$$F = ABCDE \qquad or \qquad I = ABCDEF \tag{4.7}$$

The value of I is the product of the terms on the right-hand side of the equation (4.7), and the equation $I = ABCDEF$ is called the defining relation of the 2^{6-1} design. This design is called a resolution VI design because the defining relation consists of all six factors, which are *A, B, C, D, E,* and *F*. By multiplying both sides of the equation $I = ABCDEF$ by column *A*, we get

$$A = AI = AABCDEF = BCDEF \tag{4.8}$$

The relation $A = BCDEF$ is obtained, which means the column A is identical to the product of column *B*, *C*, *D*, *E* and *F*, so that the main effect *A* is aliased with the interaction $BCDEF$. By following the same method, all aliasing relations can be inferred.

$$A = BCDEF, B = ACDEF, C = ABDEF, E = ABCDF, F = ABCDE$$

$$AB = CDEF, AC = BDEF, AD = BCEF, AE = BCDF, AF = BCDE$$

$$BC = ADEF, BD = ACEF, BE = ACDF, BF = ACDE, CD = ABEF$$

$$CE = ABDF, CF = ABDE, DE = ABCF, DF = ABCE, EF = ABCD$$

$$ABC = DEF, ABD = CEF, ABE = CDF, ABF = CDE, ACD = BEF$$

$$ACE = BDF, ACF = BDE, ADE = BCF, ADF = BCE, AEF = BCD \tag{4.9}$$

As in Wu and Chen (1992), we call a main effect or a two-factor interaction *clear* if none of its aliases are main effects or two-factor interactions, and *strongly clear* if none of its aliases are main effects, two-factor, or three-factor interactions. [12] Therefore, in this resolution VI fractional-factorial design, all the main effects and two-factor interactions are *strongly clear*, and all the three-factor interactions are *clear*.

Equation (4.9) is an example of a resolution VI fractional-factorial design. From Table 4.1, we can see this resolution VI fractional-factorial design only requires 32 trials of experiments, which is half the number of trials of the full-factorial design with six factors.

As for a factorial design with six factors, there are two more alternative fractional-factorial design methods with requiring even fewer trials of the experiments, which are resolution IV and resolution III fractional-factorial designs.

For a resolution IV fractional-factorial design, we define column E as the product of column *A, B,* and *C*, and column F as the product of columns *B, C* and D. In this resolution IV fractional-factorial design, we have the defining relation to be $I = ABCE = BCDF$. That means, we have four factors in the defining relation, and that is why it's called a resolution IV fractional-factorial design. We can denote the resolution IV fractional-factorial design with six factors as a 2^{6-2} design, which means it only requires 16 trials of experiments. Table 4.2 shows all the 16 trials that are required to take for a resolution IV fractional-factorial design, and the equation (4.10) shows all the aliasing relations of a resolution IV fractional-factorial design.

#	A	B	C	D	E	F
1	+	+	+	+	+	+
2	+	+	+	-	+	-
3	+	+	-	+	-	-
4	+	+	-	-	-	+
5	+	-	+	+	-	-
6	+	-	+	-	-	+
7	+	-	-	+	+	+
8	+	-	-	-	+	-
9	-	+	+	+	-	+
10	-	+	+	-	-	-
11	-	+	-	+	+	-
12	-	+	-	-	+	+
13	-	-	+	+	+	-
14	-	-	+	-	+	+
15	-	-	-	+	-	+
16	-	-	-	-	-	-

Table 4.2 Design matrix for a six-factor resolution IV fractional-factorial design

$$A = BCE = DEF = ABCDF, B = ACE = CDF = ABDEF$$

$$C = ABE = BDF = ACDEF, D = AEF = BCF = ABCDE$$

$$E = ABC = ADF = BCDEF, F = ADE = BCD = ABCEF$$

$$AB = CE = ACDF = BDEF, AC = BE = ABDF = CDEF$$

$$AD = EF = ABCF = BCDE, AE = BC = DF = ABCDEF$$

$$AF = DE = ABCD = BCEF, BD = CF = ABEF = ACDE$$

$$BF = CD = ABDE = ACEF, ABD = BEF$$

$$ABF = CEF = BDE, ACD = CEF, ACF = BEF = CDE \quad (4.10)$$

Although the resolution IV fractional-factorial design only requires 16 trials of experiments, from equation (4.10), we can see all the main effects are *clear*, but all other multi-factor

interactions are all *not clear*, which means all these multi-factor interactions can be easily confounded with other interactions.

For a resolution III fractional-factorial design, we define column *D* as the product of columns *A* and *B*, column *E* as the product of columns *B* and *C*, and column *F* as the product of columns *A* and *C*. In this resolution III fractional-factorial design, we have the defining relation to be $I = ABD = BCE = ACF$. That means, we have three factors in the defining relation, and that is why it's called a resolution III fractional-factorial design. We can denote the resolution III fractional-factorial design with six factors as a 2^{6-3} design, which means it only requires 8 trials of experiments. Table 4.3 shows all the 16 trials that are required to take for a resolution III fractional-factorial design.

#	A	B	C	D	E	F
1	+	+	+	+	+	+
2	+	+	-	+	-	-
3	+	-	+	-	-	+
4	+	-	-	-	+	-
5	-	+	+	-	+	-
6	-	+	-	-	-	+
7	-	-	+	+	-	-
8	-	-	-	+	+	+

Table 4.3 Design matrix for a six-factor resolution III fractional-factorial design

In this six-factor resolution III fractional-factorial design, all the main effects and multi-factor interactions are *not clear*. This means if we analyze the results of a six-factor resolution III fractional-factorial design, the effects from all these single factor and interactions can be confounded. That way we cannot distinguish these effects from each of the factors.

4.3.3 Advanced design method

From what has been discussed above, we find that (1) Fractional-factorial design can reduce the number of trials of the experiments. (2) Specifically for this project, which we are considering six factors and each with two levels, we have three fractional-factorial design methods, which are resolution VI, IV, and III. (3) Resolution VI requires the greatest number of trials of the experiment among the three fractional-factorial designs, which will give most clear and accurate analysis on the experimental results. (4) Resolution III requires the least number of trials of the experiment among the three fractional-factorial designs, but the analysis of a resolution III can be vague and the analysis on the effects of each factor along with their aliases will be confounded.

Therefore, we develop a fractional-factorial design method to apply to this project, which allows us to implement minimum number of trials as possible and still leads to an accurate analysis of the experimental results.

4.3.3.1 Screening test

To start with, a screening test was performed to give us an approximate analysis on the effects of each factor along with their aliases. In this project, considering six factors, we implemented the resolution III fractional-factorial design as the screen test, which requires eight trials of experiments. As mentioned in equations (4.1) and (4.6), we will analyze the main effects and their interactions of the factors. From the results of the effect analysis, we can eliminate one or two factors which have very limited contribution to the response variable. The elimination of factors depends on a reference line which we need to calculate, and the reference line shows the confidence level of the experiments. We usually pick 95% as the confidence level, which means 95% of the duplicated experiments will show the same results at this level. Therefore, the reference

line we applied here indicates the 95% of confidence level. For any effects or interactions of factors which exceed the reference line, we state that these factors or interactions are statistically significant, and for those effects or interactions of factors that are below the reference line level, those factors can be eliminated for the future experiments.

4.3.3.2 Half-fractional-factorial design after screening tests

After eliminating a few statistically non-significant factors from the screen test, we can implement a further half-fractional-factorial design to show a more accurate analysis on each of the factors and their interactions.

Depending on how many factors we eliminated from the screen test, we can decide how many further experiments we need to run for a further half-fractional-factorial design. For example, if we can take out one factor out of six, which means we are now only considering five significant factors for the experiments, the further half-fractional-factorial design requires $2^{5-1} = 16$ trials of experiments. If we can take out two factors, which means we are now only considering four significant factors for the experiments, the further half-fractional-factorial design only requires $2^{4-1} = 8$ trials of experiments.

After implementing the further half-fractional-factorial design of experiments, we will be able to get more accurate effects for each of the factors and their interactions.

Comparing method A: a screening test plus further fractional-factorial design and method B: the full resolution VI design, we can see the following: (1) Both methods show clear analysis results on the factors that we are considering for the experiments. (2) Applying the method A, which is the screen test plus further fractional-factorial design, we only need to run either $8 +$

$16 = 24$ or $8 + 8 = 16$ trials of experiment against the $2^{6-1} = 32$ trials of experiments which requires from the full resolution VI design. The way we are applying these methods to our actual experiments will be discussed in section 4.3.5 and the experimental results along with the analysis we got from applying these methods will be discussed in chapter 7.

Due to the fact that each trial of the experiments in our project costs hundreds of dollars, the method of a screening test plus further fractional-factorial design is considered a financially efficient and time saving method.

4.3.4 Factorial design for optimization

Besides reducing the number of trials of experiments, we used the factorial design method to implement our experiments to find an optimized response as well. In our project, we want to find the maximum optical transmission through the capillary-array windows. Therefore, once we get the experimental results from the experiments designed by the fractional-factorial design methods mentioned in section 4.3.3, we will do the analysis of variance (ANOVA) and regression analysis to help us find the maximum response variable.

ANOVA is a collection of statistical models and their associated estimation procedures that used to describe the complex relations among variables. [13] To start with, we calculate the variance of the factorial effects. Similar to equation (4.1), a more general expression of calculating the factorial effect $\hat{\theta}$ is developed as follows:

$$\hat{\theta} = \bar{z}_+ - \bar{z}_- \tag{4.11}$$

where $\bar{z}_+$ and $\bar{z}_-$ are the averages of one half of the observations. If N is the total number of the observations, the variance of the factorial effects can be determined by

$$\mathrm{Var}(\hat{\theta}) = \frac{\sigma^2}{N/2} + \frac{\sigma^2}{N/2} = \frac{4}{N}\sigma^2 \tag{4.12}$$

where σ^2 represents for the variance, which can be calculated by

$$\sigma^2 = \frac{1}{N-1}\sum_i (z_i - \bar{z})^2 \tag{4.13}$$

where $i = i^{th}$ observation, z_i is the response of each of the observation, and $\bar{z}$ is the average of the response of all observations.

Next, we need to take the natural log of the variance, which is shown in equation (4.14) before we do regression analysis and ANOVA. The reasons why we take the natural log of the

variance are the following: (1) It maps the variance σ^2 over the range of $(0, +\infty)$ to natural log of the variance $\ln \sigma^2$ over the range of $(-\infty, +\infty)$, and both regression analysis and ANOVA assume the responses are over the range of $(-\infty, +\infty)$. (2) The natural log of the variance $\ln \sigma^2$ is better for the variance prediction. The reason is that supposing the predicted response $\hat{z} = \ln \sigma^2$, and then the predicted variance $\hat{\sigma}^2 = e^{\hat{z}}$ is always non-negative. The caret sign above z and σ represents for the predicted value of them. (3) Most physical laws have a multiplicative component. Log converts multiplicity into additivity, which makes the calculation easier.

$$\ln \sigma^2 = \ln\left(\frac{1}{N-1}\sum_i (z_i - \bar{z})^2\right) \tag{4.14}$$

Next, we can do the regression analysis. The regression model of a response variable z_i is given by [11]

$$z_i = \beta_0 + \sum_{j=1}^{M} \beta_j x_{ij} \tag{4.15}$$

where β_0 is the fitted intercept, $j = 1,2,3 \ldots M$, and M is the total number of variables we have for a full-factorial design. For example, for this project, we are considering 6 factors. From these 6 factors, we have 6 one-factor variables, 15 two-factor variables, 20 three-factor variables, 15 four-factor variables, 6 five-factor variables, and 1 six-factor variable. Therefore, the total number of variables we have for a full-factorial design, M, is equal to $6 + 15 + 20 + 15 + 6 + 1 = 63$. β_j is the regression estimate coefficient, which is given by [11]

$$\begin{aligned} \beta_j &= \frac{1}{1-(-1)}\Big(\bar{z}\big(x_{ij} = +1\big) - \bar{z}\big(x_{ij} = +1\big)\Big) \\ &= \frac{1}{2}\big(\text{factorial effect of each variable } \mathrm{x_j}\big) \end{aligned} \tag{4.16}$$

where x_{ij} represents for each variable when $j = 1,2,3 \ldots M$ for the $i = i^{th}$ observation.

Now, the optimization of the response variable can be found using the following procedure: (1) Select levels of some factors which have significant effects on the variance to minimize the value of the natural log of the variance. (2) Based on the selections of (1), select the levels of other factors that have significant effects on the response variable, which means passing the referenced 95% confident level, to obtain the optimized response variable.

Here, an example is given to show the procedure of finding the optimized response variable. Please note that the numbers showing in this example are arbitrary, and they don't represent for any physical meanings. From the analysis of variance (ANOVA) and the regression analysis on the response variable, for example, we found that factor C stands out for the ANOVA, and it is the only factor that passes the significant level. We also found factor F stands out for the regression analysis on the response variable, and it is also the only factor that passes the significant level. From equations (4.14) and (4.15), we give an example showing the analysis results on both ANOVA and regression model as below

$$\ln \sigma^2 = -3.772 + 1.917C \tag{4.17}$$

$$z = 45.314 + 0.418F \tag{4.18}$$

Now, following the procedure of finding the optimization of the response variable, first, we need to select the level of factor *C* which gives us the minimum value of the natural log of the variance. As listed in equation (4.17), we want to choose the lower level of factor *C* instead of high level because low level gives us the minimum value of the natural log of the variance. With applying lower level $(-)$ of C, the natural log of the variance in equation (4.17) becomes

$$\ln \sigma^2 = -3.772 + 1.917(-1) = -5.689 \tag{4.19}$$

Next, since factor *F* is the only factor that has significant effects on the response variable, we want to choose the high level (+) of factor *F* to give us the maximum value of the response variable. Therefore, applying high level (+) of factor *F* to equation (4.18), we have

$$z = 45.314 + 0.418(+1) = 45.732 \tag{4.20}$$

With this example, we find that the maximum value of the response variable is calculated to be 45.732 with choosing the low level of factor *C* and the high level of factor *F*. The predicted variance can be determined by

$$\sigma^2 = exp\big(-3.772 + 1.917(-1)\big) = (0.058)^2 \tag{4.21}$$

The variance in equation (4.21) is very small, which means this prediction of the maximum the response variable is likely to be very optimistic. There is also another application of ANOVA and regression analysis. Using the example mentioned in equations (4.17) and (4.18), we can follow the same procedure to calculate the level of each factor to achieve a specific target value for the response variable.

With applying the analysis method to our actual experimental results designed by the advanced factorial design method mentioned in the last section, we will be able to find the optimized response variable. The detailed analysis and optimization on our experimental data will be discussed in Chapter 7.

4.3.5 Factorial design applied to this project

In this project, we are trying to find the maximum optical transmission through various capillary-array windows with a minimum number of experimental trials. Therefore, the optical transmission through capillary-array windows will be considered as the response variable of the factorial design. The factors that we are considering in the factorial design include (1) Pore diameter; (2) Thickness; (3) OAR; (4) Exposed area; (5) Wavelength of the radiation; (6) Incident angle of the radiation.

The capillary-array window samples are divided into three different groups as mentioned in Chapter 2, which are nanoporous, microporous, and milliporous capillary-array windows. However, we will not apply the factorial experimental design to measure the optical transmission through the nanoporous capillary-array windows due to the following reasons: (1) Referring to the theoretical calculations of the optical transmission through the nanoporous capillary-array windows, the calculated result shows less than 10^{-10} % of the radiation can be transmitted. (2) The results of preliminary experiments on measuring the optical transmission through the nanoporous capillary-array windows also shows nearly no optical signal can be collected. With such a limited amount of radiation passing through the nanoporous capillary-array windows, we are unable to get reasonable transmission data which allows us to do statistical analysis. Therefore, we will only implement the factorial-design methods to the experiments on measuring the optical transmission through both microporous and milliporous capillary-array windows.

Table 4.4 and Table 4.5 show the factors along with their levels that we are considering in the factorial design experiments for microporous and milliporous capillary-array windows respectively.

	Levels	+	-
A	Diameter	50 μm	25 μm
B	Thickness	1000 μm	500 μm
C	OAR	60%	50%
D	Exposed area (Diameter)	5 mm	4 mm
E	Wavelength	253 nm	105 nm
F	Incident angle	5	0

Table 4.4 Factorial design for microporous

	Levels	+	-
A	Diameter	50 μm	25 μm
B	Thickness	1000 μm	500 μm
C	OAR	60%	50%
D	Exposed area (Diameter)	5 mm	4 mm
E	Wavelength	253 nm	105 nm
F	Incident angle	5	0

Table 4.5 Factorial design for microporous

Due to the limit and the cost of the capillary-array window samples, we will only measure the optical transmission through the microporous and milliporous capillary-array window samples listed in the tables above using the factorial-design methods. As for the nanoporous capillary-array windows, the measurements on the optical transmission will still be performed but not with the factorial-design methods due to the fact that the transmission through these nanoporous capillary-array windows are so small. These measurements on the optical transmission through nanoporous capillary-array windows, which will be mentioned in Chapter 5, will give sufficient information on the properties of the optical transmission through these nanoporous capillary-array windows without applying the factorial-design method.

4.4 Reference

(1) "Poly(methyl methacrylate)", May 13th, 2021. Accessed on: May 13th, 2021. [Online] https://en.wikipedia.org/wiki/Poly(methyl_methacrylate)

(2). Laser Components, "Pen-ray Light Sources", 11SC-1 UV lamp, 45 bis Route des Gardes, 92190, Meudon, France

(3). James A. R. Samson and G. N. Haddad, "Fluorescent efficiency of sodium salicylate between 116 and 600 Å", Journal of The Optical Society of America, 64, 1346 (1974)

(4). J. D. Chatterton, G. S. Upadhyaya, J. L. Shohet, J. L. Lauer, R. D. Bathke, and K. Kukkady, J. Appl. Phys. 100, 043306 (2006).

(5). James A. R. Samson and G. N. Haddad, "Fluorescent efficiency of sodium salicylate between 116 and 600 Å", Journal of The Optical Society of America, 64, 1346 (1974)

(6). Hamamatsu, "Photomultiplier Tube R3896, R12896", Photomultiplier Tube R3896 spreadsheet, TPMS1084E01, (2014)

(7) "*Coaxial Trap, 4" Body, NW40, Filter*", 2022. Accessed on: Oct. 19th, 2022. [Online] https://www.mdcprecision.com/433015-coaxialtrap-4-inchbody-nw40-filter

(8) "*Quick Connect Couplings*", 2021. Accessed on: May 13th, 2021. [Online] https://www.lesker.com/newweb/flanges/adapters_couplings_quickconnect.cfm?pgid=0

(9) "*Factorial experiment*", May 7th, 2021. Accessed on: May 15th, 2021. [Online] https://en.wikipedia.org/wiki/Factorial_experiment

(10) Cohen, J (1968). "Multiple regression as a general data-analytic system". Psychological Bulletin. 70 (6): 426–443.

(11). C. F. Jeff Wu, Michael S. Hamad, *Experiments: Planning, Analysis, and Optimization, 2nd Edition,* (Wiley, New Jersey, 2009) p. 158-214

(12) Wu, C.F.J. and Chen. Y. "A graph-aided method for planning two-level experiments when certain interactions are important", *Technometrics*, **34**. 162-175.

(13) "*Analysis of variance*", September 5th, 2022. Accessed on: Nov. 6th, 2022. [Online] https://en.wikipedia.org/wiki/Analysis_of_variance

(14) "*Leybold TRIVAC D 90 L*", 2022. Accessed on: Dec. 6th, 2022. [Online] https://www.leyboldproducts.us/products/oil-sealed-vacuum-pumps/trivac/trivac-l/pumps/3362/trivac-d-90-l

Chapter 5 – Optical Transmission through Capillary-array Windows and Solid Windows

In this Chapter, the experimental results on optical transmission through capillary-array windows and solid windows are presented. Regarding the wavelength of the incident radiation, we are discussing both the UV and VUV transmission. Previous work [1][2] shows that a microporous capillary-array window with approximately 20 μm in pore diameter, 1 mm in thickness and 53% in OAR can transmit roughly 40% of VUV radiation in the range of 104.8 to 106.6 nm in wavelength.

In this project, we are not only discussing the transmission of VUV radiation in the range of 104.8 to 106.6 nm in wavelength, but we are also discussing the transmission of UV radiation at 253.6 nm in wavelength. Moreover, we experimentally measured the transmission through three categories of capillary-array windows which have pore diameters in the range of nanometers, micrometers and millimeter as well.

The UV light source we used comes from a low-pressure, cold-cathode mercury UV Pen-Ray lamp, [3] which was introduced in section 4.1.2. The UV lamp emits a wide range of UV radiation with respect to wavelength. The UV peak at 253.6 nm in wavelength was chosen as the reference because it has the highest intensity that the mercury UV lamp generates.

The VUV radiation is generated by an argon plasma in the ECR system, which is described in section 4.1.3. The VUV peaks we used as the reference are at 104.8 nm and 106.6 nm in wavelength.

Besides the wavelength of the incident radiation, we also present the optical transmission through the capillary-array windows and solid windows with two levels of exposed area. These round exposed areas are 4 mm and 5 mm in radius. The optical transmission through these two

exposed areas was measured for the capillary-array windows and solid windows, and it will be presented in this Chapter. The optical transmission through capillary-array windows and solid windows with an oblique incidence has also been measured and will also be discussed in this chapter.

5.1 UV transmission measurements

Starting from the UV transmission, we present the transmission results through nanoporous, microporous, milliporous capillary-array windows, as well as the solid windows. For each type of window, we consider two levels of exposed area on the window and different incident angles of the radiation.

5.1.1 Nanoporous capillary-array windows

As mentioned in Table 2.1 of chapter 2, we introduced two nanoporous capillary-array window samples used in our project. One of the nanoporous capillary-array window samples is SmartPor25, which has 40 nm pore diameter, 50 μm in thickness, and 34.34% in OAR. The other one is SmartPor40, which is 90 nm pore diameter, 100 μm in thickness, and 47.01% in OAR. To start with, the transmission of the UV radiation at 253.6 nm with normal incidence through both nanoporous capillary-array windows with 4 mm in radius of the round exposed area is shown in Figure 5.1.

In Figure 5.1, the black curve represents for the referenced UV spectrum, which is the UV peak at 253.6 nm measured without a nanoporous capillary-array window. The intensity of the reference spectrum is shown as 2.04×10^{-5} amperes in Figure 5.1 as the current intensity collected by the PMT. The green curve is the UV transmitted spectrum through SmartPor25 shown in Figure 5.1. With a nanoporous capillary-array window, SmartPor25 with a 40 nm pore diameter, 50 μm in thickness, and 34.34% in OAR, the transmitted UV intensity is measured as 2.82×10^{-7} amperes. The red curve is the UV transmitted spectrum through SmartPor40 shown in Figure 5.1. With the SmartPor40 in place, with a 90 nm pore diameter, 100 μm in thickness, and 47.01% in OAR, the transmitted UV intensity is measured as 1.24×10^{-7} amperes.

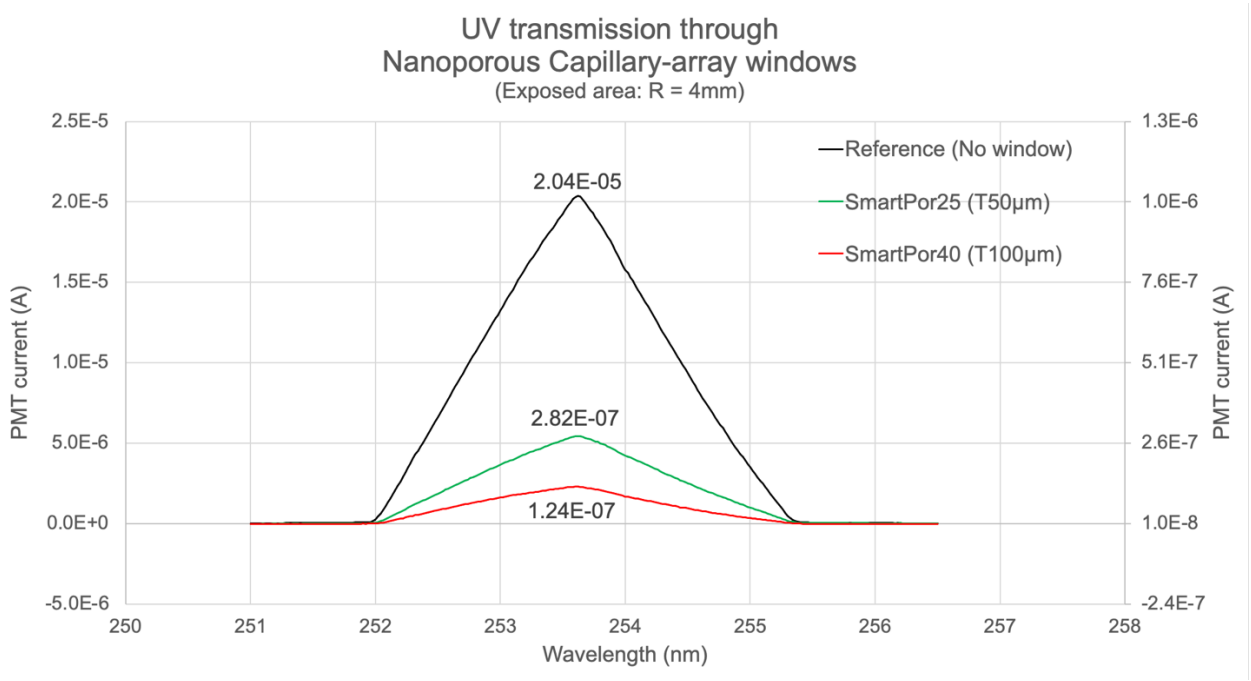

Figure 5.1 UV transmission through nanoporous capillary-array windows with 4 mm in radius exposed area

The UV transmission ratio through these nanoporous capillary-array windows is determined by

$$Transmission = \frac{transmitted\ intensity - thermal\ noise}{reference\ intensity - thermal\ noise} \times 100\% \qquad (5.1)$$

where the thermal noise level was measured at 1×10^{-8} amperes.

From the intensities shown in Figure 5.1 and equation (5.1), with the incident radiation propagating perpendicular to the nanoporous capillary-array window surface, the UV transmission through the nanoporous capillary-array windows SmartPor25 and SmartPor40 with 4 mm in radius exposed area is calculated to be 1.38% and 0.61%, respectively.

The UV transmission through both nanoporous capillary-array windows with 5 mm in radius of the round exposed area is also measured, which is shown in Figure 5.2. The incident radiation is perpendicular to the nanoporous capillary-array window surface as well.

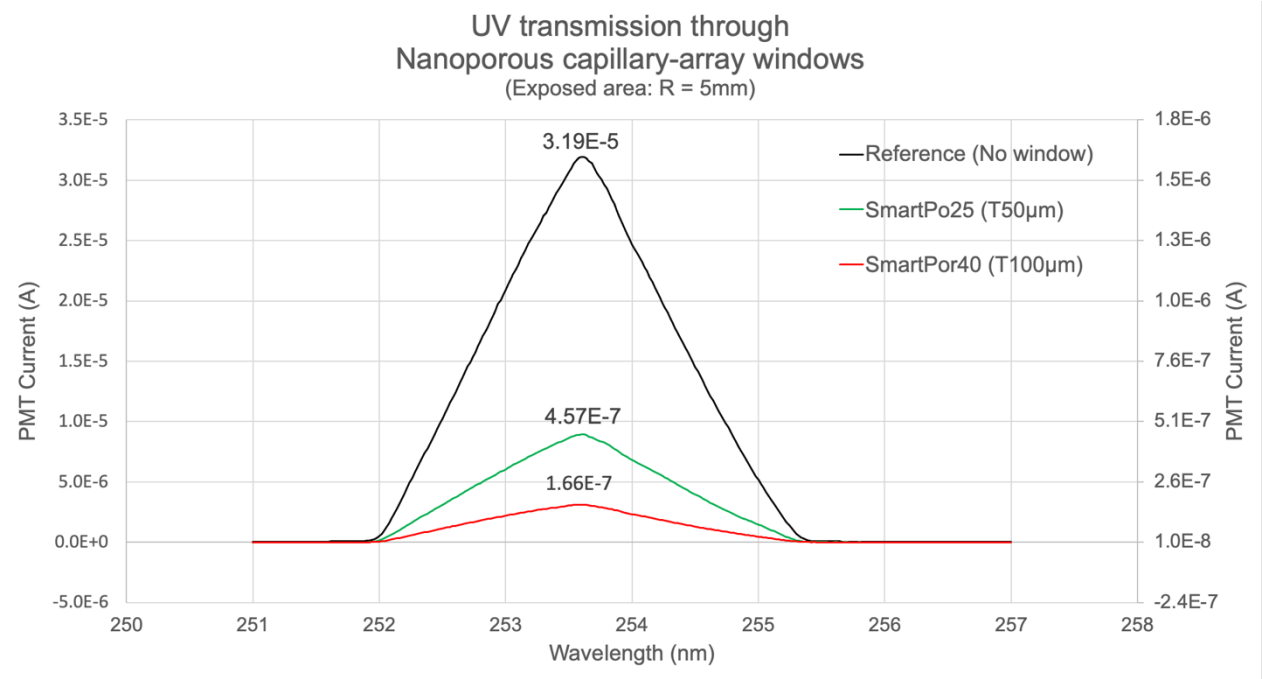

Figure 5.2 UV transmission through nanoporous capillary-array windows with 5 mm in radius exposed area

In Figure 5.2, the black curve represents for the referenced UV spectrum with no window present. The intensity of the reference spectrum is shown as 3.19×10^{-5} amperes in Figure 5.2. The green curve is the UV-transmitted spectrum through SmartPor25 shown in Figure 5.2. With a SmartPor25 in place with a 40 nm pore diameter, 50 μm in thickness, and 34.34% in OAR, the transmitted UV intensity was measured as 4.57×10^{-7} amperes. The red curve is the UV transmitted spectrum through SmartPor40 shown in Figure 5.2. With the SmartPor40 in place,

with a 90 nm pore diameter, 100 μm in thickness, and 47.01% in OAR, the transmitted UV intensity was measured as 1.66×10^{-7} amperes.

From the intensities shown in Figure 5.2 and equation (5.1), with the incident radiation propagating perpendicular to the nanoporous capillary-array window surface, the UV transmission through the nanoporous capillary-array windows SmartPor25 and SmartPor40 with 5 mm in radius exposed area was calculated to be 1.43% and 0.52%, respectively.

Besides the normal incidence, the transmission of the UV radiation at 253.6 nm in wavelength through the nanoporous capillary-array windows with a 5-degree incident angle was also measured. However, the experimental results show there is nearly no transmitted UV radiation that can be detected by the PMT at the exit of the nanoporous capillary-array windows.

As mentioned in Chapter 3, the calculations also shows that the transmission of the UV radiation at 253.6 nm in wavelength through the nanoporous capillary-array windows is less than 1% with either normal incidence or a 5-degree incident angle. Therefore, very limited UV radiation at 253.6 nm in wavelength can be transmitted through these nanoporous capillary-array window samples used in our project.

5.1.2 Microporous capillary-array windows

The transmitted UV spectra through microporous capillary-array windows along with the reference UV spectrum without a microporous capillary-array window in place were measured, and the experimental results will be presented in this section.

Recalling the dimensions of the microporous capillary-array window samples, there are (1) two levels for the pore diameter, which are 25 and 50 μm; (2) two levels for the thickness, which are 0.5 and 1 mm; (3) two levels for the OAR, which are 50% and 60%. The detailed dimensions of each window sample that was used for measuring the UV transmission properties are listed in Table 2.2 of Chapter 2.

To start with, the UV transmission through microporous capillary-array windows with 4 mm in radius exposed area is shown in Figure 5.3. Here, the incident radiation is propagating normal to the microporous capillary-array window surface.

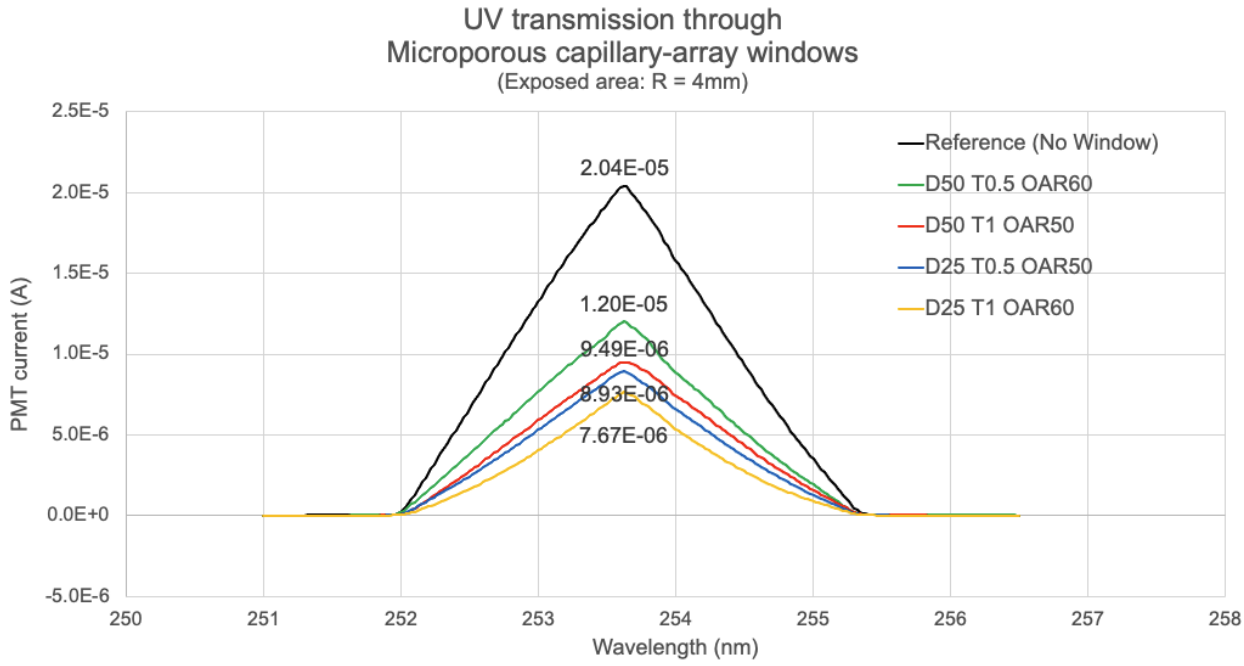

Figure 5.3 UV transmission through microporous capillary-array windows with 4 mm in radius exposed area

In Figure 5.3, the black curve represents the reference UV spectrum, which is the UV peak at 253.6 nm measured without a microporous capillary-array window in place. The intensity of the reference spectrum is 2.04×10^{-5} amperes as the current intensity collected by the PMT. The other spectra are the transmitted spectra through the microporous capillary-array windows. The dimension of each microporous capillary-array window is listed on the legend, with *D* representing for the diameter in μm, *T* representing for thickness in mm, and OAR standing for the open area ratio in percentage. The UV transmission ratio through these microporous capillary-array windows can be determined by equation (5.1) with the same thermal noise level measured at 1×10^{-8} amperes.

The UV transmission through microporous capillary-array windows with 5 mm in radius exposed area was also measured and is shown in Figure 5.4. Again, the incident radiation is propagating normal to the microporous capillary-array window surface.

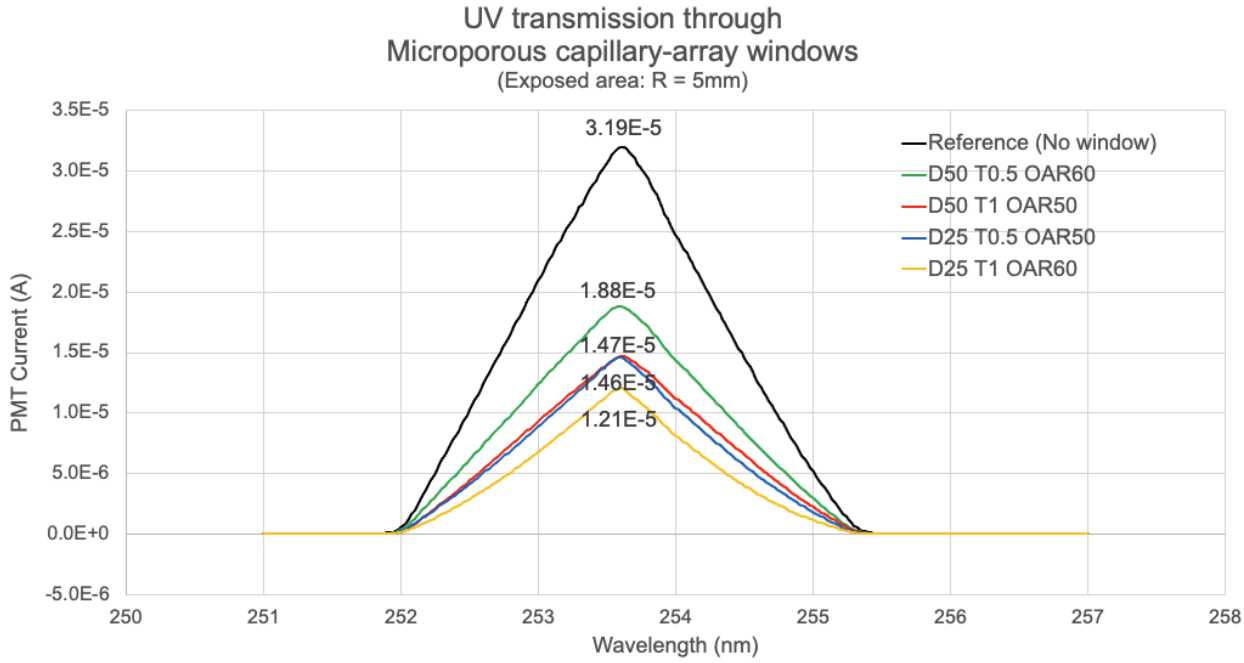

Figure 5.4 UV transmission through microporous capillary-array windows with 5 mm in radius exposed area

Besides normal incidence, the UV transmission through these microporous capillary-array windows with a 5-degree incident angle was also measured. Table 5.1 summarizes the UV transmission ratio through the microporous capillary-array windows with multiple dimensions, exposed areas, as well as the wavelengths and the angles of the incident UV radiation.

Diameter (μm)	Thickness (mm)	OAR (%)	Exposed area (R: mm)	Wavelength (nm)	Incident angle (degree)	Transmission
50	0.5	60	4	253	0	58.82%
50	1	50	4	253	0	46.51%
25	0.5	50	4	253	0	43.78%
25	1	60	4	253	0	37.60%
50	0.5	60	5	253	0	58.93%
50	1	50	5	253	0	46.01%
25	0.5	50	5	253	0	45.77%
25	1	60	5	253	0	37.93%
50	0.5	60	4	253	5	2.35%
50	1	50	4	253	5	0.48%
25	0.5	50	4	253	5	0.46%
25	1	60	4	253	5	0.12%
50	0.5	60	5	253	5	2.16%
50	1	50	5	253	5	0.55%
25	0.5	50	5	253	5	0.51%
25	1	60	5	253	5	0.47%

Table 5.1 Summary of UV transmission through microporous capillary-array windows

From Table 5.1, we can see microporous capillary-array windows have different performance transmitting UV radiation due to their different dimensions. While comparing the transmission with two exposed areas, it doesn't show much difference. For example, the first measurement shows that for an exposed area with 4 mm in radius, the window with 50 μm pore diameter, 0.5 mm in thickness and 60% in OAR shows 58.82% of UV transmission with normal incidence. Then, the fifth measurement shows 58.93% of the UV transmission with normal incidence through the same capillary-array window for an exposed area with 5 mm in radius, which is very close to the transmission under the condition that is exposed with an area with 4 mm in radius. We can also easily tell from Table 5.1 that when there is a 5-degree incident angle of the UV radiation, the transmission drops dramatically.

We also compare the results of the experimental measurements to the results of the calculations mentioned in Chapter 3. Using one of the microporous capillary-array windows with 50 μm in pore diameter, 0.5 mm in thickness and 60% in OAR as an example, the calculated transmission of UV radiation at 253.6 nm through this window is 60% with normal incidence and an exposed area of 4 mm in radius. As shown in Table 5.1, the experimental results show that the experimental UV transmission through this window was measured at 58.82% under the same condition, which is very close to the results of the theoretical calculations.

In addition, with a 5-degree incident angle, the transmission of UV radiation at 253.6 nm through this window is calculated to be 3.103% with an exposed area of 4 mm in radius. As shown in Table 5.1, the experimental results show that the experimental UV transmission through this window was measured at 2.35% under the same condition, which is also in good agreement with the calculated results.

5.1.3 Milliporous capillary-array windows

The transmitted UV spectra through milliporous capillary-array windows along with the reference UV spectrum without a milliporous capillary-array window in place were measured, and the experimental results will be presented in this section.

Recalling the dimensions of the milliporous capillary-array window samples, there are (1) two levels for the pore diameter, which are 1 and 1.50 mm; (2) two levels for the thickness, which are 0.5 and 1 mm; and (3) two levels for the OAR, which are 20% and 44%. The detailed dimension of each milliporous capillary-array window sample that was used for measuring the UV transmission properties are listed in Table 2.3 of Chapter 2.

To start with, the UV transmission through milliporous capillary-array windows with 4 mm in radius exposed area is shown in Figure 5.5. Here, the incident radiation is propagating normal to the microporous capillary-array window surface.

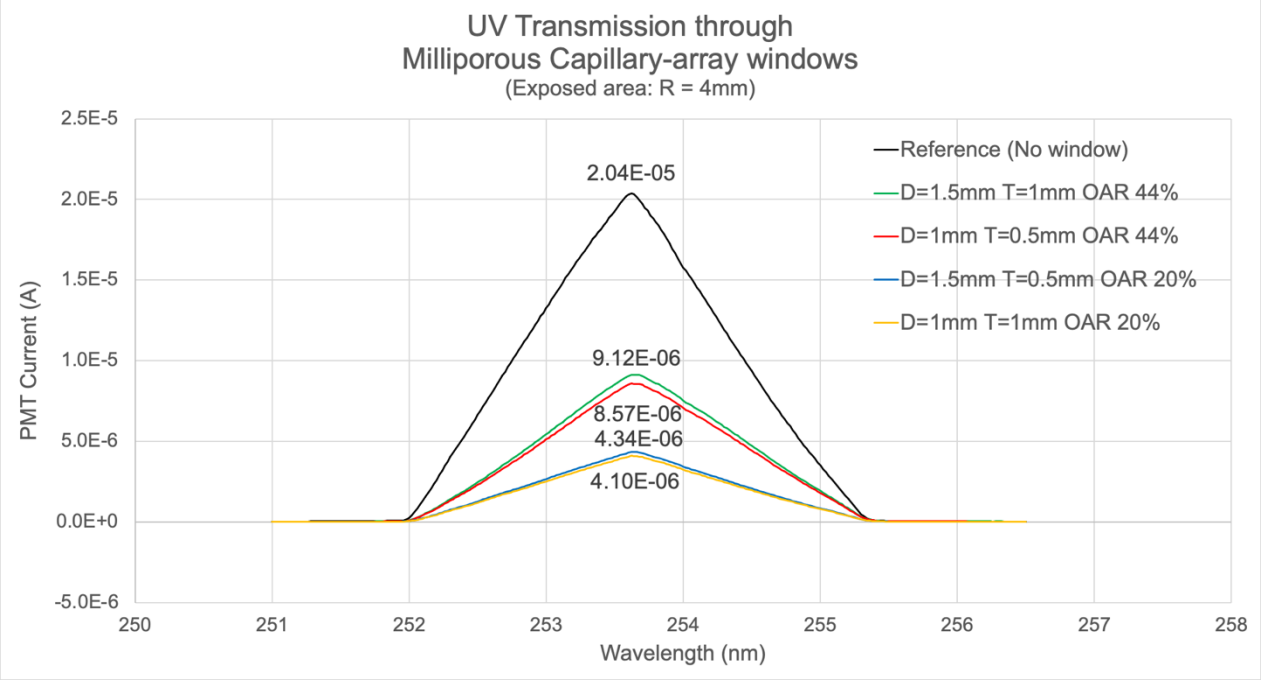

Figure 5.5 UV transmission through milliporous capillary-array windows with 4 mm in radius exposed area

In Figure 5.5, the black curve represents the reference UV spectrum, which is the UV peak at 253.6 nm measured without a milliporous capillary-array window in place. The other spectra are the transmitted spectra through the milliporous capillary-array windows. The dimension of each milliporous capillary-array window is listed on the legend. The UV transmission ratio through these milliporous capillary-array windows can be determined by equation (5.1) with the thermal noise level measured at 1×10^{-8} amperes.

The UV transmission through milliporous capillary-array windows with 5 mm radius exposed area was also measured and is shown in Figure 5.6. Again, the incident radiation is propagating normal to the milliporous capillary-array window surface.

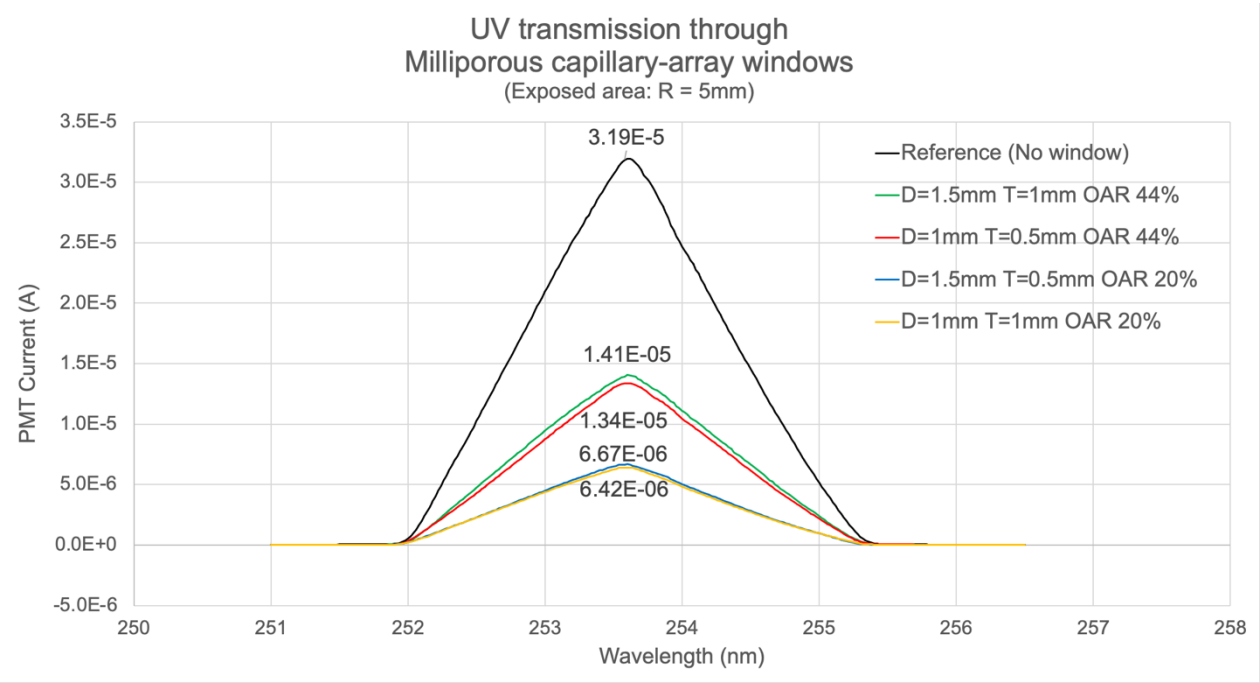

Figure 5.6 UV transmission through milliporous capillary-array windows with 5 mm in radius exposed area

Besides the normal incidence, the UV transmission through these milliporous capillary-array windows with 5-degree incident angle were also measured. Table 5.2 summarizes the UV transmission ratio through the milliporous capillary-array windows with multiple dimensions, exposed areas, as well as the wavelengths and the angles of the incident UV radiation.

Diameter (mm)	Thickness (mm)	OAR (%)	Exposed area (R:mm)	Wavelength (nm)	Incident angle (degree)	Transmission
1.5	1	44	4	253	0	44.62%
1	0.5	44	4	253	0	41.92%
1.5	0.5	20	4	253	0	21.14%
1	1	20	4	253	0	19.96%
1.5	1	44	5	253	0	44.07%
1	0.5	44	5	253	0	41.88%
1.5	0.5	20	5	253	0	20.81%
1	1	20	5	253	0	20.00%
1.5	1	44	4	253	5	42.27%
1	0.5	44	4	253	5	38.85%
1.5	0.5	20	4	253	5	18.93%
1	1	20	4	253	5	15.71%
1.5	1	44	5	253	5	41.81%
1	0.5	44	5	253	5	38.92%
1.5	0.5	20	5	253	5	18.70%
1	1	20	5	253	5	15.60%

Table 5.2 Summary of UV transmission through milliporous capillary-array windows

From Table 5.2, we can see milliporous capillary-array windows have different transmission performance for UV radiation due to their different dimensions. When comparing the exposed areas, it doesn't show much difference. In addition, when there is a 5-degree incident angle, the UV transmission through milliporous capillary-array windows drops less significantly compared to the microporous capillary-array windows. The reason is that milliporous capillary-array windows have a much greater pore diameter to thickness ratio than microporous capillary-array windows. As mentioned in section 3.2.3, due to a smaller pore diameter to thickness ratio, more radiation will hit the inside walls of the pore, and that means this radiation will be fully absorbed by the solid part of the window. Therefore, when there is an incident angle, more radiation can be transmitted through the milliporous capillary-array windows.

We also compare the results of the experimental measurements to the results of the calculations mentioned in Chapter 3. Using one of the milliporous capillary-array windows with 1.5 mm in pore diameter, 1 mm in thickness and 44% in OAR as an example, the theoretical transmission of UV radiation at 253.6 nm through this window is calculated to be 44% with normal incidence and an exposed area with 5 mm in radius. As shown in Table 5.2, the experimental results show that the experimental UV transmission through this window was measured at 44.07% under the same condition, which is very close to the results of the calculations.

In addition, with a 5-degree incident angle, the theoretical transmission of UV radiation at 253.6 nm through this window is calculated to be 40.42% with an exposed area of 5 mm in radius. As shown in Table 5.2, the experimental results show that the experimental UV transmission through this window was measured at 41.81% under the same condition, which is also in good agreement with the experimental results.

5.1.4 Thin solid windows

The UV transmission through solid windows has also been measured to give a comparison to the UV transmission through capillary-array windows. The solid-window samples we used to measure the UV transmission here have no open area, thus, we only consider the thickness of the window as one of the factors that represents the dimension of the window. The thicknesses of the solid window samples has been chosen as 0.05, 0.1, 0.5, and 1 mm to give a comparison with the capillary-array windows which have the same thickness.

We also consider two levels of exposed area for measuring the UV transmission through these thin solid windows to match it with the measurements of the capillary-array windows. The results of the UV transmission through solid windows with normal incidence is first discussed. Figure 5.7 shows the UV transmission through the thin solid windows with an exposed area which has a 4-mm radius.

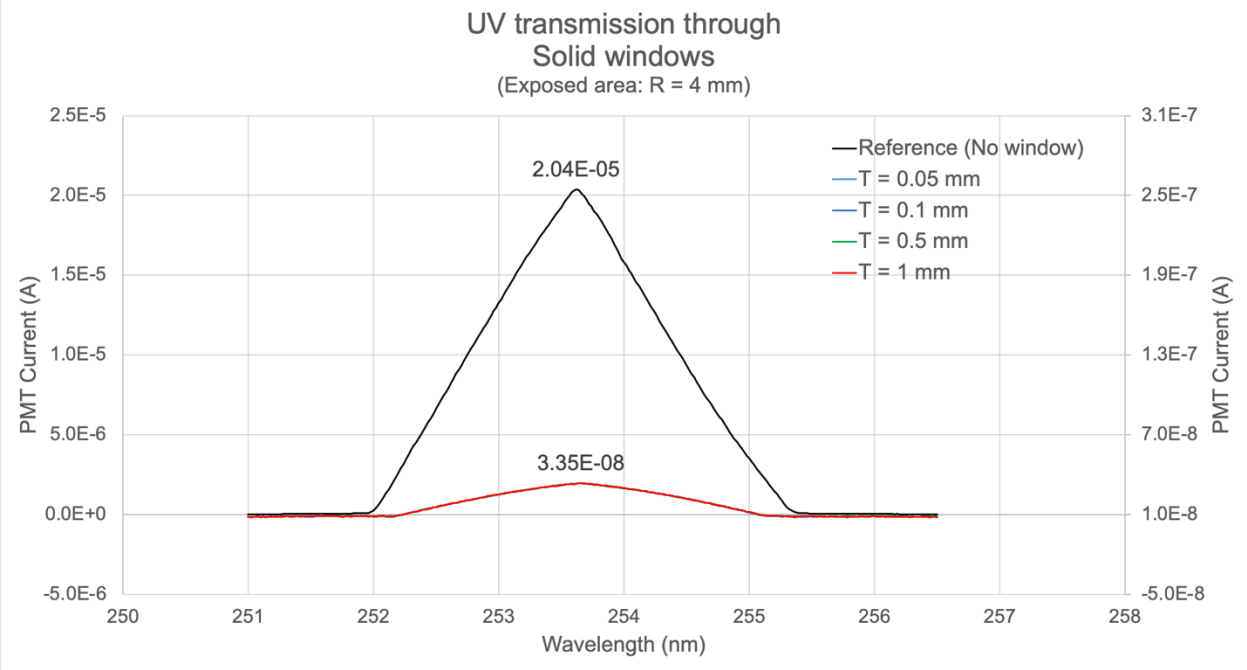

Figure 5.7 UV transmission through solid windows

with 4 mm in radius exposed area

In Figure 5.7, the black curve represents for the referenced UV spectrum without the presence of a solid window. The other spectra are the transmitted spectra through solid windows. The thickness of each solid window is listed on the legend. The transmitted spectra through solid windows with different thickness are overlapped, which means there is pretty much the same amount of UV radiation which can be transmitted through these solid windows even though they are different in thickness. The UV transmission ratio through these solid windows was calculated to be approximately 0.11% by equation (5.1) with the thermal noise level measured at 1×10^{-8} A.

Figure 5.8 shows the UV transmission through these thin solid windows with an exposed area which has a 5-mm radius.

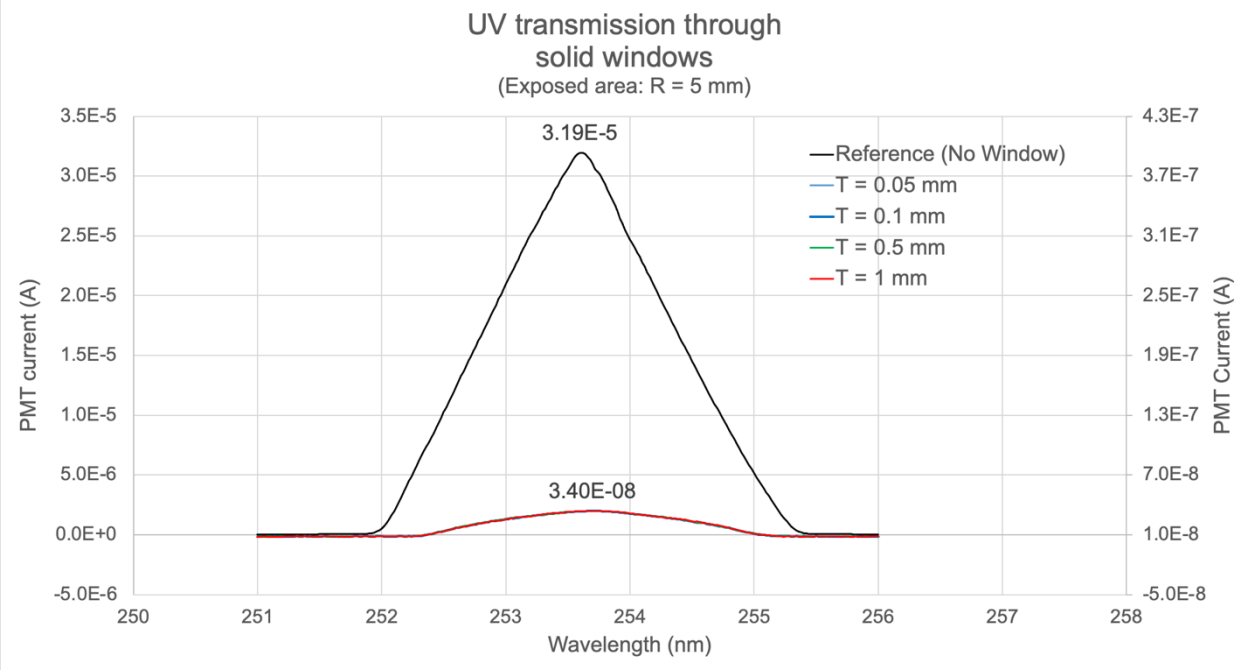

Figure 5.8 UV transmission through solid windows

with 5 mm in radius exposed area

Figure 5.8 shows very similar results to the UV transmission through solid windows with an exposed area with a 4-mm radius: (1) The transmitted spectra through solid windows are overlapped, which means these solid windows with a range of thickness show a similar UV transmission. (2) The UV transmission through these solid windows is calculated to be 0.08% by equation (5.1) with the thermal noise level measured at 1×10^{-8} amperes. Comparing to the UV transmission results with 4 mm in radius of the round exposed area, which is 0.11%, the difference can be neglected.

Besides the normal incidence, the UV transmission through solid windows with oblique incidence was also measured. However, with an oblique incidence, the UV transmission through solid windows is less than the normal incidence. The transmitted intensity of the UV radiation through solid windows with an oblique incidence was measured around 1×10^{-8} amperes, which is very close to the thermal noise level. This means the solid windows show very limited UV transmission with an oblique incidence.

The results of the experimental measurements are also compared to the results of the theoretical calculations mentioned in chapter 3. Using one of the solid windows with 0.05 mm in thickness as an example, the transmission of UV radiation at 253.6 nm through this solid window is calculated to be 1.08×10^{-13} % with normal incidence with an exposed area of 5 mm in radius. The experimental results show that the experimental UV transmission through this solid window was measured at 0.08% under the same condition. In addition, with a 5-degree incident angle, the theoretical transmission of UV radiation at 253.6 nm through this solid window is calculated to be 1.03×10^{-13} % with an exposed area of 5 mm in radius.

Therefore, based on both the experimental and theoretical results, these solid windows can transmit very limited UV radiation at 253.6 nm in wavelength.

5.2 VUV transmission measurements

Besides measuring the UV transmission through capillary-array windows and solid windows, the VUV transmission measurements for all capillary-array windows and the solid windows has also been done with two levels of exposed area of the window and different incident angles of the radiation.

5.2.1 Nanoporous capillary-array windows

To start with, the transmission of the VUV radiation at both 104.8 and 106.6 nm with normal incidence through both nanoporous capillary-array window samples with 4 mm in radius exposed area is shown in Figure 5.9.

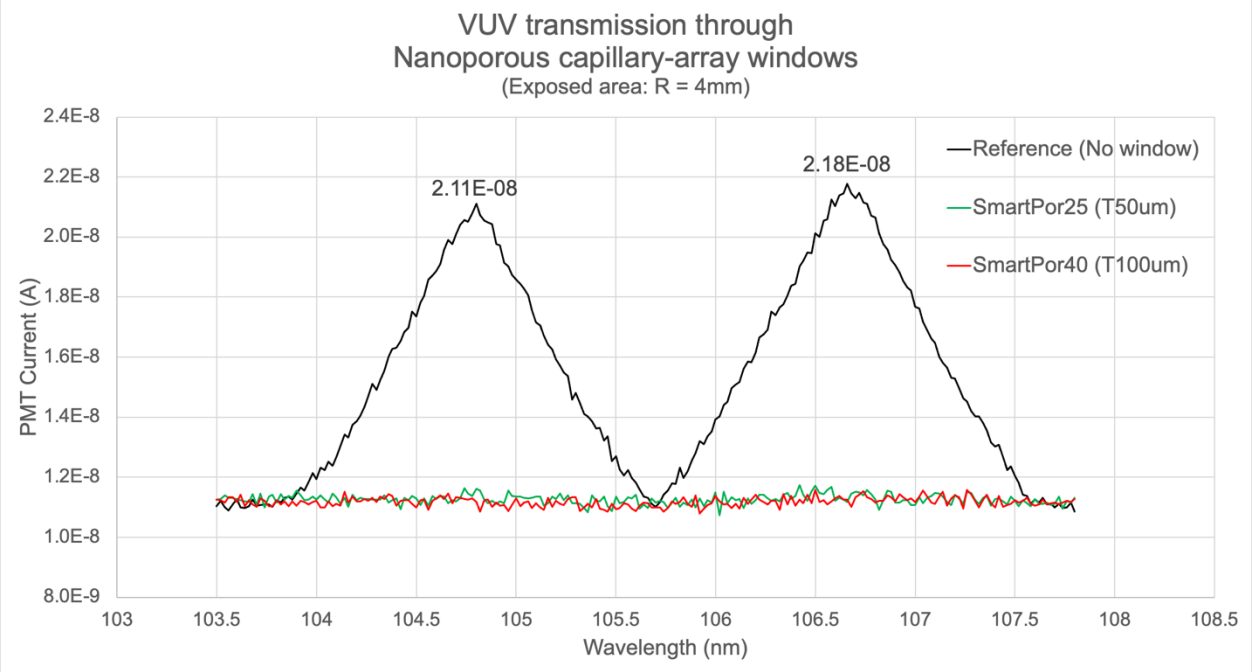

Figure 5.9 VUV transmission through nanoporous capillary-array windows with 4 mm in radius exposed area

In Figure 5.9, the black curve represents for the reference VUV spectrum, which includes the VUV peaks at 104.8 and 106.6 nm measured without a nanoporous capillary-array window. The reference spectrum shows that the intensities of the VUV peaks are both 2.11×10^{-8} amperes. The green curve is the VUV transmitted spectrum through SmartPor25, and the red curve is the VUV transmitted spectrum through SmartPor40.

From Figure 5.9, it is hardly to tell whether there is any VUV peak at either 104.8 or 106.6 nm in both transmitted spectra. Moreover, the intensities of both transmitted spectra are shown in the range of 1.1×10^{-8} amperes, which is very much the same as the thermal noise level measured from all the VUV experiments.

The VUV transmission through both nanoporous capillary-array windows with 5 mm in radius exposed area was also measured with normal incidence, which is shown in Figure 5.10.

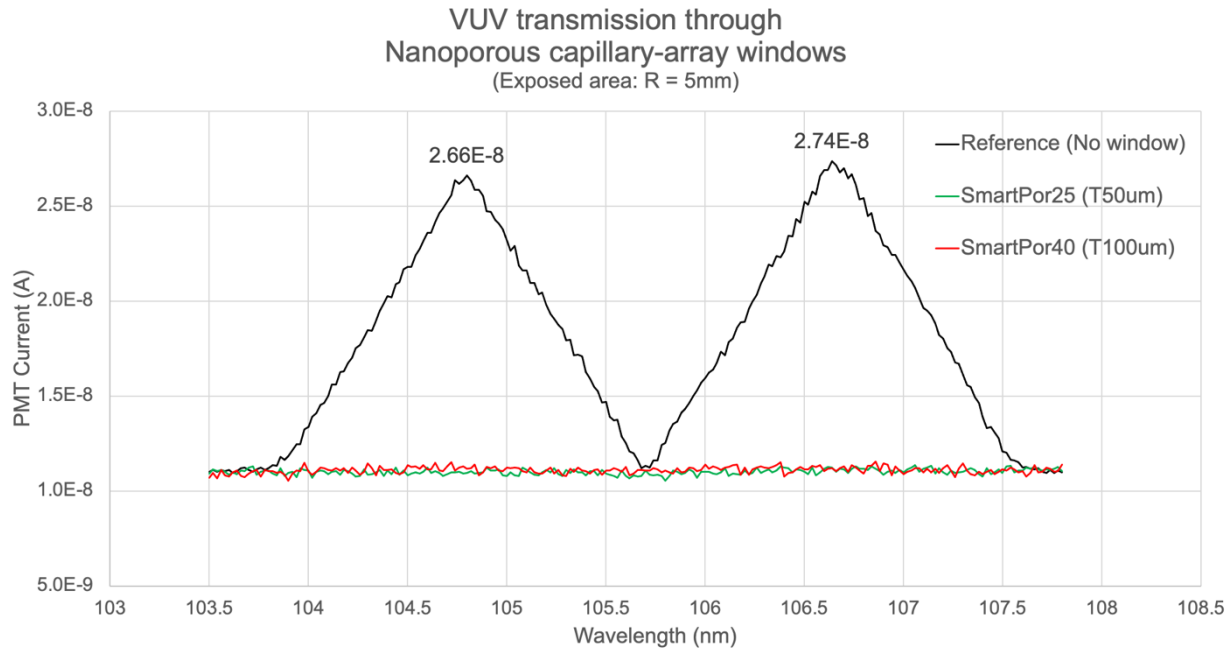

Figure 5.10 VUV transmission through nanoporous capillary-array windows with 5 mm in radius exposed area

In Figure 5.10, the black curve represents the reference VUV spectrum measured without a nanoporous capillary-array window. The intensities of the reference VUV peaks both measured as 2.11×10^{-8} amperes. The similar transmitted spectra are shown in Figure 5.10 compared with Figure 5.9, where the green curve represents the VUV transmitted spectrum through SmartPor25, and the red curve is the VUV transmitted spectrum through SmartPor40.

Besides the normal incidence, the transmission of the VUV radiation through the nanoporous capillary-array windows with a 5-degree incident angle was also measured. However, the experimental results showed there is nearly no transmitted VUV radiation that can be detected by the PMT at the exit of the nanoporous capillary-array windows, either.

As mentioned in Chapter 3, using 104.8 and 106.6 nm as the wavelengths of the incident VUV radiation, the transmission through the nanoporous capillary-array windows was calculated to be less than 10^{-50} in percentage with no matter normal incidence or a 5-degree incident angle.

Therefore, based on both the theoretical and experimental results, we concluded that there is no VUV radiation at either 104.8 or 106.6 nm in wavelength that can be transmitted through these nanoporous capillary-array window samples used in this project.

5.2.2 Microporous capillary-array windows

The transmitted VUV spectra through microporous capillary-array windows along with the reference VUV spectrum without placing a microporous capillary-array window were measured, and the experimental results will be presented in this section.

Recalling the dimensions of the microporous capillary-array window samples, there are (1) two levels for the pore diameter, which are 25 μm and 50 μm; (2) two levels for the thickness, which are 0.5 mm and 1 mm; (3) two levels for the OAR, which are 50% and 60%. The detailed dimensions of each window sample that was used for measuring the VUV transmission properties are listed in Table 2.2 of Chapter 2.

To start with, the VUV transmission through microporous capillary-array windows with 4 mm in radius exposed area is shown in Figure 5.11. Here, the incident radiation is propagating normal to the microporous capillary-array window surface.

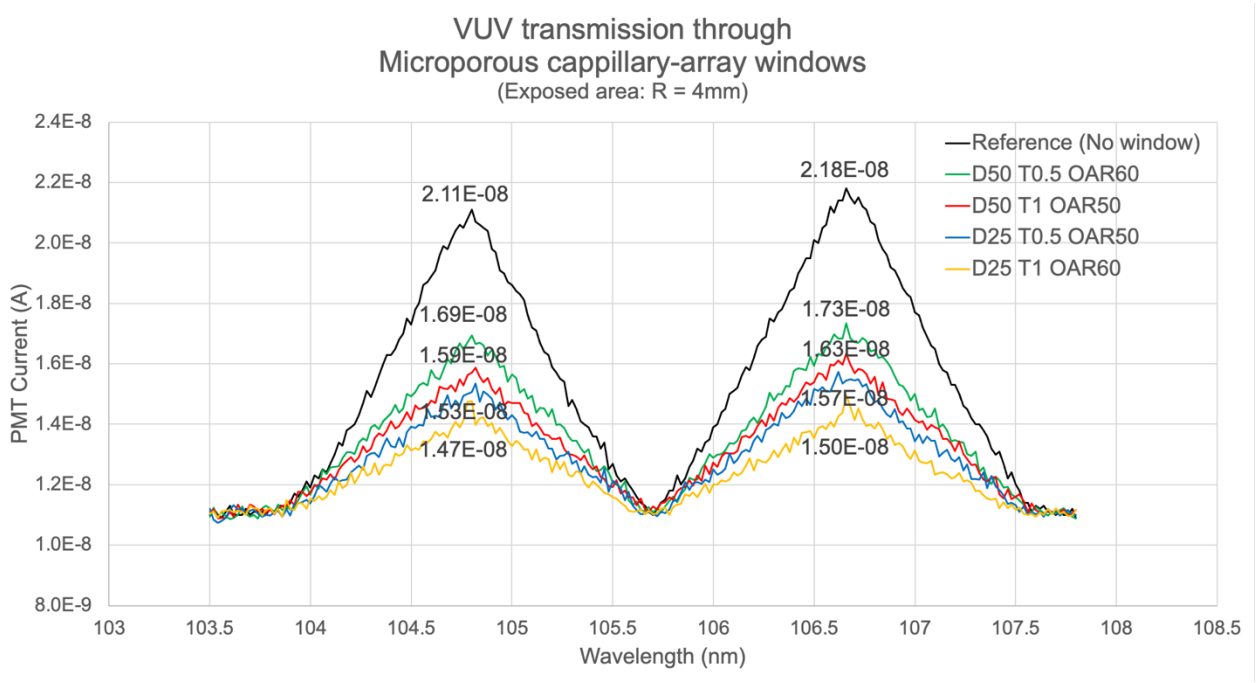

Figure 5.11 VUV transmission through microporous capillary-array windows with 4 mm in radius exposed area

In Figure 5.11, the black curve represents for the reference VUV spectrum, which is the VUV peaks at 104.8 and 106.6 nm measured without a microporous capillary-array window. The intensities of the reference peaks are 2.11×10^{-8} at 104.8 nm and 2.18×10^{-8} amperes at 106.6 nm as the current collected by the PMT. The other spectra are those transmitted through the microporous capillary-array windows. The dimension of each microporous capillary-array window is listed on the legend, with D representing the diameter in μm, T represents for thickness in mm, and OAR stands for the open area ratio in percentage. The VUV transmission ratio through these microporous capillary-array windows can be determined by equation (5.1) with the same thermal noise level measured at 1.1×10^{-8} amperes.

The VUV transmission through microporous capillary-array windows with 5 mm in radius exposed area was also measured and is shown in Figure 5.12. Again, the incident radiation is propagating normal to the microporous capillary-array window surface.

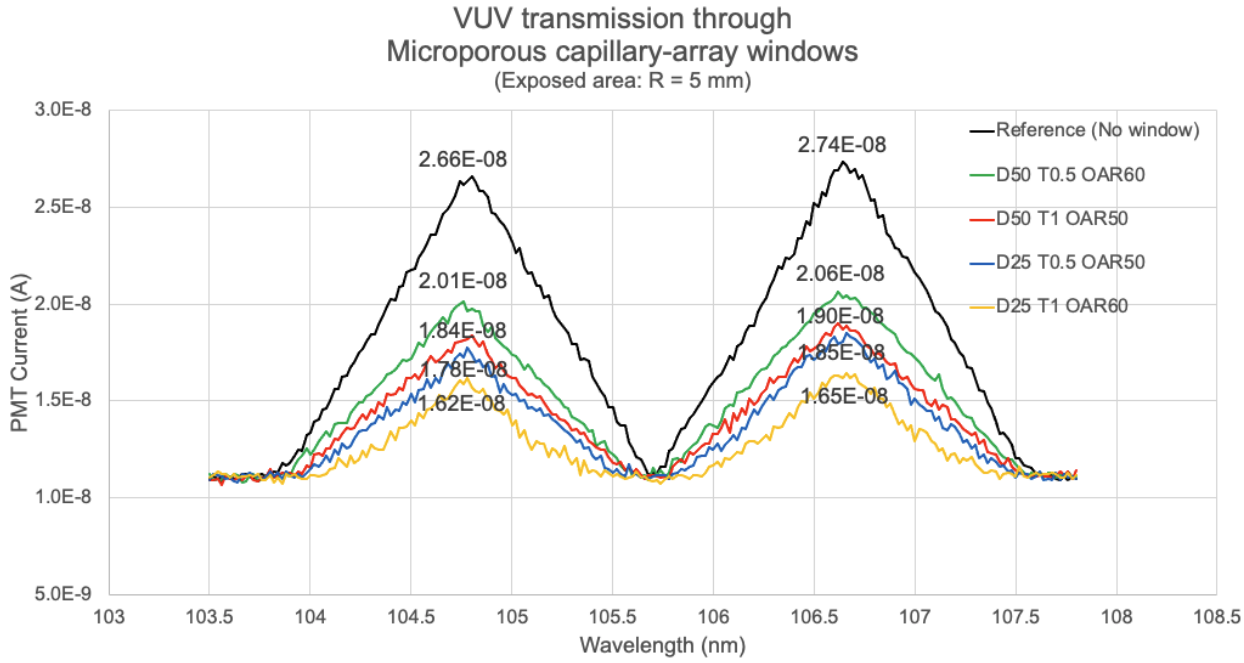

Figure 5.12 UV transmission through microporous capillary-array windows with 5 mm in radius exposed area

Besides normal incidence, the VUV transmission through these microporous capillary-array windows with 5-degree incident angle was also measured. Table 5.3 summarizes the VUV transmission ratio through the microporous capillary-array windows with multiple dimensions, exposed areas, as well as the wavelengths and the angles of the incident VUV radiation.

Diameter (μm)	Thickness	OAR	Exposed area	Wavelength	Incident angle	Transmission
50	0.5	60	4	105	0	58.41%
50	1	50	4	105	0	48.51%
25	0.5	50	4	105	0	42.57%
25	1	60	4	105	0	36.63%
50	0.5	60	5	105	0	58.33%
50	1	50	5	105	0	47.44%
25	0.5	50	5	105	0	43.59%
25	1	60	5	105	0	33.18%
50	0.5	60	4	105	5	3.41%
50	1	50	4	105	5	0.40%
25	0.5	50	4	105	5	1.35%
25	1	60	4	105	5	0.31%
50	0.5	60	5	105	5	3.83%
50	1	50	5	105	5	1.08%
25	0.5	50	5	105	5	0.83%
25	1	60	5	105	5	0.09%

Table 5.3 Summary of VUV transmission through microporous capillary-array windows

From Table 5.3, we can see microporous capillary-array windows have perform differently transmitting VUV radiation due to their different dimensions. However, while comparing the transmission with two different exposed areas, it doesn't show much difference. We can also easily tell from Table 5.3 that when there is a 5-degree incident angle of the UV radiation, the transmission drops dramatically.

We also compare the results of the experimental measurements to the results of the calculations mentioned in Chapter 3. Using one of the microporous capillary-array windows with 50 μm in pore diameter, 0.5 mm in thickness and 60% in OAR as an example, the transmission of VUV radiation at 104.8 nm through this window is calculated to be 60% with normal incidence and an exposed area with 4 mm in radius. As shown in Table 5.3, the experimental results show that the experimental VUV transmission through this window was measured at 58.41% under the same condition, which is very close to the results of the theoretical calculation.

In addition, with a 5-degree incident angle, the theoretical transmission of VUV radiation at 104.8 nm through this window is calculated to be 3.103% with an exposed area of 4 mm in radius.

As shown in Table 5.3, the experimental results show that the experimental UV transmission through this window was measured at 3.41% under the same condition, which is also in good agreement with the experimental results.

5.2.3 Milliporous capillary-array windows

The transmitted VUV spectra through milliporous capillary-array windows along with the reference VUV spectrum without a milliporous capillary-array window were measured, and the experimental results will be presented in this section.

Recalling the dimensions of the milliporous capillary-array window samples, there are (1) two levels for the pore diameter, which are 1 and 1.50 mm; (2) two levels for the thickness, which are 0.5 and 1 mm; (3) two levels for the OAR, which are 20% and 44%. The detailed dimensions of each milliporous capillary-array window sample that was used for measuring the VUV transmission properties are listed in Table 2.3 of Chapter 2.

To start with, the VUV transmission through milliporous capillary-array windows with 4 mm in radius exposed area is shown in Figure 5.13. Here, the incident radiation is propagating normal to the microporous capillary-array window surface.

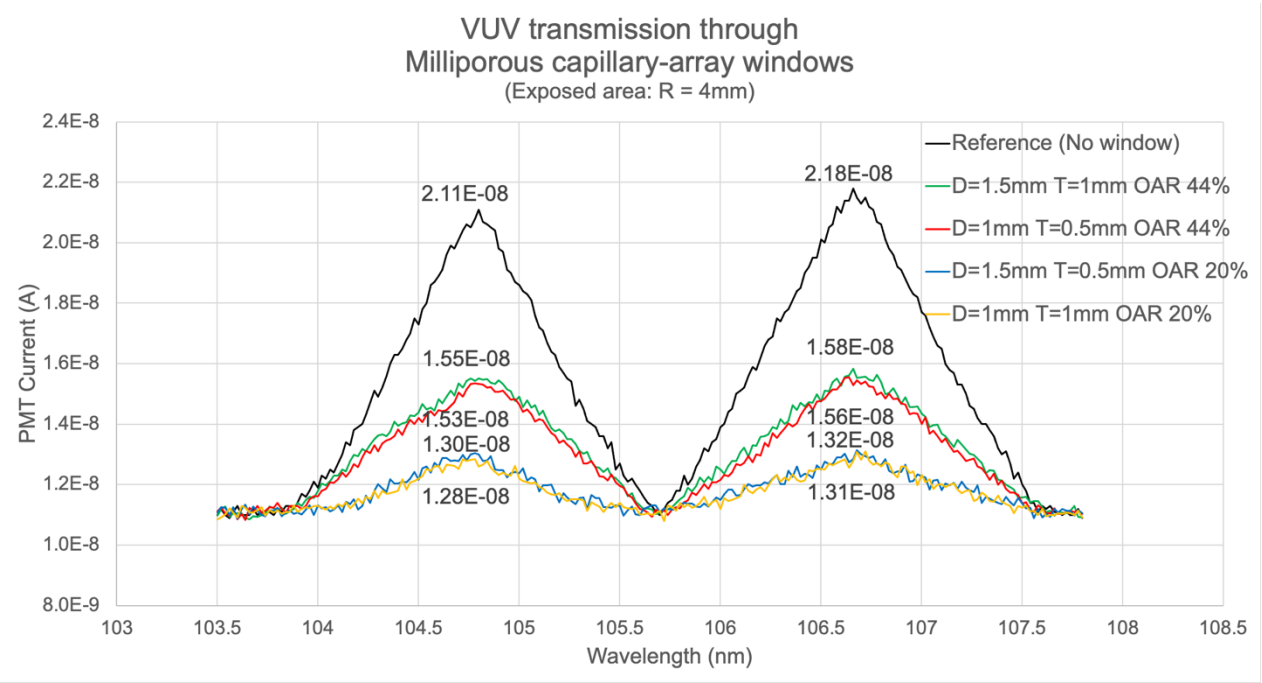

Figure 5.13 VUV transmission through milliporous capillary-array windows with 4 mm in radius exposed area

In Figure 5.13, the black curve represents the reference VUV spectrum, which are the VUV peaks at 104.8 and 106.6 nm measured without a milliporous capillary-array window. The other spectra are the transmitted spectra through the milliporous capillary-array windows. The dimension of each milliporous capillary-array window is listed on the legend. The VUV transmission ratio through these milliporous capillary-array windows can be determined by equation (5.1) with the thermal noise level measured at 1.1×10^{-8} amperes.

The VUV transmission through milliporous capillary-array windows with 5 mm in radius exposed area was also measured and is shown in Figure 5.14. Again, the incident radiation is propagating normal to the milliporous capillary-array window surface.

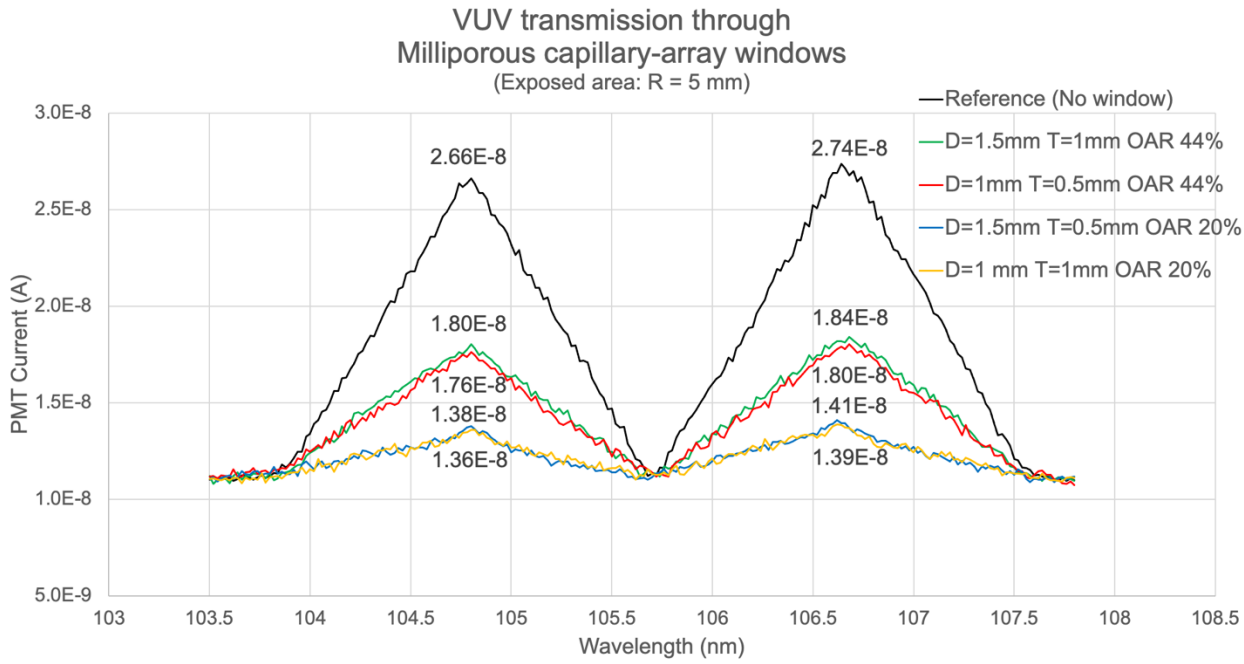

Figure 5.14 VUV transmission through milliporous capillary-array windows with 5 mm in radius exposed area

Besides the normal incidence, the VUV transmission through these milliporous capillary-array windows with 5-degree incident angle was also measured. Table 5.4 is summarizes the VUV transmission ratio through the milliporous capillary-array windows with multiple dimensions, exposed areas, as well as the wavelengths and the angles of the incident radiation.

Diameter (mm)	Thickness (mm)	OAR (%)	Exposed area (R:mm)	Wavelength (nm)	Incident angle (degree)	Transmission
1.5	1	44	4	105	0	44.55%
1	0.5	44	4	105	0	42.57%
1.5	0.5	20	4	105	0	19.80%
1	1	20	4	105	0	17.82%
1.5	1	44	5	105	0	44.87%
1	0.5	44	5	105	0	42.31%
1.5	0.5	20	5	105	0	18.90%
1	1	20	5	105	0	17.68%
1.5	1	44	4	105	5	43.23%
1	0.5	44	4	105	5	40.12%
1.5	0.5	20	4	105	5	19.46%
1	1	20	4	105	5	17.52%
1.5	1	44	5	105	5	43.54%
1	0.5	44	5	105	5	38.84%
1.5	0.5	20	5	105	5	18.66%
1	1	20	5	105	5	15.20%

Table 5.4 Summary of VUV transmission through milliporous capillary-array windows

From Table 5.4, we can see milliporous capillary-array windows perform differently when transmitting VUV radiation due to different dimensions. When comparing the exposed areas, it doesn't show much difference. In addition, when there is a 5-degree incident angle, the UV transmission through milliporous capillary-array windows drops less significantly compared to the microporous capillary-array windows. The reason is that milliporous capillary-array windows have a much greater pore diameter to thickness ratio than microporous capillary-array windows. As mentioned in section 3.2.3, due to a smaller pore diameter to thickness ratio, more radiation will hit the inside wall of the pore with an incident angle, and that means that radiation will be fully absorbed by the solid part of the window. Therefore, when there is an incident angle, more radiation can be transmitted through the milliporous capillary-array windows.

We also compare the results of the experimental measurements to the results of the calculations mentioned in Chapter 3. Using one of the milliporous capillary-array windows with 1 mm in pore diameter, 0.5 mm in thickness and 44% in OAR as an example, the transmission of VUV radiation at 104.8 nm through this window is calculated to be 44% with normal incidence

and an exposed area with 4 mm in radius. As shown in Table 5.4, the experimental results show that the experimental VUV transmission through this window was measured at 42.57% under the same condition, which is very close to the results of the calculation.

In addition, with a 5-degree incident angle, the transmission of VUV radiation at 104.8 nm through this window was calculated to be 41.23% with an exposed area of 4 mm in radius. As shown in Table 5.4, the experimental results show that the experimental UV transmission through this window was measured to be 40.12% under the same conditions, which is also in good agreement with the experimental results.

5.2.4 Thin solid windows

The VUV transmission through solid windows has also been measured to give a comparison to the VUV transmission through capillary-array windows. The solid window samples used to measure the VUV transmission here has no open area, thus, we only consider the thickness of the window as one of the factors that represents the dimension of the window. The thickness of the solid-window samples has been chosen as 0.05, 0.1, 0.5, and 1 mm to compare to the capillary-array window which has the same thicknesses.

We also consider two levels of exposed area for measuring the VUV transmission through these thin solid windows to be consistent with the measurements for capillary-array windows. The results of the VUV transmission through solid windows with normal incidence is first discussed. Figure 5.15 shows the VUV transmission through thin solid windows with an exposed area which has a 4-mm radius.

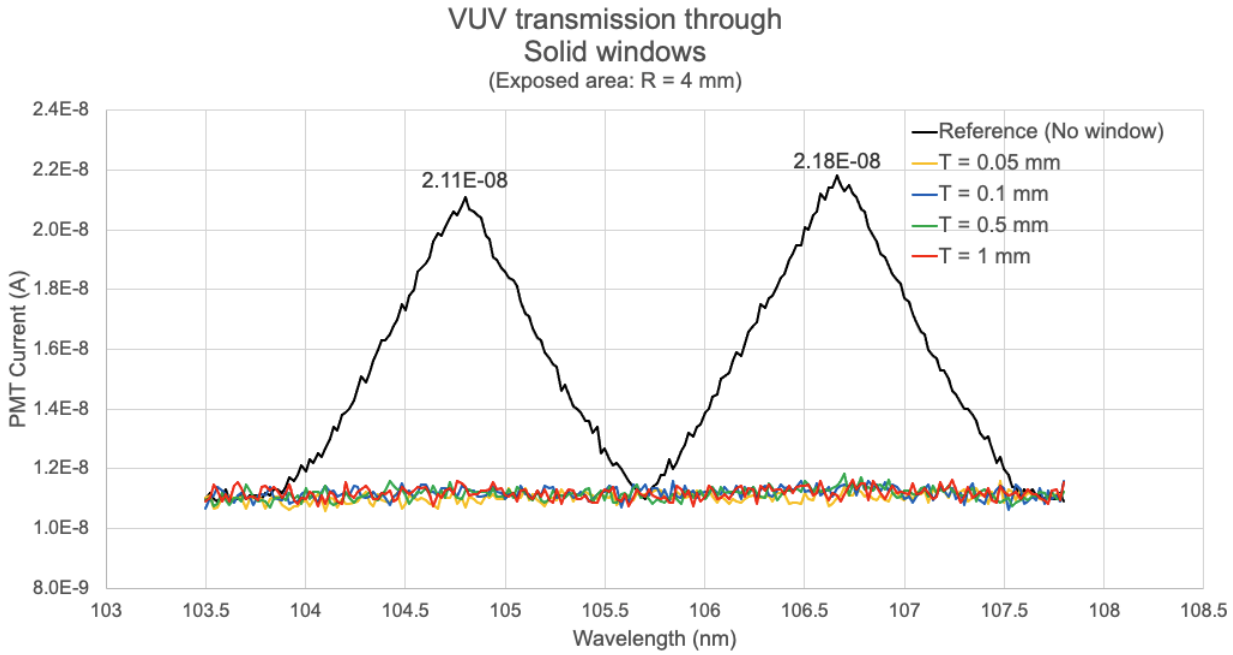

Figure 5.15 VUV transmission through solid windows

with 4 mm in radius exposed area

In Figure 5.15, the black curve represents for reference VUV spectrum without a solid window. The other spectra are the transmitted spectra through solid windows. The thickness of each solid window is listed on the legend. The transmitted spectra through solid windows with different thicknesses are overlapped, which means there is pretty much the same amount of VUV radiation which can be transmitted through these solid windows even though they are different in thickness. The VUV transmission ratio through these solid windows is hard to calculate because the intensity of the transmitted radiation is in the same range as the level of the thermal noise, which is measured at approximately 1.1×10^{-8} amperes. This means very little of the VUV radiation can transmit through the solid windows.

Figure 5.16 shows the VUV transmission through these thin solid windows with an exposed area which has a 5-mm radius.

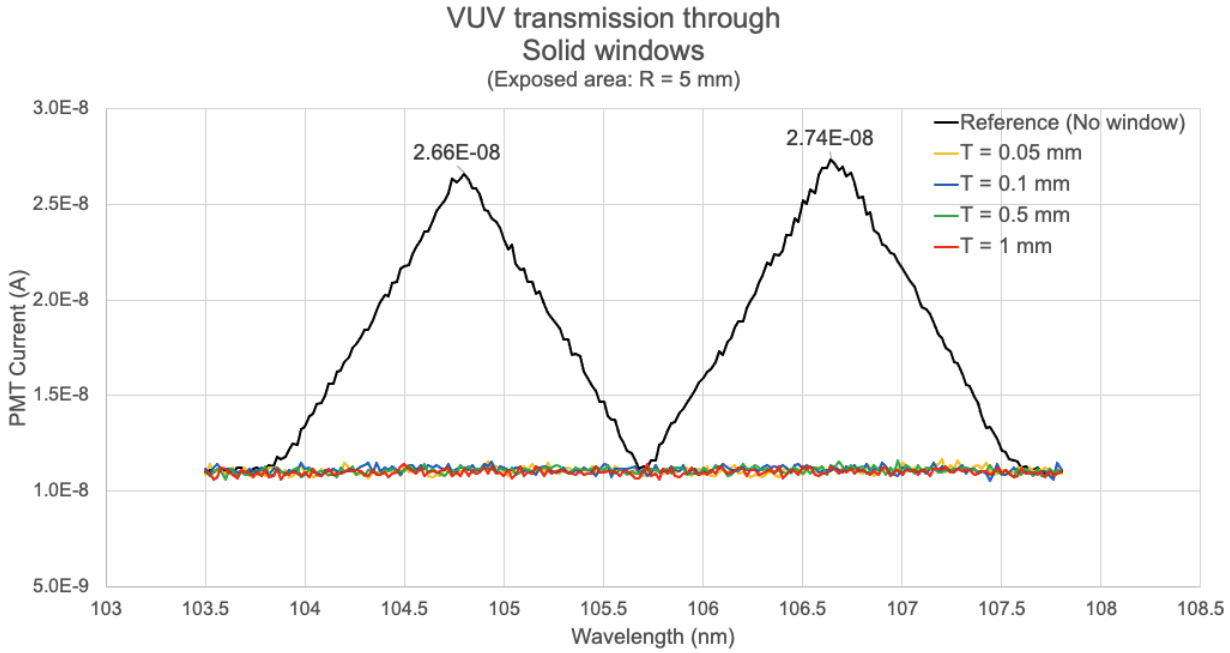

Figure 5.16 VUV transmission through solid windows

with 5 mm in radius exposed area

In Figure 5.16, it shows very similar results of the VUV transmission through solid windows with an exposed area with a 4-mm radius: (1) The transmitted spectra through solid windows are overlapped, which means these solid windows with a range of thickness performance a similar UV transmission. (2) The VUV transmission through these solid windows is hard to calculate because the intensity of the transmitted VUV radiation is in the same range as the thermal noise level. Compared to the UV transmission results with 4 mm in radius exposed area, the conclusion is the same, which is that very little VUV radiation can be transmitted through these solid windows.

Besides the normal incidence, the VUV transmission through solid windows with oblique incidence was also measured. However, with an oblique incidence, the VUV transmission through solid windows is also very limited.

The results of the experimental measurements are also compared to the results of the calculations mentioned in Chapter 3. Using one of the solid windows with 0.1 mm in thickness as an example, the transmission of VUV radiation at 104.8 nm through this solid window is calculated to be less than 10^{-300} % with normal incidence and an exposed area with 5 mm in radius. The experimental results show that the experimental VUV transmission through this solid window was also measured to be very small under the same condition. In addition, with a 5-degree incident angle, the theoretical transmission of UV radiation at 253.6 nm through this solid window is also calculated to be less than 10^{-300} % with an exposed area of 5 mm in radius.

Therefore, based on both the experimental and calculated results, these solid windows are very limited in transmitting VUV radiation at 104.8 nm in wavelength.

5.3 Reference

(1). J. D. Chatterton, G. S. Upadhyaya, J. L. Shohet, J. L. Lauer, R. D. Bathke, and K. Kukkady, J. Appl. Phys. 100, 043306 (2006).

(2) T. Lucatorto B, T. J. Mcllrath, and J. R. Roberts, Appl. Opt. 18, 2505 (1979)

(3). Laser Components, “Pen-ray Light Sources”, 11SC-1 UV lamp, 45 bis Route des Gardes, 92190, Meudon, France.

Chapter 6 – Statistical Analysis

The transmission measurements of capillary-array windows discussed in Chapter 5 were acquired through statistical experimental design. This work implemented two methods for this purpose, one being the utilization of resolution VI fractional-factorial design, [1,2] and the other being an advanced-design approach as discussed in Section 4.3.3 of Chapter 4, which is involved a combination of a resolution III fractional-factorial design, also known as an initial screen test, and a half-fractional factorial design. [1,2]

In this Chapter, we undertake a comparative analysis of the statistical evaluation of experimental data obtained by utilizing these two distinct design methods. Our aim is to identify the best approach that offers adequate results of predicting the optimal transmission efficiency through capillary-array windows with minimum number of experimental trials. To accomplish this objective, we analyze the effects of each factor, as well as the interaction effects of various factor combinations, and determine the significance levels to ascertain the influential factors. [3] We employ regression analysis to predict the optimized value of the response variable, which is the optical transmission through capillary-array windows in this case. [4,5]

The statistical analysis has been carried out on the experimental results of optical transmission through microporous and milliporous capillary-array windows. However, the statistical analysis has not been applied to the results of transmission through nanoporous capillary-array windows due to their limited transmission capacity for both UV and VUV radiation, which can confound and inaccurately affect the statistical-analysis results.

6.1 Resolution VI fractional-factorial design

In this section, the Resolution VI fractional-factorial design method is discussed. This method was implemented on the measurements of optical transmission through both microporous and milliporous capillary-array windows.

6.1.1 Microporous Capillary-array windows

The statistical analysis on the experimental results of optical transmission through microporous capillary-array windows utilizing the resolution VI fractional-factorial design method is presented in this section.

As discussed in Chapters 2 and 4, our investigation of the optical transmission through microporous capillary-array windows encompasses six factors, which are: (A) pore diameter; (B) thickness of the window; (C) Open Area ratio (OAR); (D) exposed area; (E) wavelength of the incident radiation; and (F) incident angle of the radiation. For each factor, we consider two levels, specifically low and high, with predefined values for each level.

Considering the six factors, each with two levels, the implementation of the Resolution VI fractional-factorial design method necessitates a total of 32 experimental trials. This represents a notable reduction of 50% when compared to the conventional approach, which would typically require 64 trials of experiment in the absence of any experimental design methodology.

By compiling the experimental results presented in Tables 5.1 and 5.3 in Chapter 5, we obtain a comprehensive dataset of the optical transmission through microporous capillary-array windows, as shown in Table 6.1. This dataset can be subjected to statistical analysis using the resolution VI fractional-factorial design.

	Diameter (μm)	Thickness (mm)	OAR (%)	Exposed area (R:mm)	Wavelength (nm)	Incident angle (degree)	Transmission
1	50	0.5	60	5	253	0	58.93%
2	50	1	50	5	253	0	46.01%
3	25	0.5	50	5	253	0	45.77%
4	25	1	60	5	253	0	37.93%
5	50	0.5	60	4	253	0	58.82%
6	50	1	50	4	253	0	46.51%
7	25	0.5	50	4	253	0	43.78%
8	25	1	60	4	253	0	37.60%
9	50	0.5	60	5	105	0	58.33%
10	50	1	50	5	105	0	47.44%
11	25	0.5	50	5	105	0	43.59%
12	25	1	60	5	105	0	33.18%
13	50	0.5	60	4	105	0	58.41%
14	50	1	50	4	105	0	48.51%
15	25	0.5	50	4	105	0	42.57%
16	25	1	60	4	105	0	36.63%
17	50	0.5	60	5	253	5	2.16%
18	50	1	50	5	253	5	0.55%
19	25	0.5	50	5	253	5	0.51%
20	25	1	60	5	253	5	0.47%
21	50	0.5	60	4	253	5	2.35%
22	50	1	50	4	253	5	0.48%
23	25	0.5	50	4	253	5	0.46%
24	25	1	60	4	253	5	0.12%
25	50	0.5	60	5	105	5	3.83%
26	50	1	50	5	105	5	1.08%
27	25	0.5	50	5	105	5	0.83%
28	25	1	60	5	105	5	0.09%
29	50	0.5	60	4	105	5	3.41%
30	50	1	50	4	105	5	0.40%
31	25	0.5	50	4	105	5	1.35%
32	25	1	60	4	105	5	0.31%

Table 6.1 Experimental results of optical transmission through microporous capillary-array windows utilizing resolution VI fractional-factorial design

By utilizing the experimental data displayed in Table 6.1 and employing the statistical analysis methods described in Section 4.3, we can obtain the impact of each individual factor and in addition, the interaction effects resulting from combinations of multiple factors. These outcomes are presented in a Pareto chart shown in Figure 6.1.

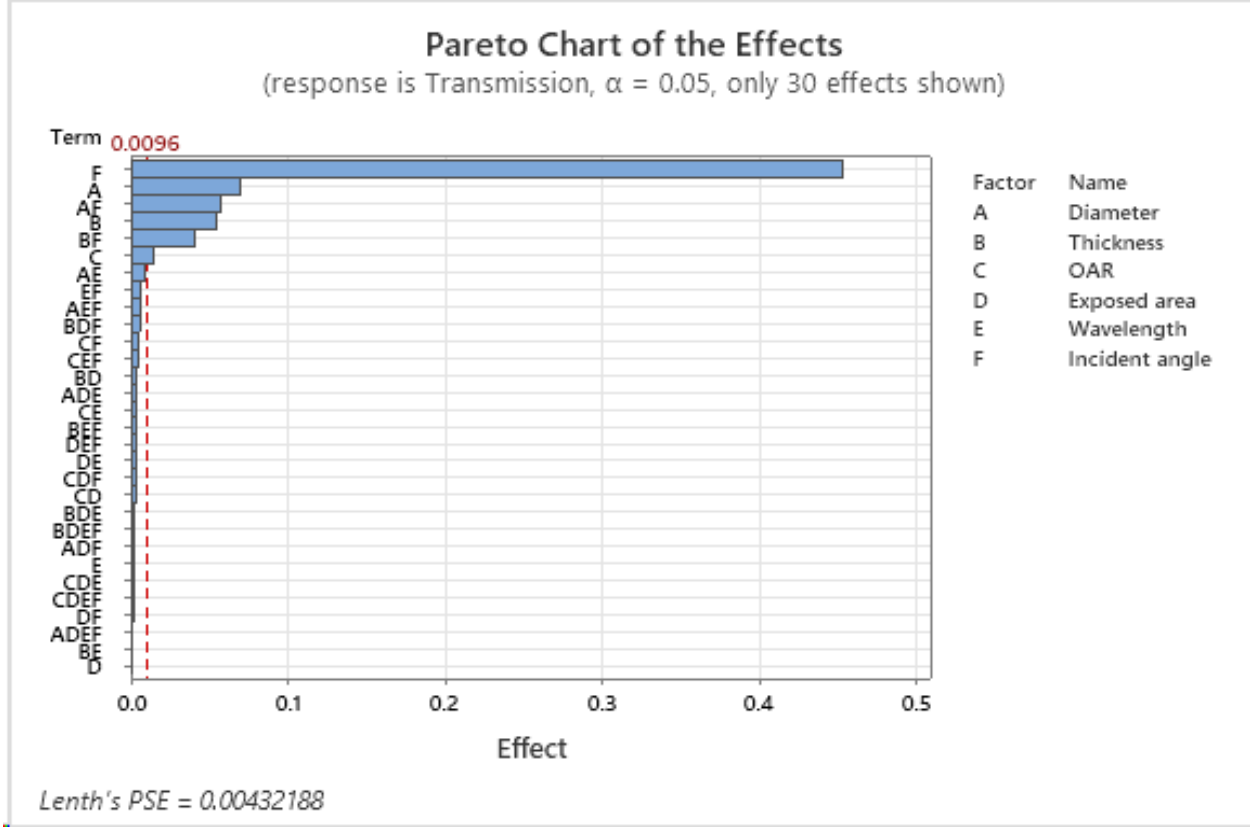

Figure 6.1 Pareto chart of the effects of each factor and their interactions for the microporous capillary-array windows utilizing resolution VI fractional-factorial design (32 experiments)

In Figure 6.1, only 30 effects are displayed due to the fact that the remaining effects were found to be negligible in terms of their impact on the transmission efficiency through the microporous capillary-array windows. It is important to note that α, which represents the confidence level, is typically set at 0.05 in statistical analysis. This signifies that there is a 5% chance of erroneously rejecting the null hypothesis when it is actually true. Moreover, this level of α also implies that there is a 95% likelihood of obtaining the same experimental outcomes upon duplication of the experiments. The value of the significant level at 95% can be computed using the ANOVA calculation approach discussed in Chapter 4, and the red-dashed vertical line depicted

in Figure 6.1 corresponds to the reference confidence line of the significant level at 95%. [4] For instance, if the effect value of a factor or interaction surpasses the reference line, we can assert with 95% confidence that the factor or interaction has a significant influence on the response variable, which in this case, refers to the optical transmission efficiency. [4] Furthermore, regardless of the number of experiments replicated, there is a 95% chance of obtaining the same effects of that factor on the response variable. Conversely, if the effect value of a factor or interaction falls well below the reference line, it can be classified as an insignificant factor, indicating that its impact on the response variable is extremely limited.

The normalized values of the effect of each single factor and the reference line shown in Figure 6.1 are calculated using the equation (4.1) in Chapter 4, and the values are listed as follows:

$$F(Incident\ angle) = 0.4535;$$

$$A(Pore\ diameter) = 0.07002;$$

$$B(Thickness) = 0.05487;$$

$$C(OAR) = 0.014206;$$

$$Reference\ line = 0.0096;$$

$$E(Wavelength) = 0.001556;$$

$$D(Exposed\ area) = 0.000631;$$

In statistical analysis, the normalized effect value is a measure that indicates the change in the response variable when a given factor is modified by one level while holding the other factors constant. For instance, we investigate the impact of the factor incident angle on the transmission efficiency through the capillary-array windows, considering two levels of 0 and 5 degrees. The normalized effect value of the incident angle on the response variable is estimated to be 45.35%, indicating that if we changed the level of the incident angle from one to the other, for example,

from normal incidence to an incident angle of 5 degree, the transmission efficiency through the capillary-array windows is going to be reduced by 45.35%.

From what has been shown in Figure 6.1 and the effect value of each factor, we can draw the following conclusions:

(1) The Incident angle factor, which is the incident angle of the radiation, has the most significant influence on the optical-transmission efficiency through microporous capillary-array windows.
(2) The factors Incident angle (F), pore diameter (A), Thickness of the window (B), and OAR (C) all have significant influence on the transmission efficiency, while the factors Wavelength (E) and Exposed area (D) have very limited effects.
(3) The order of the importance level of each factor is: $F > A > B > C > Reference\ line > E > D$.

Regrettably, the Pareto chart of effects presented in Figure 6.1 does not provide any indication of whether the factors have a positive or negative impact on the response variable. However, regression analysis can provide valuable insights into (1) the direction of the effect resulting from the modification of the factors, and (2) the nature of the relationship between the response variable and each factor and their corresponding interactions.

Using the calculation of regression analysis mentioned in Section 4.3, we obtain the regression equation [5] for the transmission efficiency as follows:

$$\begin{aligned}\text{Transmission efficiency} = {} & 0.2383 + 0.03501A - 0.02743B + 0.007103C - 0.000316D \\ & + 0.000778E - 0.2268F - 0.02868AF + 0.02031BF \\ & + 0.004278AE - 0.003403EF + \cdots \end{aligned} \quad (6.1)$$

From the regression equation listed above, the following information can be drawn:

(1) We can discern the direction of transmission changes resulting from modifications to individual factors or their interactions. For instance, factor pore diameter (A) exhibits a positive effect on transmission, whereby increasing the pore diameter will lead to increased transmission efficiency.

(2) The magnitude of influence resulting from alterations to each factor or interaction can also be determined. For instance, an increase in the level of factor Thickness (B), representing an increase in the thickness of the microporous capillary-array window from 0.5 mm to 1 mm, will result in a 5.487% decrease in the transmission ratio.

(3) The signs and coefficients of the *interaction* terms indicate the direction and extent of transmission efficiency changes resulting from the modification of multiple factors simultaneously. For instance, if both factors A pore diameter and F incident angle are increased by one level, denoting a change in pore diameter from 25 to 50 μm and a change in incident angle from 0 to 5 degrees, the transmission efficiency will be reduced by 5.737%.

(4) The regression equation for estimating transmission efficiency may include many terms. However, many of these terms may be disregarded as they represent factors and interactions that exert negligible influence on transmission efficiency.

Furthermore, utilizing the regression equation (6.1), we can determine the maximum optical transmission attainable through microporous capillary-array windows by substituting specific levels of the factors and interactions. Thus, based on the conditions of a pore diameter of 50 μm, a window thickness of 0.5 mm, an OAR of 60%, an exposed area with a radius of 4 mm, an incident radiation wavelength of 253.6 nm, and a normal radiation with an incidence angle of 0 degrees,

the maximum achievable optical transmission through microporous capillary-array windows was found to be 59.24%.

6.1.2 Milliporous Capillary-array windows

This section presents the statistical analysis of the experimental results obtained from measuring the optical transmission through milliporous capillary-array windows using the resolution VI fractional-factorial design method.

As previously discussed in Chapters 2 and 4, the optical transmission through a milliporous capillary-array window depends on the same factors: (A) Pore Diameter, (B) Thickness of the window, (C) Open Area Ratio (OAR), (D) Exposed Area, (E) Wavelength of the incident radiation, and (F) Incident angle of the radiation. Each factor is considered at two levels, low and high, with specific values provided for each level.

Again, considering the same six factors, each with two levels, the implementation of the Resolution VI fractional-factorial design method necessitates a total of 32 experimental trials. This also represents a notable reduction of 50% when compared to the conventional approach, which would typically require 64 trials of experiment in the absence of any experimental design methodology.

The full data set of the optical transmission through milliporous capillary-array windows, obtained by combining the experimental results presented in Tables 5.2 and 5.4 in Chapter 5, which is shown in Table 6.2 and will be analyzed using the resolution VI fractional-factorial design.

Milli	Diameter (mm)	Thickness (mm)	OAR (%)	Exposed area (R:mm)	Wavelength (nm)	Incident angle (degree)	Transmission
1	1.5	1	44	5	253	0	44.07%
2	1	0.5	44	5	253	0	41.88%
3	1.5	0.5	20	5	253	0	20.81%
4	1	1	20	5	253	0	20.00%
5	1.5	1	44	4	253	0	44.62%
6	1	0.5	44	4	253	0	41.92%
7	1.5	0.5	20	4	253	0	21.14%
8	1	1	20	4	253	0	19.96%
9	1.5	1	44	5	105	0	44.87%
10	1	0.5	44	5	105	0	42.31%
11	1.5	0.5	20	5	105	0	18.90%
12	1	1	20	5	105	0	17.68%
13	1.5	1	44	4	105	0	44.55%
14	1	0.5	44	4	105	0	42.57%
15	1.5	0.5	20	4	105	0	19.80%
16	1	1	20	4	105	0	17.82%
17	1.5	1	44	5	253	5	41.81%
18	1	0.5	44	5	253	5	38.92%
19	1.5	0.5	20	5	253	5	18.70%
20	1	1	20	5	253	5	15.60%
21	1.5	1	44	4	253	5	42.27%
22	1	0.5	44	4	253	5	38.85%
23	1.5	0.5	20	4	253	5	18.93%
24	1	1	20	4	253	5	15.71%
25	1.5	1	44	5	105	5	43.54%
26	1	0.5	44	5	105	5	38.84%
27	1.5	0.5	20	5	105	5	18.66%
28	1	1	20	5	105	5	15.20%
29	1.5	1	44	4	105	5	43.23%
30	1	0.5	44	4	105	5	40.12%
31	1.5	0.5	20	4	105	5	19.46%
32	1	1	20	4	105	5	17.52%

Table 6.2 Experimental results of optical transmission through milliporous capillary-array windows utilizing resolution VI fractional-factorial design

By utilizing the statistical methods discussed in Section 4.3 and the experimental data presented in Table 6.2, we have determined the effects of individual factors and the interaction effects resulting from multiple factors in combination. The results are depicted in Figure 6.2.

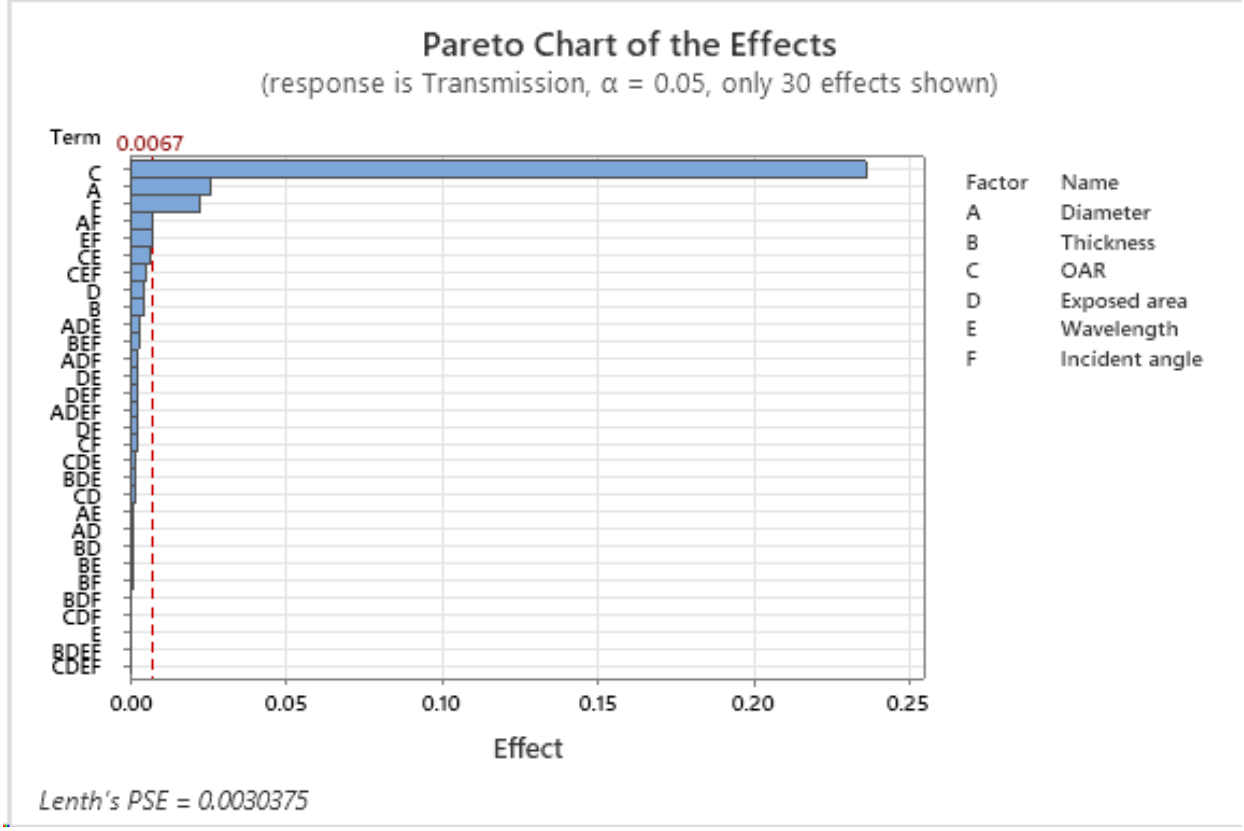

Figure 6.2 Pareto chart of the effects of each factor and their interactions for the milliporous capillary-array window with utilizing resolution VI fractional-factorial design (32 experiments)

In Figure 6.2, only 30 effects are displayed due to the insignificance of the remaining effects on the transmission efficiency through milliporous capillary-array windows. To determine the significance of each factor and interaction effect, again, a confidence level of $\alpha = 0.05$ was chosen, and a red dashed vertical line was used to represent the reference confidence line for the significance level of 95%. This implies that (1) A 5% chance of rejecting the null hypothesis is acceptable when it is true. (2) If the effect of a factor or interaction exceeds the reference line, we can assert with 95% confidence that it has a significant influence on the response variable, whereas

if the effect is considerably below the reference line, it is deemed insignificant. (3) If the experiments are duplicated, there is a 95% likelihood of obtaining the same results.

The normalized values of the effect of each single factor and the reference line shown in Figure 6.2 are as follows:

$$C(OAR) = 0.2362;$$

$$A(Pore\ diameter) = 0.0256;$$

$$F(Incident\ angle) = 0.02252;$$

$$Reference\ line = 0.0067;$$

$$D(Exposed\ area) = 0.004488;$$

$$B(Thickness) = 0.004462;$$

$$E(Wavelength) = 0.000387;$$

The normalized effect value denotes the alteration in the response variable, which in this case, is the optical transmission efficiency through milliporous capillary-array windows, that ensues when a factor is modified by one level. For instance, consider the factor C Open area ratio or OAR, which has two levels, namely 20% and 44%. A modification of the OAR level from one to the other leads to a 23.62% change in the transmission efficiency through the milliporous capillary-array windows.

From what has been shown in Figure 6.2 and the effect of each factor, we can draw the following conclusions:

(1) The factor C (OAR), which is the open-area ratio, has the most significant influence on the optical transmission efficiency through microporous capillary-array windows.

(2) The factors A (pore diameter) and F (Incident angle) also have significant influence on the transmission efficiency through milliporous capillary-array windows, while the factors D (Exposed area), B (Thickness), and E (Wavelength) have very limited effects.

(3) The order of the importance level of each factor is: $C > A > F >$ Reference line $> D > B > E$.

Despite providing information on the significance of the factors, as before, the Pareto chart of effects displayed in Figure 6.2 does not reveal whether the factors have a positive or negative impact on the response variable. However, through regression analysis, we can ascertain crucial information such as (1) the direction of change resulting from the modification of the factors, *i.e.*, whether there is a positive or negative change, and (2) the nature of the relationship between the response variable and the individual factors and their interactions.

Using the calculation of regression analysis mentioned in Section 4.3, we can obtain the regression equation as follows:

$$\begin{aligned}\text{Transmission} = {} & 0.303 + 0.0128A + 0.002231B + 0.1181C - 0.002244D + 0.000194E \\ & -0.01126F + 0.003663AF - 0.003494EF - 0.003438CE \\ & - 0.002512CEF - 0.00155ADE + \cdots \end{aligned} \tag{6.2}$$

From the regression equation listed above, the following information can be drawn:

(1) The direction of change in transmission efficiency resulting from modifications of individual factors or interactions can be determined through regression analysis. For instance, the positive effect of factor A pore diameter on transmission efficiency implies that increasing the pore diameter will result in a corresponding increase in transmission efficiency.

(2) The magnitude of the effect resulting from modifications of individual factors or interactions can also be estimated through regression analysis. For instance, a one-level increase in factor

E wavelength, which corresponds to an increase in the wavelength of the incident radiation from 105 to 253 nm, results in a 0.0387% increase in transmission ratio.

(3) The coefficients and signs of the interaction terms in the regression equation reveal the direction and magnitude of changes in transmission efficiency that result from modifications of multiple factors simultaneously. For instance, an increase in both factors E wavelength and F incident angle by one level, which corresponds to an increase in wavelength from 105 to 253 nm and an increase in incident angle from 0 to 5 degrees, results in a 0.6988% decrease in transmission efficiency.

(4) Although the regression equation contains numerous other terms, which represent factors or interactions that have minimal effect on transmission efficiency, they can be safely disregarded.

Furthermore, by utilizing the regression equation (6.2), the optimal level of each factor and interaction can be substituted to determine the maximum optical transmission through milliporous capillary-array windows. As a result, a maximum optical transmission of 45.03% can be achieved under the following conditions: a pore diameter of 1.5 mm, a window thickness of 1 mm, an OAR of 44%, an exposed area with a radius of 4 mm, an incident radiation wavelength of 253.6 nm, and a normal incidence with an incident angle of 0 degrees.

6.2 Screen test and half-fractional-factorial design

In this section, the advanced experimental-design method, as mentioned in Chapter 4, is discussed. This method starts with a resolution III fractional-factorial design, known as the screen test, followed by a subsequent half-fractional-factorial design. This method was implemented on the measurements of optical transmission through both microporous and milliporous capillary-array windows.

6.2.1 Microporous Capillary-array windows

In this section, we present an analysis of the experimental results on optical transmission through microporous capillary-array windows with employing a resolution III fractional-factorial design, known as the screen test, supplemented with a half-fractional-factorial design. We conduct ANOVA and regression analysis to investigate the effect of various factors, which are the same factors that we considered in the last section, including (A) Pore Diameter, (B) Thickness of the window, (C) Open area ratio (OAR), (D) Exposed area, (E) Wavelength of the incident radiation, and (F) Incident angle of the radiation, on the optical transmission through microporous capillary-array windows.

When considering all six factors at two levels each, the initial resolution III screen test requires only 8 experimental measurements to assess the optical transmission, while there were 32 experimental measurements were done in the previous method mentioned in the last section.

Following the methodology discussed in Chapter 4, we perform a specific group of 8 experiments to measure the optical transmission through microporous capillary-array windows. The results of the experimental measurements are presented in Table 6.3.

	A	B	C	D	E	F	
	Diameter (μm)	Thickness (mm)	Exposed area (R:mm)	OAR (%)	Wavelength (nm)	Incident angle (degree)	Transmission
1	50	1	5	50	253	5	0.55%
2	50	1	4	50	105	0	48.51%
3	50	0.5	5	60	105	5	3.83%
4	50	0.5	4	60	253	0	58.82%
5	25	1	5	60	253	0	37.93%
6	25	1	4	60	105	5	0.31%
7	25	0.5	5	50	105	0	43.59%
8	25	0.5	4	50	253	5	0.46%

Table 6.3 Screen-test results on the optical transmission through microporous capillary-array windows

With utilizing the analysis on the effects of each considered factors and their interactions plus the ANOVA analysis, the Pareto chart of the effects can be obtained, which is shown in Figure 6.3.

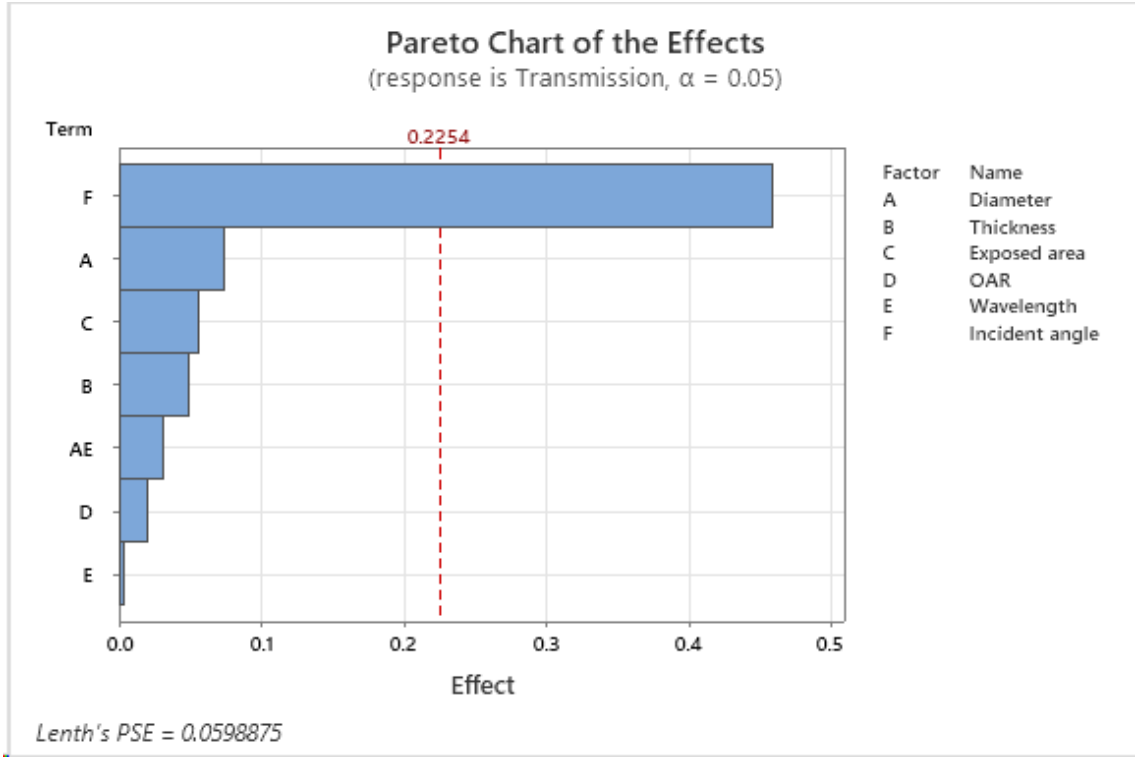

Figure 6.3 Pareto chart of the effects of each factor and their interactions for the microporous capillary-array windows utilizing screen tests (8 experiments)

In Figure 6.3, only seven effects are presented because the remaining effects were found to have negligible impact on the transmission efficiency through the microporous capillary-array windows and because a screen test with a limited number of experiments was conducted. The confidence level α was set at 5%, and the red dashed vertical line in Figure 6.3 corresponds to the significance threshold at 95%. In contrast to the previous Pareto charts of effects in Figure 6.1 and 6.2, only one effect, which is the incident angle of the radiation (F), exceeded the reference line in the Pareto chart resulting from the application of the screen test. It should be noted that the primary motivation for implementing a screen test in our project was to exclude factors with a minimal influence on transmission efficiency.

The normalized values of the effect of each single factor and the reference line shown in Figure 6.3 are as follows:

$$F(Incident\ angle) = 0.4593;$$

$$Reference\ line = 0.2254;$$

$$A(Pore\ diameter) = 0.07355;$$

$$C(Exposed\ area) = 0.0555;$$

$$B(Thickness) = 0.0485;$$

$$D(OAR) = 0.01945;$$

$$E(Wavelength) = 0.0038;$$

The factor wavelength (E) has been determined to have an insignificant effect on the optical transmission efficiency and, therefore, can be disregarded in further analysis. The primary purpose of conducting a screen test is to exclude certain factors that have a negligible impact on the response variable. However, due to the limited number of experiments conducted during a screen

test, it is not possible to obtain precise estimates of the effects of each factor on the response variable. Consequently, the information that can be gleaned from a screen test is restricted in scope. Therefore, in order to determine the most significant factors that influence the optical transmission efficiency through microporous capillary-array windows and to estimate the optimized transmission efficiency, a further experimental design using a half-fractional-factorial design was employed.

After removing the factor wavelength from further consideration, this design considered only five factors: (A) Pore Diameter; (B) Thickness of the window; (C) Open area ratio (OAR); (D) Exposed area; (E) Incident angle of the radiation. 16 measurements were taken for the half-fractional-factorial design regarding to the methodology discussed in Chapter 4 after a screen test, which involved 8 measurements. The experimental data from both designs are presented in Table 6.4.

	A	B	C	D	E	E=ABCD
	Diameter (μm)	Thickness (mm)	OAR (%)	Exposed area (R:mm)	Incident angle (degree)	Transmission
1	50	1	60	5	5	0.86%
2	50	1	60	4	0	54.41%
3	50	1	50	5	0	46.01%
4	50	1	50	4	5	0.40%
5	50	0.5	60	5	0	58.93%
6	50	0.5	60	4	5	3.41%
7	50	0.5	50	5	5	0.55%
8	50	0.5	50	4	0	48.51%
9	25	1	60	5	0	33.18%
10	25	1	60	4	5	0.12%
11	25	1	50	5	5	0.33%
12	25	1	50	4	0	38.78%
13	25	0.5	60	5	5	0.09%
14	25	0.5	60	4	0	37.60%
15	25	0.5	50	5	0	43.59%
16	25	0.5	50	4	5	0.46%

Table 6.4 Further half-fractional-factorial design experimental results on the optical transmission through microporous capillary-array windows

The same statistical analysis is applied to the experimental results on the optical transmission through microporous capillary-array windows with the half-fractional-factorial design, which was mentioned in Section 4.3.3 Chapter 4, to generate a Pareto chart of the effects, which is shown in Figure 6.4.

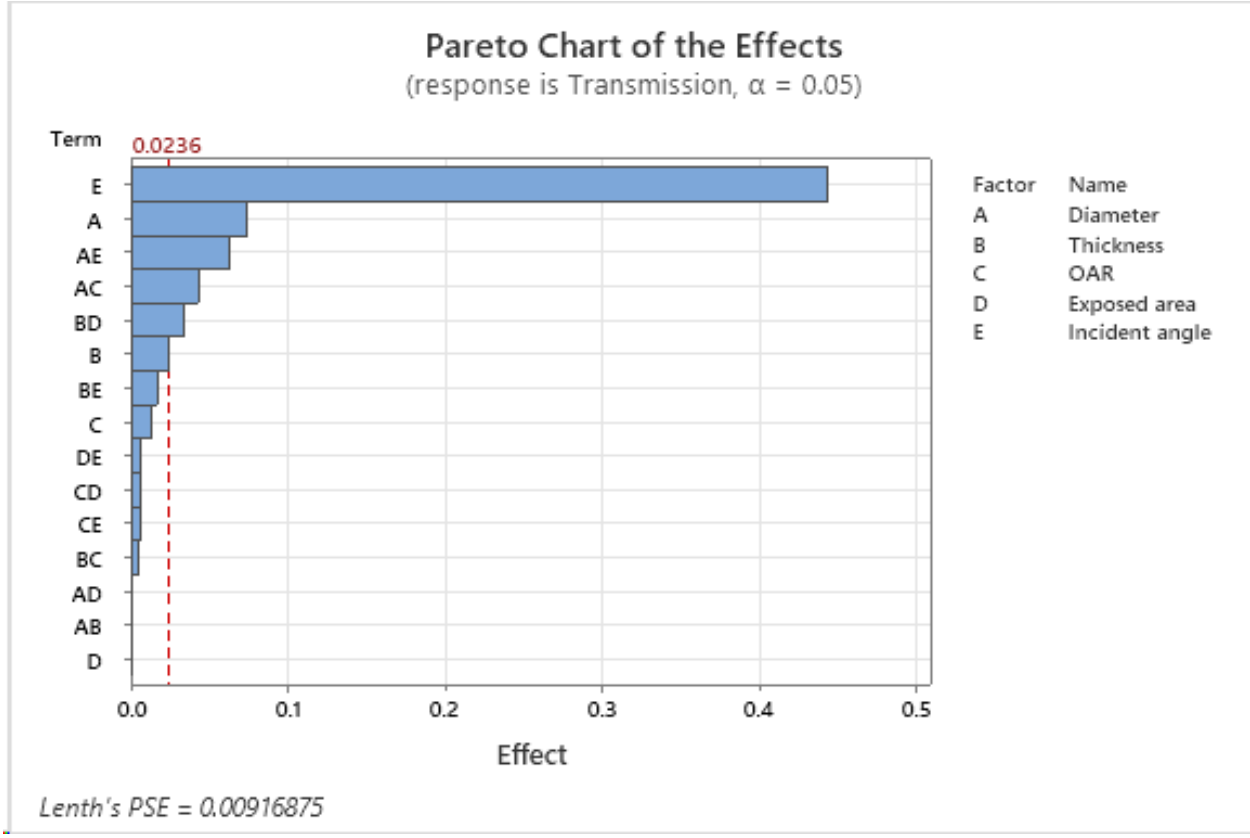

Figure 6.4 Pareto chart of the effects of each factor and their interactions for the microporous capillary-array windows using a half-fractional-factorial design (16 experiments)

Now, with more measurements were performed, we can see a further statistical analysis on the effects of each factor and the interactions shown in Figure 6.4. The normalized values of the effect of each single factor and the reference line shown in Figure 6.4 are as follows:

$$E(Incident\ angle) = 0.4435;$$

$$A(Pore\ diameter) = 0.07366;$$

$$B(Thickness) = 0.02381;$$

$$Reference\ line = 0.0236;$$

$$C(OAR) = 0.012463;$$

$$D(Exposed\ area) = 0.000187;$$

Therefore, with the help of the further half-fractional-factorial design, we get the more accurate analysis over the effects of each factor and the interactions, which will lead us to the following conclusions:

(1) The accurate reference line is determined to be at a value of 0.0236, based on our analysis.

(2) Based on the results of the screen test and the subsequent half-fractional-factorial design, we have identified that three factors - wavelength of the incident radiation, open area ratio (OAR), and exposed area - have minimal impact on the transmission efficiency through microporous capillary-array windows and can be eliminated from further consideration.

(3) Our analysis has revealed that the incident angle of the radiation is the most significant factor influencing the optical transmission efficiency through microporous capillary-array windows.

(4) Additionally, we have identified that the pore diameter and thickness of the window are also significant factors affecting the transmission efficiency through microporous capillary-array windows.

Using the calculation of regression analysis mentioned in Section 4.3, we can obtain the regression equation as follows:

$$\text{Transmission} = 0.2295 + 0.03863A - 0.01191B + 0.006231C - 0.0000094D - 0.2217E$$

$$-0.03156AE + 0.02144AC - 0.01657BD + 0.008406BE - 0.003106DE \ldots \quad (6.3)$$

where A represents for the factor pore diameter, B represents for the thickness of the window, C represents for the OAR, D represents for the exposed area, and E represents for the incident angle of the radiation. Those cross terms, such as AE, AC and BD, listed in equation (6.3), represent for interactions between factors. For example, AE represents for the interaction between the factors pore diameter (A) and incident angle (E). Please note that the factor wavelength of incident radiation is not considered in equation (6.3) because it has been eliminated from the screen test results.

Based on the regression equation (6.3), we can calculate the maximum optical transmission through microporous capillary-array windows by substituting the optimized level of each factor and interaction. By employing the screen test and further half-fractional-factorial design, the optimal condition for achieving the maximum optical transmission is by setting the pore diameter to 50 μm, thickness of the window to 0.5 mm, OAR to 60%, exposed area with a radius of 4 mm, and incident angle of the radiation to 0 degree, which corresponds to normal incidence. The resulting maximum optical transmission through the microporous capillary-array windows is calculated to be 54.97% under this condition.

It is noteworthy that by utilizing this advanced experimental-design methodology, we can achieve optimized transmission efficiency by conducting only 24 experiments (8 for the screen tests and 16 for the further tests), with the best selections of factor levels. In contrast, a complete experimental design consisting of six factors, each with two levels, would necessitate 64 measurements. In addition, even with the implementation of the Resolution VI fractional-factorial design discussed in the Section 6.1, it still requires 32 experiments. Compared to this advanced

method, the utilization of the aforementioned approach results in a substantial reduction in the number of experiments required while still leading to the similar prediction of the optimization.

6.2.2 Milliporous Capillary-array windows

This section is devoted to the analysis of experimental results concerning the optical transmission through milliporous capillary-array windows. To achieve this, we again employ a resolution III fractional-factorial design as an initial screen test, together with a half-fractional-factorial design. Additionally, we apply ANOVA and regression analysis techniques to explore the impact of diverse factors on the optical transmission.

We still employ the design considering six factors to investigate the effect on optical transmission through milliporous capillary-array windows. The six factors that we considered are the same, including pore diameter, thickness of the window, open area ratio (OAR), exposed area, wavelength of the incident radiation, and incident angle of the radiation, each measured at two levels. To efficiently perform a preliminary analysis, a resolution III screen test was conducted, requiring only 8 experimental measurements. As in the resolution III fractional-factorial design methodology described in Chapter 4, a specific set of eight experiments was carried out to measure optical transmission. The experimental data is presented in Table 6.5.

	A	B	C	D	E	F	
	Diameter (mm)	Thickness (mm)	Exposed area (R:mm)	OAR (%)	Wavelength (nm)	Incident angle (degree)	Transmission
1	1.5	1	5	44	253	5	41.81%
2	1.5	1	4	44	105	0	44.55%
3	1.5	0.5	5	20	105	5	18.66%
4	1.5	0.5	4	20	253	0	21.14%
5	1	1	5	20	253	0	20.00%
6	1	1	4	20	105	5	17.52%
7	1	0.5	5	44	105	0	42.31%
8	1	0.5	4	44	253	5	38.85%

Table 6.5 Screen test results on the optical transmission through milliporous capillary-array windows

With utilizing the analysis on the effects of each considered factors and their interactions plus the ANOVA analysis, the Pareto chart of the effects can be achieved, which is shown in Figure 6.5.

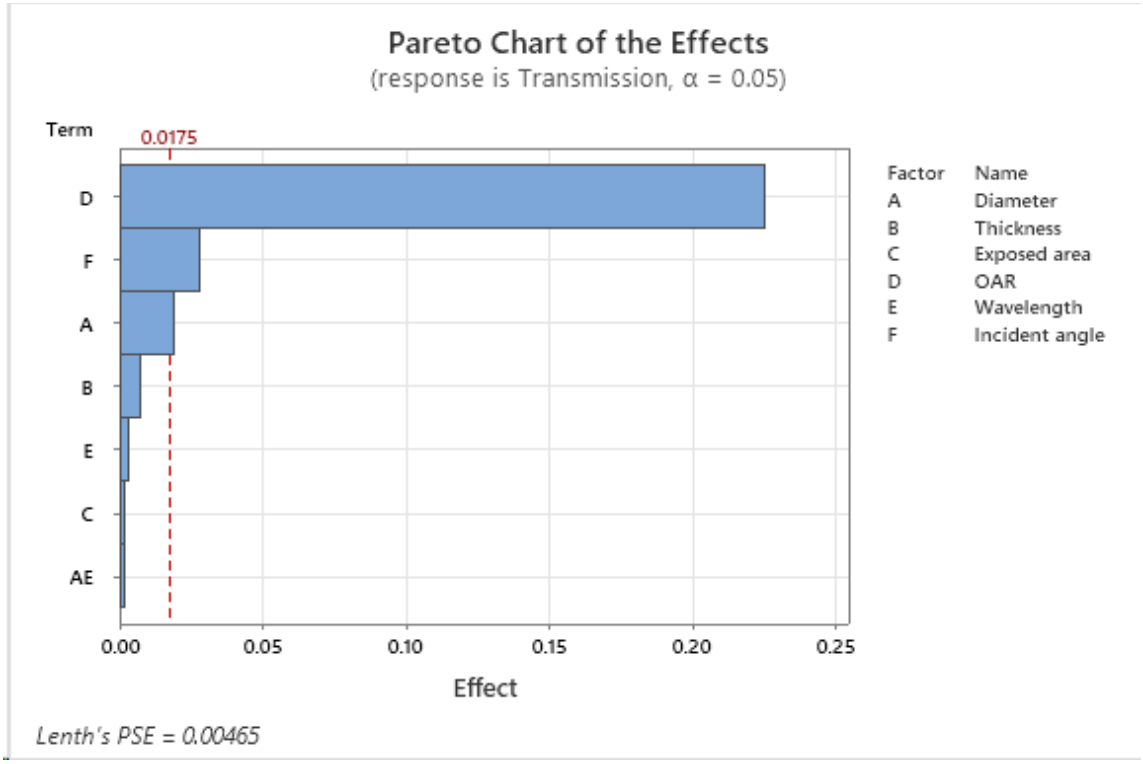

Figure 6.5 Pareto chart of the effects of each factor and their interactions for the milliporous capillary-array windows with utilizing screen tests (8 experiments)

Figure 6.5 displays only seven effects since the remaining effects exhibit negligible impact on the transmission efficiency of milliporous capillary-array windows and only eight experiments were conducted in the screen test. The confidence level α is fixed at 5%, and the red dashed vertical line in Figure 6.5 denotes the reference line corresponding to the significant level of 95%. Compared to the previous Pareto charts in Figures 6.1 and 6.2, the Pareto chart generated by the

screen test reveals three effects exceeding the reference line. The screen test proves helpful in identifying factors with limited influence on the transmission efficiency, which can be excluded from further consideration. Specifically, factors exhibiting effects well below the reference line can be eliminated.

The normalized values of the effect of each single factor and the reference line shown in Figure 6.5 are as follows:

$$D(\text{OAR}) = 0.2255;$$

$$F(\text{Incident angle}) = 0.0279;$$

$$A(\text{Pore diameter}) = 0.0187;$$

$$\text{Reference line} = 0.0175;$$

$$B(\text{Thickness}) = 0.0073;$$

$$E(\text{Wavelength}) = 0.0031;$$

$$C(\text{Exposed area}) = 0.0018;$$

The factors of wavelength and exposed area exhibit effects that are significantly below the reference line and are thus eliminated from further consideration. Again, it should be noted that the primary purpose of conducting a screen test is to exclude certain factors that have a negligible impact on the response variable. However, due to the limited number of experiments conducted during a screen test, it is not possible to obtain precise estimates of the effects of each factor on the response variable. Consequently, the information that can be gleaned from a screen test is restricted in scope. Therefore, a half-fractional-factorial design was performed, considering only four factors: (A) pore diameter, (B) thickness of the window, (C) open area ratio (OAR), and (D) incident angle of the radiation. The first-round screen test comprising eight measurements is

followed by an additional eight measurements in accordance with the half-fractional-factorial design. The experimental outcomes are presented in Table 6.6.

	A	B	C	D	
	Diameter (mm)	Thickness (mm)	OAR (%)	Incident angle (degree)	Transmission
1	1.5	1	44	5	41.81%
2	1.5	1	20	0	19.97%
3	1.5	0.5	44	0	43.74%
4	1.5	0.5	20	5	18.70%
5	1	1	44	0	40.11%
6	1	1	20	5	15.20%
7	1	0.5	44	5	38.34%
8	1	0.5	20	0	17.56%

Table 6.6 Further half-fractional-factorial design experimental results on the optical transmission through milliporous capillary-array windows

The same statistical analysis is applied to the experimental results on the optical transmission through milliporous capillary-array windows with the further half-fractional-factorial design to generate a pareto chart of the effects, which is shown in Figure 6.6.

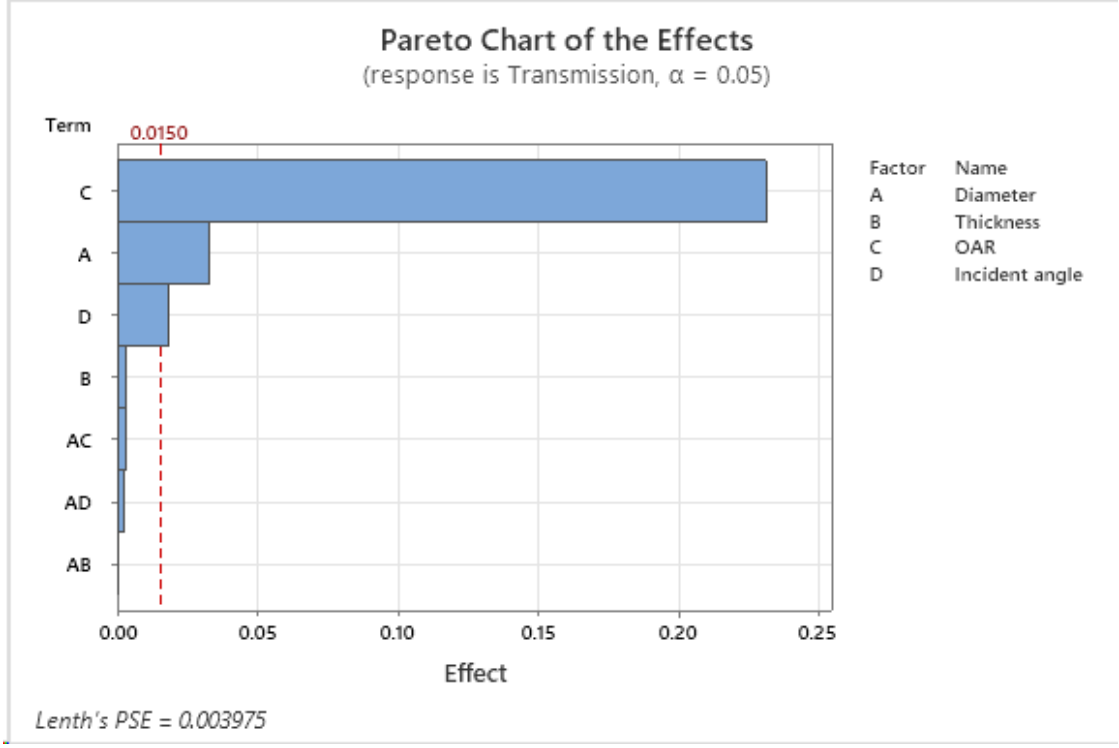

Figure 6.6 Pareto chart of the effects of each factor and their interactions for the milliporous capillary-array windows with further half-fractional-factorial design (8 experiments)

Now, with more measurements were performed, we can see a further statistical analysis on the effects of each factor and the interactions shown in Figure 6.6. The normalized values of the effect of each single factor and the reference line shown in Figure 6.6 are as follows:

$$C(OAR) = 0.2314;$$

$$A(\text{Pore diameter}) = 0.03253;$$

$$D(I\text{ncident angle}) = 0.018325;$$

$$R\text{eference line} = 0.015;$$

$$B(\text{Thickness}) = 0.003125;$$

Therefore, with the help of the further half-fractional-factorial design, we get a more accurate analysis over the effects of each factor and the interactions, which will lead us to the following conclusions:

(1) The reference line for identifying significant effects in the transmission efficiency through milliporous capillary-array windows was determined to be 0.015.

(2) Based on the results of a screen test and a subsequent half-fractional-factorial design, it was found that the factors of wavelength of the incident radiation, exposed area, and thickness of the window had limited impact on the transmission efficiency and were therefore eliminated from further consideration.

(3) The open area ratio (OAR) was found to have the most significant influence on the optical transmission efficiency through milliporous capillary-array windows. Additionally, the factors of pore diameter and incident angle of the radiation were found to have significant influence on the transmission efficiency through milliporous capillary-array windows.

(4) Upon comparing the outcomes of the analysis derived from the screen test with those obtained via the subsequent half-fractional-factorial design, it is evident that the results are highly similar. Consequently, the implementation of the half-fractional-factorial design could be deemed superfluous in terms of further reduction of the experimental trials. Detailed comparison will be presented in the ensuing section.

Using the calculation of regression analysis mentioned in Section 4.3, we can obtain the regression equation as follows:

$$Transmission = 0.2943 + 0.01626A - 0.001563B + 0.1157C$$
$$-0.009162D - 0.001487AC - 0.001163AD + \cdots \quad (6.4)$$

where A represents for the factor pore diameter, B represents for the thickness of the window, C represents for the OAR, and D represents for the incident angle of the radiation. Those cross terms, such as AC and AD, listed in equation (6.4), represent for interactions between factors. For example, AC represents for the interaction between the factors pore diameter (A) and OAR (C). Please note that the factors wavelength of incident radiation and exposed area are not considered in equation (6.4) because they have been eliminated from the screen test.

By using the regression equation (6.4), we can determine the maximum optical transmission through milliporous capillary-array windows by substituting the optimized level of each factor and their interactions. Hence, by utilizing the screen test and further half-fractional-factorial design to implement the experiments and the statistical analysis on the experimental data, the maximum optical transmission through milliporous capillary-array windows is revealed to be 43.67% under the condition that the pore diameter is 1.5 mm, thickness of the window is 0.5 mm, OAR is 44%, and incident angle of the radiation is 0 degrees, *i.e.*, normal incidence.

6.3 Comparison between the methods

In this section, we compare two experimental design methods discussed in sections 6.1 and 6.2, which are the resolution VI fractional-factorial design and a screen test plus a subsequent half-fractional factorial design. The comparison is made in terms of the total number of required trials to complete the experiments and the results obtained from regression analysis and optimization.

Recall that the primary aim of implementing the factorial designs in our project is to minimize the number of experimental trials, leading to time and cost savings. Additionally, the goal is to achieve optimal optical transmission through capillary-array windows with the least number of experimental trials.

6.3.1 Microporous Capillary-array windows

In this section, we present the comparison between the two experimental design methods implemented on measuring the optical transmission through microporous capillary-array windows.

We commence with the overall number of experimental trials. Given that there are six factors, each with two distinct levels, a total of 64 measurements are required to encompass all possible combinations of experimental conditions when no experimental-design method is utilized.

As discussed in Section 6.1, by implementing the resolution VI fractional-factorial design, there are 32 measurements needed to complete the experiment, and we can still obtain the prediction of optimal optical transmission efficiency through the statistical analysis.

However, as discussed in Section 6.2, with the help of the advanced experimental design, which is the combination of a resolution III screen test and a further half-fractional-factorial design, only 24 measurements were taken, and the result of the statistical analysis on optimal transmission stays very close to the result from the resolution VI fractional-factorial design.

Table 6.7 shows the analysis on the effects and reference line of microporous capillary-array windows with implementing two methods.

Method 1		Method 2			
Resolution VI		Screen test		Further fractional-factorial design	
Incident angle	-0.4535	Incident angle	-0.4593	Incident angle	-0.4435
Diameter	0.07002	Reference line	0.2254	Diameter	0.07366
Thickness	-0.05487	Diameter	0.07355	Thickness	-0.02381
OAR	0.014206	Exposed area	-0.0555	Reference line	0.0236
Reference line	0.0096	Thickness	-0.0485	OAR	0.012463
Wavelength	0.001556	OAR	0.01945	Exposed area	-0.000187
Exposed area	-0.000631	Wavelength	0.0038		

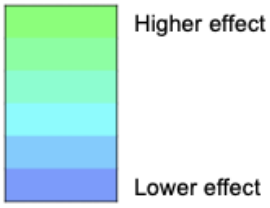

Table 6.7 Comparison between design methods for microporous capillary-array windows

The first two columns in Table 6.7 show the effects of each factor and the reference line with the implementation of method 1, which is the resolution VI fractional-factorial design. A positive value denotes a favorable impact on the transmission ratio, whereas a negative value indicates an unfavorable effect. In addition, A higher numerical value signifies a greater influence on the transmission ratio, whereas a lower numerical value signifies a lower influence on the transmission efficiency. To provide further clarity, the text highlighted in green signifies a higher impact on transmission efficiency, while the text highlighted in blue signifies a lower effect on transmission efficiency. As detailed in Section 6.1, the factors wavelength and exposed area exhibit effects that are considerably below the reference line. Consequently, these two factors may be regarded as insignificant.

In the columns pertaining to method 2, the two middle columns depict the outcomes of the initial round of screen testing. It should be noted that the outcomes of the screen test do not enable an accurate estimation of the magnitude of the factors' impact on transmission efficiency; rather,

the test only identifies and removes the insignificant factor(s). Upon reviewing the outcomes of the initial round of screen testing, as illustrated in the two central columns, it is evident that only one factor, namely incident angle, exhibits an effect that surpasses the reference line. In contrast, the effects of the remaining factors remain consistent with the reference line. It would be erroneous to assert that incident angle is the sole factor that exerts a significant influence on the transmission efficiency, given this observation. In addition, the primary rationale for performing a screen test is to eliminate the least significant factor. Thus, based on the results of the screen test, only one factor, *i.e.*, wavelength of the radiation, can be excluded from further consideration, owing to its effect lying far below the reference line. In order to obtain accurate and precise statistical analysis pertaining to the transmission through microporous capillary-array windows, the subsequent implementation of the half-fractional-factorial design is imperative.

The rest two columns on the right-hand side pertaining to method 2 depict the outcomes of the subsequent half-fractional-factorial design. After eliminating the factor wavelength, the analysis focuses on the remaining five factors. A comparison between method 1 resolution VI fractional-factorial design and method 2 subsequent half-fractional-factorial design reveals that:

(1) The rank order of the effects of each factor in the resolution VI fractional-factorial design remains the same as in the subsequent half-fractional-factorial design.

(2) The magnitude of the effect of each factor in the resolution VI fractional-factorial design is very similar to that in the corresponding factor in the subsequent half-fractional-factorial design.

(3) The reference line in the resolution VI fractional-factorial design is slightly lower than that in the subsequent half-fractional-factorial design. This difference is attributed to the fact that the results of the half-fractional-factorial design are based on only 16 experiments, while the

resolution VI fractional-factorial design involved 32 experiments, providing more information. As such, the results of the resolution VI fractional-factorial design are more accurate, but this does not negate the fact that the outcome of the half-fractional-factorial design in method 2 still offers sufficient information for further analysis aimed at optimizing transmission efficiency.

Regarding the prediction of achieving optimal transmission efficiency using the two design methods, the resolution VI fractional-factorial design in method 1 indicates that the maximum optical transmission through microporous capillary-array windows of 59.24% can be achieved under the following conditions: pore diameter of 50 μm, window thickness of 0.5 mm, OAR of 60%, exposed area with a radius of 4 mm, incident radiation wavelength of 253.6 nm, and normal incidence with an incident angle of 0 degrees. On the other hand, method 2, which combines an initial screen test with a subsequent half-fractional-factorial design, predicts a maximum optical transmission of 54.97% through microporous capillary-array windows under the following conditions: pore diameter of 50 μm, window thickness of 0.5 mm, OAR of 60%, exposed area with a radius of 4 mm, and normal incidence with an incident angle of 0 degrees. Thus, it can be concluded that both methods provide similar and consistent results in terms of predicting the optimal conditions for achieving the maximum transmission efficiency through the microporous capillary-array windows. The small difference in the predicted values of the optimal transmission efficiency can be attributed to the reduced number of experiments in Method 2.

With regards to the number of experimental trials, conducting the entire experiment whilst covering all feasible experimental conditions, given the inclusion of six factors, each with two levels, would necessitate a total of 64 measurements in the absence of any statistical design methodology. Conversely, the implementation of Method 1, which employs the Resolution VI

fractional-factorial design, requires only 32 trials. Regarding Method 2, whilst the screen test with 8 measurements is capable of providing some preliminary insights into the degree to which each factor influences the optical transmission efficiency through microporous capillary-array windows, the subsequent implementation of the half-fractional-factorial design, which requires 16 measurements, is necessary to be performed to obtain a more comprehensive understanding. Thus, a total of 24 experimental trials are required for Method 2.

In conclusion, it is recommended that for measuring the optical transmission through microporous capillary-array windows, the preferred statistical design method is Method 2, which consists of an initial screen test and a subsequent half-fractional-factorial design. This method requires only 24 experimental trials, yet it provides accurate predictions on the optimal transmission efficiency and the most appropriate selection of factor levels to achieve it. Notably, when compared to the approach without any statistical designs, which necessitates 64 experimental trials, or Method 1, which demands 32 experimental trials, Method 2 is highly efficient and cost-effective.

6.3.2 Milliporous Capillary-array windows

In this section, we present a comparison between the two statistical experimental-design methods implemented for measuring the optical transmission through milliporous capillary-array windows.

When considering six factors with two different levels each, a total of 64 experimental measurements are needed to cover all potential combinations of experimental conditions without using any experimental design method.

As discussed in Section 6.1, by implementing Method 1, the resolution VI fractional-factorial design, there are 32 measurements needed to complete the experiment, and we can obtain the prediction of optimal optical transmission efficiency through the statistical analysis.

As discussed in Section 6.2, the utilization of advanced experimental design Method 2, which combines a resolution III screen test with a subsequent half-fractional-factorial design, resulted in the need for only 16 measurements. However, due to the fact that the screen test, consisting of only 8 experimental trials, yielded sufficient information on the effects of each factor in this case of measuring the optical transmission through milliporous capillary-array windows, the Method 2 can be further optimized by solely implementing the initial screen test. As such, the total number of experimental trials required would be reduced to 8.

Table 6.8 shows the analysis on the effects and reference line of milliporous capillary-array windows with implementing two methods.

Method 1		Method 2			
Resolution VI		Screen test		Further fractional-factorial design	
OAR	0.2362	OAR	0.2255	OAR	0.2314
Diameter	0.0256	Incident angle	-0.0279	Diameter	0.03253
Incident angle	-0.02252	Diameter	0.0187	Incident angle	-0.018325
Reference line	0.0067	Reference line	0.0175	Reference line	0.015
Exposed area	-0.004488	Thickness	0.0073	Thickness	-0.003125
Thickness	0.004462	Wavelength	-0.0031		
Wavelength	0.000387	Exposed area	0.0018		

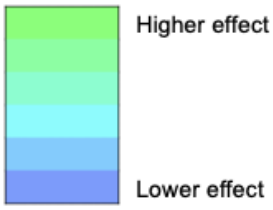

Table 6.8 Comparison between design methods for milliporous capillary-array windows

The first two columns in Table 6.8 show the effects of each factor and the reference line with the implementation of method 1, which is the resolution VI fractional-factorial design. The text highlighted in green signifies a higher effect on the transmission efficiency, while the text highlighted in blue signifies a lower effect on the transmission efficiency. As detailed in Section 6.1, the factors of exposed area, thickness of the window, and the wavelength of incident radiation exhibit effects that are considerably below the reference line. Consequently, these three factors will be regarded as insignificant.

In the columns pertaining to method 2, the two middle columns depict the outcomes of the initial round of screen testing, and the next two columns on the right-hand side pertaining to Method 2 depict the outcomes of the subsequent half-fractional-factorial design, which is the analysis focuses on the remaining four factors after eliminating the factors of the wavelength and the exposed area. The rationale for performing a screen test is to eliminate the least significant factors, and in order to obtain accurate and precise statistical analysis pertaining to the transmission through microporous capillary-array windows, the subsequent implementation of the half-fractional-factorial design is typically imperative. However, upon reviewing the outcomes of the initial round of screen testing and the subsequent half-fractional-factorial design, it becomes

apparent that the results obtained from both screen testing and the subsequent test exhibit a striking similarity in their analysis of the effect of each factor. Moreover, these results are found to be consistent with the results obtained from the implementation of Method 1, which utilizes the Resolution VI fractional-factorial design. A comprehensive comparison between Method 1 and Method 2 is presented as follows:

(1) The rank order of the effect of each factor in Method 1, resolution VI fractional-factorial design, remains highly similar to that observed in both the initial screen test and the subsequent half-fractional-factorial design of Method 2.

(2) The effect magnitude of each factor in Method 1, which is the resolution VI fractional-factorial design, are highly similar to those observed in the corresponding factors of both the initial screen test and the subsequent half-fractional-factorial design of Method 2.

(3) Based on the analysis, it was observed that the reference line in Method 1, which is the resolution VI fractional-factorial design, maintains the same rank order as in both the initial screen test and the subsequent half-fractional-factorial design of Method 2.

(4) If anyone would start out, it is recommended to initially employ Method 2. This approach provides ample information for predicting the maximum transmission efficiency through capillary-array windows, while minimizing the number of experiments needed.

The observed consistency in the rank order and magnitude of the effect of each factor, as well as the reference line, between Method 1, which is the resolution VI fractional-factorial design and Method 2, which comprises an initial screen test and a subsequent half-fractional-factorial design, suggests that the initial screen test alone can provide ample information for statistical

analysis on the effect of each factor and the relationship between each factor and the response variable, namely the optical transmission through microporous capillary-array windows.

Regarding the prediction of achieving optimal transmission efficiency using the two design methods, the resolution VI fractional-factorial design in method 1 indicates that the maximum optical transmission through milliporous capillary-array windows of 45.03% can be achieved under the following conditions: pore diameter of 1.5 mm, window thickness of 1 mm, OAR of 44%, exposed area with a radius of 4 mm, incident radiation wavelength of 253.6 nm, and normal incidence. On the other hand, Method 2, which combines an initial screen test with a subsequent half-fractional-factorial design, predicts a maximum optical transmission of 43.67% through milliporous capillary-array windows under the following conditions: pore diameter of 1.5 mm, window thickness of 0.5 mm, OAR of 44%, and normal incidence. In addition, specifically in the case of measuring the optical transmission efficiency through milliporous capillary-array windows, OAR is the most important factor, which is in a good agreement with the calculations discussed in Chapter 3.

Therefore, it can be concluded that both methods provide similar and consistent results in terms of predicting the optimal conditions for achieving the maximum transmission efficiency through the milliporous capillary-array windows. Although they give a different prediction on the condition of window thickness, with thickness considering as an insignificant factor, it does not make a huge difference. In addition, the tiny difference in the predicted values of the optimal transmission efficiency can be attributed to the reduced number of experiments in method 2, which is a tradeoff for saving time and experimental costs.

In summary, the integration of an initial screen test with a subsequent half-fractional-factorial design provides a practical and effective method for optimizing the transmission

efficiency of milliporous capillary-array windows with only 16 experimental trials. Notably, in this specific case, the initial screen test alone suffices to provide ample information for the optimization of optical transmission through microporous capillary-array windows, requiring only 8 experimental trials as opposed to the 64 required for conducting experiments without statistical design methodology.

6.4 Reference

(1) "*Factorial experiment*", May 7th, 2021. Accessed on: May 15th, 2021. [Online] https://en.wikipedia.org/wiki/Factorial_experiment

(2). C. F. Jeff Wu, Michael S. Hamad, *Experiments: Planning, Analysis, and Optimization, 2nd Edition,* (Wiley, New Jersey, 2009) p. 158-214

(3) Wu, C.F.J. and Chen. Y. "A graph-aided method for planning two-level experiments when certain interactions are important", *Technometrics*, **34**. 162-175.

(4) "*Analysis of variance*", September 5th, 2022. Accessed on: Nov. 6th, 2022. [Online] https://en.wikipedia.org/wiki/Analysis_of_variance

(5) Cohen, J (1968). "Multiple regression as a general data-analytic system". Psychological Bulletin. 70 (6): 426–443.

Chapter 7 – Pressure Differential across the Capillary-array Windows

In this Chapter, we extend our investigation beyond the optical-transmission characteristics of capillary-array windows to evaluate their ability to withstand pressure differentials while maintaining photon or other particle permeability. Please kindly be aware that the pressure tests have not been performed on solid windows due to their minimal transmission of optical radiation within the UV and VUV wavelength range. The solid windows used in our project are not intended for the purpose of transmitting optical radiation while maintaining a pressure differential, which is the main objective of this work. Nonetheless, it is worthwhile to consider conducting such tests in future endeavors to facilitate a comparison with capillary-array windows.

We present the experimental results of pressure tests on capillary-array windows and compare them to the calculations presented in Chapter 3. Based on the combined results of our calculations and experimental measurements, we draw conclusions on several key aspects: (1) the ability of capillary-array windows to withstand pressure differentials, and (2) the maximum pressure differential that can be supported by a capillary-array window before failure occurs.

We conducted pressure tests on nanoporous, microporous, and milliporous capillary-array windows as well as solid films to assess their ability to withstand pressure differentials. The pressure tests were carried out under three distinct conditions: (1) One side of the window was exposed to 10^{-6} torr, while the other side was exposed to 20 mtorr, mimicking the conditions of the optical transmission measurements through capillary-array windows in the ECR system discussed in Chapter 4. (2) The outside of the capillary-array window was exposed to the atmospheric pressure of 760 torr, while the interior was pumped down to 20 mtorr to determine whether the windows could withstand the pressure differential between atmospheric pressure and

the 20 mtorr vacuum required for the generation of UV and VUV radiation. (3) The exterior of the window was maintained at atmospheric pressure, while nitrogen gas was introduced into the pressure-test system and pumped up to a pressure sufficient to cause the window to fail. The third test was conducted only after the window had survived the second pressure test, as the pressure differential in the third test was set to exceed one atmosphere. The objective of the third pressure test is to find the maximum pressure differential that a capillary-array window can hold before failure, and it should be noted that VUV radiation at these pressures is not going to show any results because the high pressure air absorbs the radiation. Through the second and third experiments, we established the maximum pressure differential that a capillary-array window could withstand before breaking and evaluated whether the experimental results were consistent with the calculations presented in Chapter 3.

In the context of testing the pressure differential across capillary-array windows, we conducted experiments with round exposure areas of 4-mm and 5-mm radius. These experiments aimed to examine the influence of the exposed area on both the gas-flow rate through the samples and the maximum pressure differential that a capillary-array window can endure before failure. The results of these tests provide valuable insight into the behavior of capillary-array windows under varying conditions of pressure differential and exposed area.

7.1 Pressure differential across nanoporous capillary-array windows

This work employs two nanoporous capillary-array window samples as specified in Table 2.1 of Chapter 2. The first sample features a pore diameter of 40 nm, a thickness of 50 μm, and an OAR of 34.34%, while the second sample features a pore diameter of 90 nm, a thickness of 100 μm, and an OAR of 47.01%.

The initial pressure test involved subjecting a nanoporous capillary-array window sample to a pressure differential between 10^{-6} torr and 20 mtorr in the ECR system, as detailed in Chapter 4. One side of the capillary-array window was regulated using a Leybold oil-sealed vacuum pump TRIVAC D 90 L, which provides a pumping rate of 110 m^3/h, [1] and a Leybold turbo pump TURBOVAC 600 C, which offers a pumping rate of 2000 m^3/h. [2] The other side of the capillary-array window with 20 mtorr pressure was managed using the same pumps but with a mass-flow controller that introduced argon gas to generate plasma. Experimental outcomes from the pressure tests on the nanoporous capillary-array windows indicated that both samples were able to withstand a pressure differential between 10^{-6} torr and 20 mtorr without breaking, regardless of whether the exposed area was 4 mm or 5 mm in radius.

In the second pressure test, the nanoporous capillary-array window samples were subjected to a specific pressure test setup, which was detailed in Chapter 4 Section 4.2. The setup maintained one side of the sample at 20 mtorr while exposing the other side to atmospheric pressure of 760 torr. The side under the pressure of 20 mtorr was controlled using the Leybold oil-sealed vacuum pump TRIVAC D 90 L, which had a pumping rate of 110 m^3/h, [1] while the other side at atmospheric pressure was entirely exposed to the air. Experimental results indicated that both nanoporous capillary-array window samples could withstand the pressure differential between 760 torr and 20 mtorr without failure, irrespective of the exposed area with 4 mm or 5 mm in radius.

					Pressure differential	
					760 torr to 20 mtorr	20 mtorr to 10^(-6) torr
	Pore diameter	Thickness	OAR	Exposed area (R:mm)	Gas-flow rate 1 (m^3/h)	Gas-flow rate 2 (m^3/h)
Nanoporous	40 nm	50 μm	34%	4	< 0.01	< 0.001
	40 nm	50 μm	34%	5	< 0.01	< 0.001
	90 nm	100 μm	47%	4	< 0.01	< 0.001
	90 nm	100 μm	47%	5	< 0.01	< 0.001

Table 7.1 Calculation of gas-flow rate through nanoporous capillary-array windows

Referring back to the calculations performed in Chapter 3, Section 3.1, whereby the pumping rate through capillary-array windows was determined, it was observed that the dimensions of the two nanoporous capillary-array window samples utilized in the pressure test fall well below the threshold for maintaining a pressure differential between (1) 10^{-6} torr and 20 mtorr and (2) 20 mtorr and 760 torr for either of the exposed areas. The pumping rates required for maintaining these pressure differentials are displayed in Table 7.1, and all values are below 0.001 m^3/h. Moreover, it is noted that the pumping rate available in the pressure-test system greatly exceeds 110 m^3/h, thus indicating that the pumping rate is more than sufficient to uphold these two pressure differentials.

Subsequently, the third pressure test was conducted under the following conditions: one side of the nanoporous capillary-array window sample was exposed to atmospheric pressure, which is 760 torr, while the other side was pressurized with nitrogen gas until the nanoporous capillary-array window sample failed. As previously calculated in Chapter 3, the maximum pressure differential estimations that a nanoporous capillary-array window can withstand before failure are presented in Table 7.2.

Catogery	Diameter	Thickness	OAR	Relative Density (g/cm3)	Pressure At Break (Psi)
Nanoporous	40 nm	50 μm	34.34%	2.594	360
	90 nm	100 μm	47.01%	2.094	490

Table 7.2. Estimation of the maximum pressure differential for nanoporous capillary-array windows can hold before failure

Regrettably, the current pressure test system setup imposed limitations on the maximum pressure differential that it could provide, which was approximately 87 psi (~4500 torr). Consequently, the nanoporous capillary-array windows were tested but not broken during this round of pressure testing. This observation partly confirms the capacity of the nanoporous capillary-array windows to resist a pressure differential beyond 87 psi (~4500 torr). [7]

7.2 Pressure differential across microporous capillary-array windows

The microporous capillary-array window samples that were used in the tests are listed in Table 2.2 in Chapter 2. There are two values for pore diameter, which are 25 and 50 μm, two values for thickness, which are 500 and 1000 μm, and two values for OAR, which are 50 and 60%.

The initial pressure test was conducted in the ECR system, wherein the microporous capillary-array window sample was subjected to a pressure differential ranging from 10^{-6} torr to 20 mtorr. The experimental results of the pressure tests on the microporous capillary-array windows indicate that all the window samples were capable of withstanding the pressure differential without fracturing, irrespective of the exposed area with 4 or 5 mm in radius.

The second pressure test was conducted under the experimental condition whereby one side of the microporous capillary-array window sample was subjected to a pressure of 20 mtorr, while the other side was exposed to atmospheric pressure of 760 torr. The results of the pressure tests on the microporous capillary-array windows demonstrated that all window samples were capable of withstanding the pressure differential between 20 mtorr and 760 torr without experiencing failure, regardless of the exposed area size of either 4 or 5 mm in radius.

The results of the calculations on the required pumping rate for these microporous capillary-array windows to maintain a pressure differential between (1) 10^{-6} torr and 20 mtorr and (2) 20 mtorr and 760 torr for two different exposed areas are listed in Table 7.3.

					Pressure differential	
					760 torr to 20 mtorr	20 mtorr to 10^(-6) torr
	Pore diameter	Thickness	OAR	Exposed area (R:mm)	Gas-flow rate 1 (m^3/h)	Gas-flow rate 2 (m^3/h)
Microporous	50 μm	500 μm	60%	4	0.41	0.001
	50 μm	500 μm	60%	5	0.64	0.002
	50 μm	1000 μm	50%	4	0.17	0.0006
	50 μm	1000 μm	50%	5	0.27	0.0009
	25 μm	500 μm	50%	4	0.09	0.0006
	25 μm	500 μm	50%	5	0.13	0.0009
	25 μm	1000 μm	60%	4	0.05	0.0004
	25 μm	1000 μm	60%	5	0.08	0.0006

Table 7.3 Calculation of gas-flow rates through microporous capillary-array windows

As shown in Table 7.3, the maximum calculated gas-flow rate through the microporous capillary-array window is 0.64 m^3/h. This implies that the minimum pumping rate of the pressure test system must exceed 0.64 m^3/h to maintain a pressure differential between 20 mtorr and 760 torr for a microporous capillary-array window with a 50 μm pore diameter, 500 μm thickness, 60% OAR, and a round exposed area of 5 mm in radius. As discussed in Section 7.1, the Leybold mechanical pump used in the pressure test has a pumping rate of 110 m^3/h, which greatly exceeds the required gas-flow rate to sustain the pressure differential. As expected, all microporous capillary-array windows successfully withstood the pressure differentials applied during the second round pressure test.

The third pressure experiment aimed to investigate the maximum pressure differential that the microporous capillary-array windows can sustain before failure. To achieve this, nitrogen gas was introduced into the inside of the system while maintaining atmospheric pressure (760 torr) on the outside of the capillary-array window. This setup allowed for a pressure differential greater than 760 torr to be applied to the capillary-array window.

The results for the calculation of pressure differential at failure of all the microporous capillary-array windows used in this project are listed in Table 7.4.

Catogery	Diameter	Thickness	OAR	Relative Density (g/cm3)	Pressure At Break (Psi)
Microporous	25 μm	500 μm	50%	1.976	100
	25 μm	1000 μm	60%	1.581	180
	50 μm	500 μm	60%	1.581	80
	50 μm	1000 μm	50%	1.976	140

Table 7.4 Calculation of pressure differential at failure of microporous capillary-array windows

Considering the constraints of the pressure test system, it was observed that the maximum pressure differential it could generate was restricted to approximately 87 psi (~4500 torr). The experimental results of the pressure tests on microporous capillary-array windows show that:

(1) For the microporous capillary-array window with 50 μm in pore diameter, 500 μm in thickness, and 60% OAR, when subjected to an exposed area of either 4 or 5 mm in radius, the microporous capillary-array window fractured at an internal pressure of approximately 91 psi (~4690 torr). Hence, the maximum pressure differential it can tolerate is 76 psi (~3930 torr). It matches the calculation shown in Table 7.4.

(2) Considering the current restrictions of the pressure test system, the maximum achievable pressure differential was limited to around 87 psi (~4500 torr). In light of this constraint, it was observed that none of the remaining microporous capillary-array window samples suffered any fractures or breakage under this test condition. This also matches the results of the calculation listed in Table 7.4.

Therefore, from (a). the calculations of gas-flow rate; (b). the calculation of pressure differential at break; and (c). the results of the experimental measurements, we can draw the conclusions as follows:

(1) All microporous capillary-array window samples can hold the pressure differential between 10^{-6} torr and 20 mtorr as long as sufficient pumping rate is provided. The pumping rate to maintain such pressure differential through these microporous capillary-array windows can be found in Table 7.3.

(2) The results of the pressure tests on the microporous capillary-array window samples revealed that they can withstand the pressure differential between 20 mtorr and 760 torr with the provision of a higher pumping rate. Table 7.3 provides the gas flow rate required to maintain this pressure differential across these microporous capillary-array windows.

(3) Regarding the experimental results of the pressure test on the microporous capillary-array windows under a pressure differential greater than an atmospheric pressure (~760 torr), one window sample with a pore diameter of 50 μm, thickness of 500 μm, and 60% open area ratio (OAR) was found to have fractured under a pressure differential of 76 psi (~3930 torr), whereas the other window samples tested successfully withstanding a pressure differential of at least 87 psi (~4500 torr). These experimental results are consistent with the calculations listed in Table 7.4. However, due to the limitations of the pressure system, the exact maximum pressure differential that these microporous capillary-array windows can withstand could not be determined.

7.3 Pressure differential across milliporous capillary-array windows

The milliporous capillary-array window samples utilized in the pressure tests are documented in Table 2.3, as presented in Chapter 2. The window samples vary in terms of pore diameter, with two distinct sizes of 1 and 1.5 mm, thickness, with two levels of 0.5 and 1 mm, and OAR, with two values of 20% and 44%.

The initial pressure test was conducted in the ECR system with the milliporous capillary-array window subjected to a pressure differential in the range of 10^{-6} torr on one side to 20 mtorr on the other side. The experimental results of the pressure tests on the milliporous capillary-array windows indicate that all the milliporous capillary-array window samples were capable of withstanding the pressure differential between 10^{-6} torr and 20 mtorr without fracturing, regardless of the exposed area size of either 4 or 5 mm in radius.

The second pressure test aimed to investigate whether the milliporous capillary-array windows could withstand a pressure differential between 20 mtorr and 760 torr, with the inside of the window sample at 20 mtorr and the outside at atmospheric pressure of 760 torr. To maintain this pressure differential, a pumping rate of 110 m^3/h was applied to the system. The experimental results indicate that none of the milliporous capillary-array windows broke under these conditions. While some of the window samples successfully withstood the pressure differential within the specified range with this pumping rate, others failed to reach the desired pressure inside the window due to the limited pumping rate of the mechanical pump. The detailed experimental results are presented below.

(1) For the milliporous capillary-array window with a pore diameter of 1.5 mm, thickness of 1 mm, and an OAR of 44%, subjecting it to a pumping rate of 110 m^3/h resulted in the system being pumped down to approximately 46 torr when exposed to the atmosphere at 760 torr with a round area of 4 mm in radius. Similarly, when exposed with a round area of 5 mm in radius, the system can be pumped down to approximately 303 torr, with the window sample not exhibiting any breakage under both conditions. According to Table 7.5, to maintain a pressure differential between 20 mtorr and 760 torr, the pumping rate needs to be at least 115 m^3/h with an exposed round area of 4 mm in radius and 180 m^3/h with an exposed round area of 5 mm in radius.

(2) For the milliporous capillary-array window sample with 1.5 mm pore diameter, 0.5 mm thickness, and 20% OAR, the pressure test was conducted with a round area of 4 mm radius and a pumping rate of 110 m^3/h. The results showed that the sample was able to withstand a pressure differential between 20 mtorr and 760 torr without any damage. This outcome aligns with the calculation presented in Table 7.5, as the required gas-flow rate to maintain this pressure differential is 105 m^3/h, which is lower than the applied pumping rate. However, when tested with a round area of 5 mm radius, the sample survived without breaking, but the inside pressure could only be reduced to around 258 torr. According to the data in Table 7.5, a pumping rate of at least 163 m^3/h is necessary to sustain the pressure differential between 20 mtorr and 760 torr.

(3) For the milliporous capillary-array window sample with 1 mm pore diameter, 1 mm thickness, and 20% OAR, and a pumping rate of 110 m^3/h, the pressure test was conducted with two round areas of 4 and 5 mm in radius, respectively. The results showed that the window could hold the pressure differential without any damage in both conditions. The experimental findings align with the calculation outlined in Table 7.5. Specifically, the gas-flow rate required to maintain the pressure differential was 23 m^3/h and 36 m^3/h for the round-exposed areas with 4 and 5 mm radius, respectively. These values are lower than the pumping rate provided by the mechanical pump, thus validating the suitability of the milliporous capillary-array window for this pressure range.

(4) For the milliporous capillary-array window with 1 mm pore diameter, 0.5 mm thickness, and 44% OAR, when it was exposed to air with a circular area of 4 mm radius and subjected to a pumping rate of 110 m^3/h provided by the mechanical pump, the window successfully held a pressure differential between 20 mtorr and 760 torr without any damage. This experimental result matches well with the calculated values in Table 7.5, as the required gas-flow rate to maintain the pressure differential is found to be 102 m^3/h, which was less than the actual applied pumping rate. However, when the exposed area was increased to 5 mm radius, although no breakage was observed in the milliporous capillary-array window, the pressure inside the window could only be pumped down to approximately 246 torr. According to Table 7.5, a higher pumping rate of at least 159 m^3/h is required to maintain the pressure differential between 20 mtorr and 760 torr for this particular window under the same experimental condition.

Table 7.5 provides the results of calculations conducted to determine the necessary pumping rates for various milliporous capillary-array windows to maintain pressure differentials ranging from 10^{-6} torr to 20 mtorr and from 20 mtorr to 760 torr. The calculations were performed for two different exposed areas.

					Pressure differential	
					760 torr to 20 mtorr	20 mtorr to 10^(-6) torr
	Pore diameter	Thickness	OAR	Exposed area (R:mm)	Gas-flow rate 1 (m^3/h)	Gas-flow rate 2 (m^3/h)
Milliporous	1.5 mm	1 mm	44%	4	115.01	0.016
	1.5 mm	1 mm	44%	5	179.69	0.026
	1.5 mm	0.5 mm	20%	4	104.55	0.015
	1.5 mm	0.5 mm	20%	5	163.36	0.023
	1 mm	1 mm	20%	4	23.23	0.005
	1 mm	1 mm	20%	5	36.3	0.007
	1 mm	0.5 mm	44%	4	102.23	0.021
	1 mm	0.5 mm	44%	5	159.73	0.033

Table 7.5 Calculation of gas-flow rate through milliporous capillary-array windows

As is shown in Table 7.5, the required gas-flow rate for maintaining a pressure differential between 10^{-6} torr and 20 mtorr for all the milliporous capillary-array windows that were used in this project was calculated to be within the normal operating range of the Leybold mechanical pump that used for the pressure test, which provides a pumping rate at 110 m^3/h. However, some of the milliporous capillary-array windows require a higher pumping rate than what the Leybold mechanical pump can provide to maintain the pressure differential between 20 mtorr and 760 torr. The calculated gas-flow rates for maintaining the pressure differential between 20 mtorr and 760 torr, listed in red in Table 7.5, align well with the experimental measurements, particularly for those milliporous capillary-array windows that cannot sustain the pressure differential between 20 mtorr and 760 torr.

Subsequently, a third pressure test was conducted on the milliporous capillary-array windows with the external surface exposed to ambient air while the internal surface was supplied with nitrogen gas at a higher pressure. The primary objective of this pressure test was to determine the maximum pressure differential that the milliporous capillary-array window could sustain without undergoing any damage. The experimental results of the pressure tests on milliporous capillary-array windows show the following:

(1) The milliporous capillary-array window with 1 mm pore diameter, 0.5 mm thickness and 44% OAR was fractured when the inside of the window was feed in with nitrogen to approximately 83 psi (~4310 torr) and the maximum pressure differential this it can hold is then 68 psi (~3550 torr) regardless of whether it was exposed to a round area with a radius of 4 mm or 5 mm.

(2) The milliporous capillary-array window with 1 mm pore diameter, 1 mm thickness and 20% OAR was observed fractured when the inside of the window was pumped up to approximately 87 psi (~4500 torr) and the maximum pressure differential this it can hold is then 72 psi (~3740 torr), regardless of whether it was exposed to a round area with a radius of 4 mm or 5 mm.

(3) The milliporous capillary-array window with 1.5 mm pore diameter, 0.5 mm thickness and 20% OAR failed when the inside of the window was fed in with nitrogen gas to approximately 80 psi (~4130 torr) and the maximum pressure differential this it can hold is then 65 psi (~3370 torr), regardless of whether it was exposed to a round area with a radius of 4 or 5 mm.

(4) The milliporous capillary-array window with 1.5 mm pore diameter, 1 mm thickness and 44% OAR fractured when the inside of the window was pumped up to approximately 83 psi (~4310 torr) and the maximum pressure differential this it can hold is then 68 psi (~3550 torr) regardless of whether it was exposed to a round area with a radius of 4 or 5 mm.

The experimental results pertaining to the maximum pressure differential that a milliporous capillary-array window can withstand before breaking are consistent with the calculations presented in Table 7.6.

Catogery	Diameter	Thickness	OAR	Relative Density (g/cm3)	Calculated Pressure At Break (Psi)	Experimental pressure at break (Psi)
Milliporous	1000 μm	500 μm	44%	2.213	68.211	68
	1000 μm	1000 μm	20%	3.160	72.954	72
	1500 μm	500 μm	20%	3.160	68.153	65
	1500 μm	1000 μm	44%	2.213	69.879	68

Table 7.6 Calculation of pressure differential at break
of milliporous capillary-array windows

Therefore, from (a). the calculations of gas-flow rate; (b). the calculation of pressure differential at break; and (c). the results of the experimental measurements, we can draw the conclusions as follows:

(1) The results of the pressure tests demonstrate that all of the milliporous capillary-array windows can sustain a pressure differential between 10^{-6} torr and 20 mtorr, provided that an adequate pumping rate is supplied. The requisite pumping rate for maintaining this pressure differential through the milliporous capillary-array windows is summarized in Table 7.5.

(2) In accordance with the experimental results, all the samples of milliporous capillary-array windows can sustain the pressure differential ranging from 20 mtorr to 760 torr, provided an adequate pumping rate is supplied. The requisite gas-flow rates for preserving this pressure differential across the milliporous capillary-array windows are also listed in Table 7.5.

(3) In summary, the milliporous capillary-array windows exhibit a limit to the pressure differential they can withstand before breaking. The calculations of the pressure differential at failure, presented in Table 7.6, are in good agreement with the experimental results. Hence, these calculations can serve as a reliable reference for predicting the pressure differential at break for milliporous capillary-array windows with different parameters. Additionally, the experimental findings indicate that the impact of varying the exposed area can be disregarded.

7.4 Reference

(1). "*Leybold TRIVAC D 90 L*", 2022. Accessed on: Dec. 6th, 2022. [Online] https://www.leyboldproducts.us/products/oil-sealed-vacuum-pumps/trivac/trivac-l/pumps/3362/trivac-d-90-l

(2). LEYBOLD, "Leybold Turbovac", Leybold Turbovac Operating Instructions, GA05118_1302, (2004)

(3). Engineering ToolBox, (2014). "*Gases - Dynamic Viscosities*". Accessed on: Dec 4th, 2022. [online] Available at: https://www.engineeringtoolbox.com/gases-absolute-dynamic-viscosity-d_1888.html

(4). Z. Y. Deng, T. Fukasawa, and M. Ando, "Microstructure and Mechanical Properties of Porous Alumina Ceramics Fabricated by the Decomposition of Aluminum Hydroxide", J. Am. Ceram. Soc., **84** [11] 2638-44 (2001)

(5). B. Seeber, U. T. Gonzenbach, and L. Gauckler, "Mechanical properties of highly porous alumina foams", Journal of Material Research, 28(17):2281-2287. DOI: 10.1557/jmr.2013.102, (2013)

(6). S. C. Nanjangud, R. Brezny, D. J. Green, "Strength and Young's Modulus Behavior of a Partially Sintered Porous Alumina", J. Am. Ceram. Soc., **78** [1] 266-68 (1995)

(7). B. Seeber, U. T. Gonzenbach, and L. Gauckler, "Mechanical properties of highly porous alumina foams", Journal of Material Research, 28(17):2281-2287. DOI: 10.1557/jmr.2013.102, (2013)

Chapter 8 – Conclusions and Future Directions

The primary objectives of this research project are to investigate the transmission efficiency of porous capillary-array windows compared to thin solid films, and to evaluate the ability of porous capillary-array windows to withstand a significant pressure differential between atmosphere and vacuum.

Our hypothesis suggests that both porous capillary-array windows and thin solid films have the capability to transmit ultraviolet (UV) and vacuum ultraviolet (VUV) radiation. In addition, we hypothesize that porous capillary-array windows will exhibit significantly higher transmission efficiency than thin solid films while maintaining a significant pressure differential between the atmosphere and vacuum.

To prove the above hypothesis, following tasks have been undertaken:

1. Calculated the gas-flow rates through capillary-array windows and solid windows, the pressure at break of the capillary-array windows, and optical transmission through them as a function of wavelength.
2. Designed fractional-factorial experiments to reduce the number of trials for the UV and VUV transmission measurements while still letting us find the best choices of factors, which are: pore diameter, thickness, the percentage of opening area, the total exposed area, as well as the angle and the wavelength of incident radiation, to obtain the maximum transmission efficiency.
3. Experimentally measured the UV and VUV transmission efficiency through both capillary-array windows and solid windows.
4. Evaluate the weight of each factor and each of their interactions and to estimate the effects of the factors. Used statistical models to analyze the results of the fractional-factorial

design to estimate the combination of factors that output the optimized optical transmission through the capillary-array windows.

5. Experimentally measured the pressure differential across both capillary-array windows, and tested out the maximum pressure differential that one window can hold before break.

The following sections will outline the key findings from this project regarding each tasks required to undertake to prove the hypothesis, and the opportunities for the further research as well.

8.1 Optical transmission

Initially, we conducted an experiment to measure the transmission of UV and VUV radiation through thin solid windows. The experiment considered multiple dimensions of thin solid windows. The results indicated that the thin solid windows were capable of transmitting a maximum of 0.11% of UV radiation at a wavelength of 253.6 nm, and less than 10^{-300}% of VUV radiation at both 104.8 and 106.6 nm in wavelength. The experimental outcomes are highly consistent with the calculations discussed in Chapter 3, Section 3.2.1, which indicate that negligible radiation in the range of UV and VUV can be transmitted through the solid thin film samples, irrespective of the wavelength of the incident radiation in the range we used.

Subsequently, we conducted experiments to measure the transmission of UV and VUV radiation through nanoporous, microporous, and milliporous capillary-array windows. In the case of nanoporous capillary-array windows, the experimental findings revealed a maximum UV transmission ratio of around 1.43% and a maximum VUV transmission ratio of less than 10^{-50}%, which concurred with the calculated transmission ratios of roughly 1% and less than 10^{-30}%, respectively. For microporous capillary-array windows, the experimental results demonstrated a

maximum UV transmission ratio of approximately 58.93% and a maximum VUV transmission ratio of roughly 58.41%, which agreed with the calculated transmission ratio of 60% for both wavelengths. Similarly, the experimental results for milliporous capillary-array windows indicate a maximum UV transmission ratio of around 44.62% and a maximum VUV transmission ratio of 44.87%. These values are in accordance with the calculated transmission ratio of 44% for both wavelengths as well.

Finally, the application of experimental design methods effectively reduced the total number of experimental trials, and by using statistical analysis techniques such as effect analysis, ANOVA, and regression analysis, we were able to predict the maximum optical transmission through both microporous and milliporous capillary-array windows under optimized conditions. Without the implementation of experimental-design methods, it would have been necessary to conduct 64 experiments to cover all possible experimental conditions, considering the six factors with two levels each. However, by utilizing our advanced experimental-design method that combines an initial screen test and a subsequent half-fractional-factorial design, we only needed to perform 24 experiments to obtain sufficient information to correctly predict the maximum optical transmission efficiency through the microporous capillary-array windows, and only 8 experiments to obtain the maximum optical transmission efficiency through the milliporous capillary-array windows. It is noteworthy to mention that in the case of measuring optical transmission efficiency through the milliporous capillary-array windows, the total number of experimental trials was reduced by 87.5%, while still achieving accurate prediction of the maximum experimental outcomes. If this method were to be applied to industrial projects, it is believed that significant cost and time savings could be achieved.

Under the optimized conditions of pore diameter of 50 μm, window thickness of 0.5 mm, OAR of 60%, exposed area with a radius of 4 mm, incident radiation wavelength of 253.6 nm, and normal incidence with an incident angle of 0 degrees, the predicted maximum optical transmission through the microporous capillary-array windows was approximately 59.24%. This value is highly consistent with the experimental results, which showed a maximum transmission of 58.93%, and is in good agreement with the theoretical maximum value of 60%. Similarly, the maximum optical transmission through milliporous capillary-array windows was predicted to be approximately 45.03% under the optimal conditions of pore diameter of 1.5 mm, window thickness of 1 mm, OAR of 44%, exposed area with a radius of 4 mm, incident radiation wavelength of 253.6 nm, and normal incidence with an incident angle of 0 degrees. Notably, this prediction is highly correlated with the experimental results, which demonstrated a maximum transmission of 44.62%. Furthermore, this predicted value is in close agreement with the theoretical maximum value of 44%.

Therefore, with the application of experimental designs and the use of statistical analysis, the maximum optical transmission through capillary-array windows can be successfully and correctly predicted with implementing the minimum number of experimental trials. In addition to predicting optimal experimental outcomes, we have also established the relationships between the experimental response variable, namely the optical transmission ratio, and each of the factors. For instance, an increased pore diameter was found to be positively correlated with the transmission ratio, while an increased incident angle was negatively correlated. The detailed relationships were discussed in Chapter 6.

8.2 Pressure differential

The experiments on measuring the pressure differential across nanoporous, microporous, and milliporous capillary-array windows were conducted under three distinct conditions: (1) One side of the window was exposed to 10^{-6} torr, while the other side was exposed to 20 mtorr, mimicking the conditions of the optical transmission measurements through capillary-array windows in the ECR system discussed in Chapter 4. (2) The outside of the capillary-array window was exposed to atmospheric pressure of 760 torr, while the inside of the window was pumped down to 20 mtorr to determine whether the windows could withstand the pressure differential between atmospheric pressure and the 20 mtorr vacuum required for the generation of UV and VUV radiation. (3) The exterior of the window was maintained at atmospheric pressure of 760 torr, while nitrogen gas was introduced into the pressure test system and the inside of the window was pumped up to a pressure sufficient to cause the window to fail. The third test was conducted only after the window had survived the second pressure test, because the pressure differential in the third test was set to exceed 760 torr, while the maximum absolute pressure differential that could be tested in the second experiment was 760 torr. Through the second and third experiments, we established the maximum pressure differential that a capillary-array window could withstand before breaking and evaluated whether the experimental results were consistent with the calculations presented in Chapter 3.

Two nanoporous capillary-array window samples were initially tested for pressure resistance. In the first round of pressure testing, the samples were subjected to a pressure differential between 10^{-6} torr and 20 mtorr, and both samples were found to have survived. The theoretical calculation suggests that the minimum gas-flow rate required to maintain this pressure differential through the nanoporous capillary-array is less than 0.001 m^3/h. Given that the

pressure test system provides a gas-flow rate of more than 110 m^3/h, the survival of the nanoporous capillary-array windows during the first-round of pressure testing is a good validation of the theory. Similarly, the nanoporous capillary-array windows also survived the second pressure test, which was conducted for pressure differential between 20 mtorr and 760 torr. The calculated minimum gas-flow rate necessary to uphold a pressure differential between 20 millitorr to 760 torr is less than 0.01 m^3/h, which is also considerably lower than the gas-flow rate capacity of the pressure test system. The nanoporous capillary-array windows also demonstrated their ability to withstand pressure during the third pressure test, as they remained intact. However, the pressure differential that the test system can provide is limited to a maximum of 87 psi (~4500 torr), which is Insufficient to test the maximum pressure differential that the nanoporous capillary-array windows can withstand without breaking. The theoretical maximum pressure differential that the nanoporous capillary-array windows can withstand without breaking is approximately 360 psi (~18750 torr) for one of the samples and about 490 psi (~25500 torr) for the other. Although the experimental results are limited by the test system's capabilities, they do demonstrate the nanoporous capillary-array windows' ability to withstand a pressure differential of 87 psi (~4500 torr) without failure. Further pressure tests can be performed to determine the maximum pressure differential that the nanoporous capillary-array windows can withstand.

The microporous capillary-array windows were subjected to the same pressure tests. The microporous capillary-array windows demonstrated excellent durability, remaining intact after both the first and second pressure experiments, which tested their ability to withstand pressure differentials of (1) 10^{-6} torr to 20 mtorr and (2) 20 mtorr to 760 torr, respectively. The minimum gas-flow rate necessary to maintain a pressure differential between 10^{-6} torr and 20 mtorr was calculated to be at least 0.0009 m^3/h, and 0.64 m^3/h for maintaining a pressure differential

between 20 mtorr and 760 torr. The pressure test system's capacity of 110 m^3/h is more than adequate for either of these pressure differentials. The third pressure test sought to determine the maximum pressure differential that the microporous capillary-array windows could withstand before failing. One of the microporous capillary-array windows, with a pore diameter of 50 μm, a window thickness of 500 μm, and an OAR of 60%, fractured at a pressure differential of 76 psi (~3930 torr), which is corresponding to the calculated pressure at break of 80 psi (~4140 torr). The remaining microporous capillary-array window samples survived the third pressure test, where the pressure test system can only provide with testing a pressure differential for up to 87 psi (~4500 torr). According to the calculation results of the pressure at break for these microporous capillary-array windows, the minimum pressure differential required to break them is at least 100 psi (~5170 torr), which is consistent with the experimental results.

All of the milliporous capillary-array windows survived the initial pressure test designed to assess their ability to withstand a pressure differential between 10^{-6} torr and 20 mtorr, similar to the nanoporous and microporous capillary-array windows. The minimum gas-flow rate necessary to maintain this pressure differential was calculated to be 0.033 m^3/h, which was well below the maximum gas-flow rate of 110 m^3/h provided by the pressure system. During the second pressure test, which involved testing the ability of the milliporous capillary-array windows to hold a pressure differential between 20 mtorr and 760 torr, it was observed that some of the capillary-array windows required a gas-flow rate exceeding the maximum rate of 110 m^3/h provided by the pressure system. This result was consistent with theoretical calculations mentioned in Chapter 3. For these windows, the experimental results demonstrated that the inside of the pressure test system could not be pumped down to 20 mtorr when the outside of the system was exposed to an atmospheric pressure of 760 torr. Regrettably, the third pressure test of the milliporous capillary-

array windows yielded unfavorable results, as all the samples either fractured or broke. The calculations indicate that the maximum pressure differential that the milliporous capillary-array windows could withstand before breaking lies within the range of 68 to 72 psi (~ 3520 to 3720 torr). The experimental results validated the theoretical prediction, as one of the windows intended to withstand a pressure differential of 72 psi (~3720 torr) was observed to have fractured at a pressure differential of 70 psi (~3620 torr).

Therefore, the pressure tests conducted to the nanoporous, microporous, and milliporous capillary-array window approved their abilities of withstanding pressure differentials of (1) 10^{-6} torr to 20 mtorr and (2) 20 mtorr to 760 torr. Regrettably, the current pressure test system setup imposed limitations on the maximum pressure differential that it could provide, which was approximately 87 psi (~4500 torr). Consequently, the maximum pressure differential that certain capillary-array windows could endure prior to fracture could not be determined.

8.3 Future Work

Based on the results found in this work, there are a variety of research paths that could help with advancing the application of capillary-array windows in transmitting optical radiation while holding a pressure differential.

Firstly, it should be noted that the capillary-array windows examined in this study feature round pores, though it is possible to explore other pore shapes such as rectangular or hexagonal. Specifically regarding nanoporous capillary-array windows, the propagation of incident radiation in the waveguide may be impacted by changes to the waveguide shape. Therefore, investigating how alterations to pore shape affect transmission efficiency of capillary-array windows could be a valuable avenue for future research. In addition to pore shape, the material used to fabricate the capillary-array windows could influence transmission efficiency through factors such as refractive index, permeability, and permittivity. Hence, exploring the impact of different materials on optical transmission through capillary-array windows could also be an important area of investigation.

Secondly, an alternative approach for future work could be the utilization of response-surface design instead of factorial-design methods to design the experiments and statistically analyze the experimental data. Surface-response design offers a distinct perspective to experiments. By applying a different statistical analysis method alongside surface-response design, it may yield a more accurate prediction of the optimal optical transmission efficiency.

Thirdly, it is important to conduct further research to determine the maximum pressure differential that the capillary-array windows can withstand before experiencing failure. Because the current pressure system only supports tests up to approximately 87 psi, it is necessary to explore alternative pressure testing systems or techniques, including compressive testing, Brazilian disc

testing, and 3-point bending tests, to accurately assess the maximum pressure differential that these capillary-array windows can endure without breaking.

8.4 Closing Statement

In summary, the capillary-array windows have demonstrated promising optical transmission properties for ultraviolet (UV) and vacuum-ultraviolet (VUV) radiation. Not only by effectively transmitting the optical radiation, but they also serve as a barrier against the passage of high-energy electrons, ions, and neutral particles. Therefore, capillary-array windows provide protection to substrates exposed to optical treatments, safeguarding them against damage caused by the impact of such high-energy particles.

Appendix A - Monochromator Scanning System

A.1 Front panel

This LabView program was developed to control the McPherson 234/302 VUV monochromator, whereby a motor within the monochromator was calibrated by the program, and this program enables the grating to rotate to a precise position corresponding to the desired wavelength as set up in the program. Initially, the COM port and GPIB port settings must be correctly selected in the first equipment setup section to establish a connection between the monochromator and the computer, and between the picoammeter and the computer. The monochromator position needs to be set up the same as the start wavelength. In the second section, start wavelength, end wavelength, step size, scan speed and grating model can be setup regarding the specific requirement of the experiment. The real-time spectrum will be displayed in the XY graph as a function of wavelength.

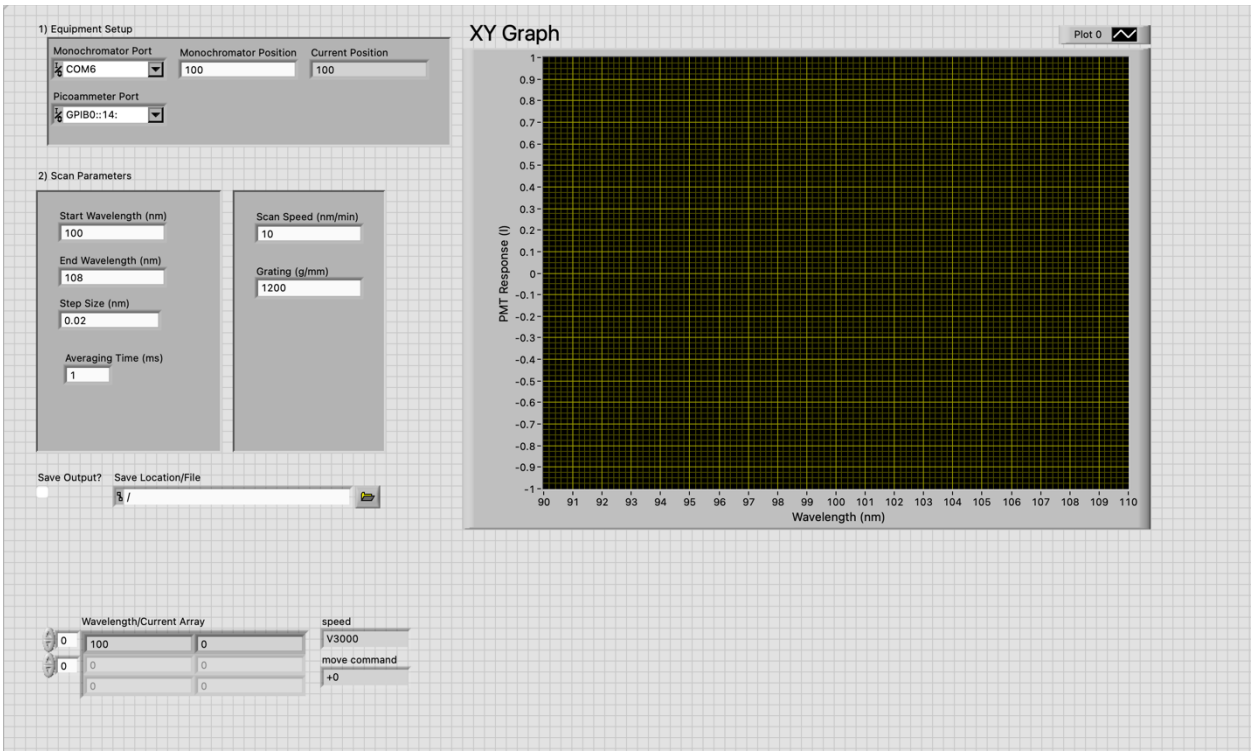

A.2 Block Diagram

The block diagram presents the order of the operations for the monochromator scanning system.

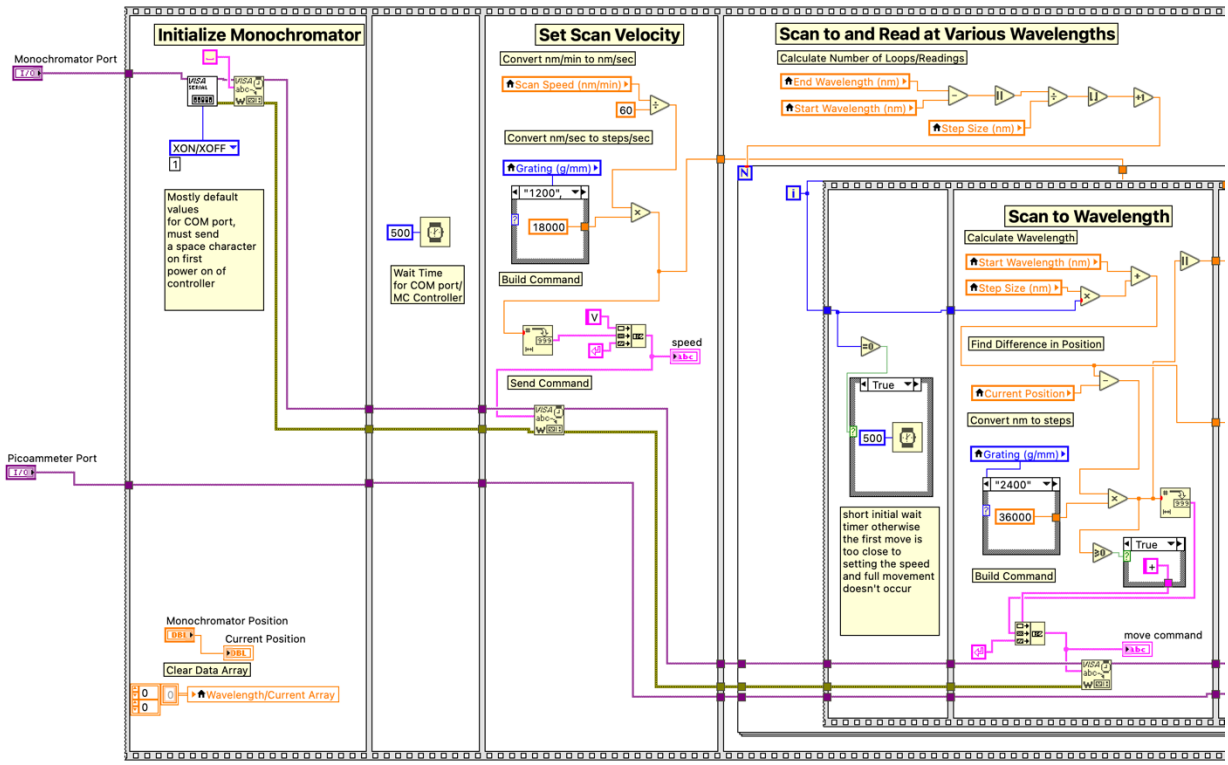

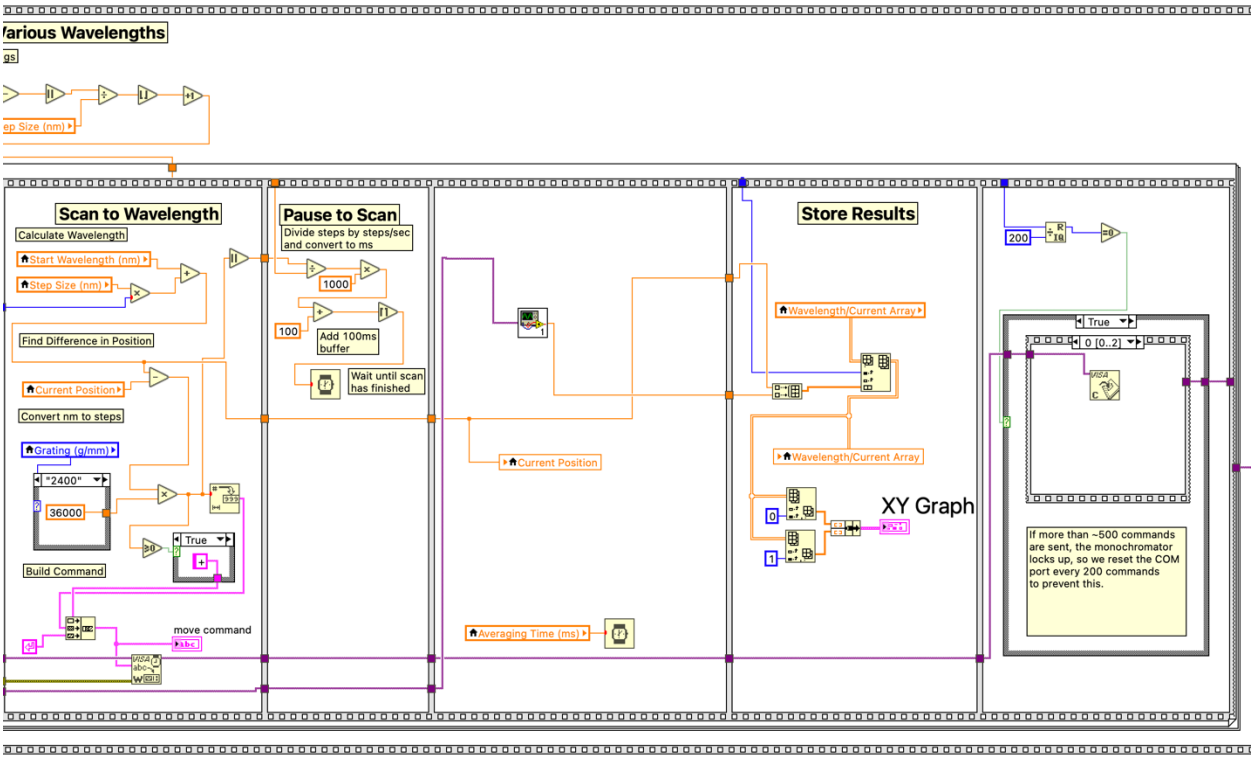
arious Wavelengths
gs
ep Size (nm)
Scan to Wavelength
Calculate Wavelength
Start Wavelength (nm)
Step Size (nm)
Find Difference in Position
Current Position
Convert nm to steps
Grating (g/mm)
"2400"
36000
True
Build Command
move command
Pause to Scan
Divide steps by steps/sec and convert to ms
1000
100
Add 100ms buffer
Wait until scan has finished
Current Position
Averaging Time (ms)
Store Results
Wavelength/Current Array
Wavelength/Current Array
XY Graph
0
1
200
True
0 [0..2]
If more than ~500 commands are sent, the monochromator locks up, so we reset the COM port every 200 commands to prevent this.

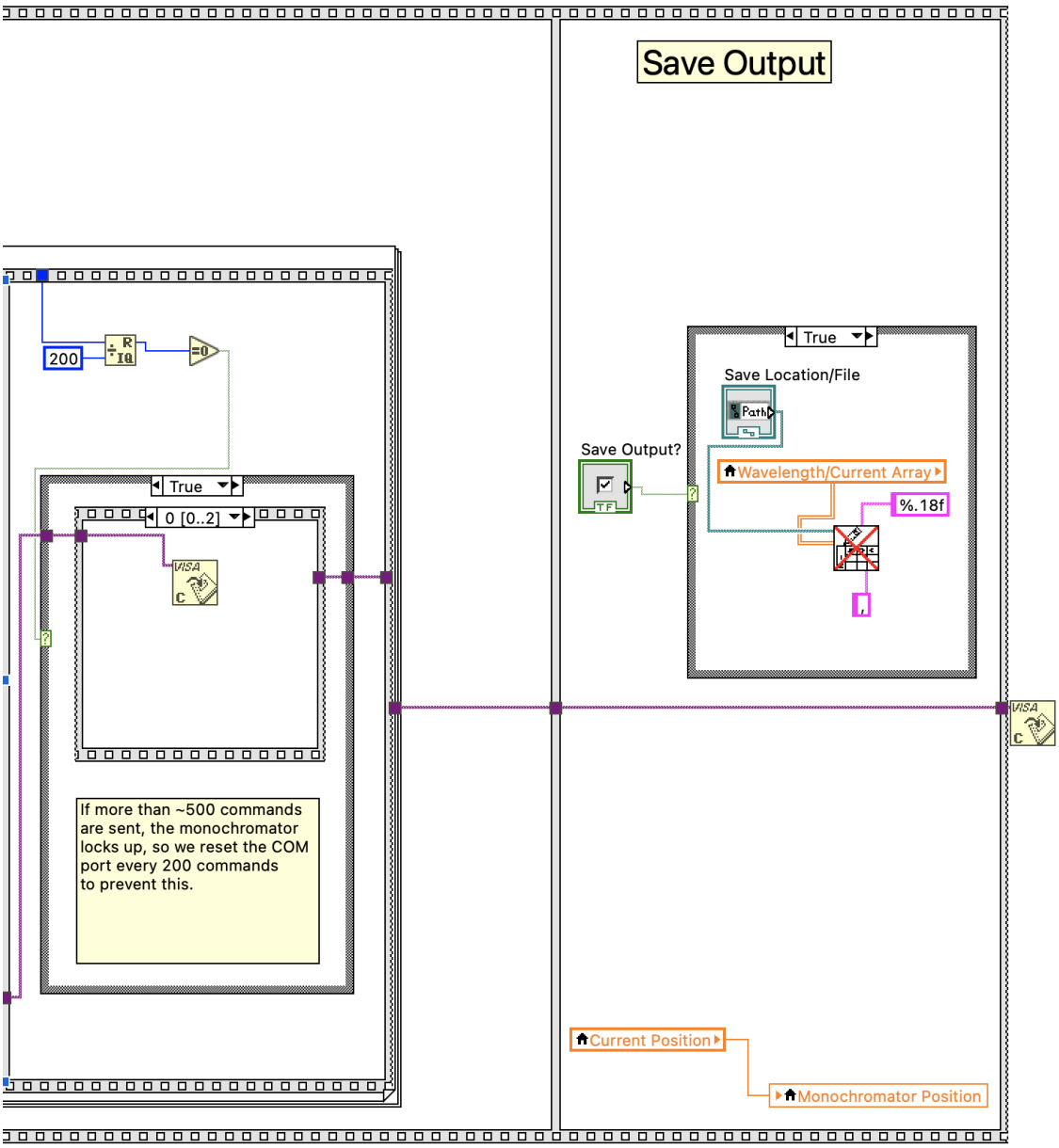
Save Output
200
True
0 [0..2]
VISA
If more than ~500 commands are sent, the monochromator locks up, so we reset the COM port every 200 commands to prevent this.
Save Output?
TF
True
Save Location/File
Path
Wavelength/Current Array
%.18f
VISA
Current Position
Monochromator Position

Appendix B - Picoammeter Signal Processing System

B.1 Front panel

This LabView program was developed to facilitate the acquisition and processing of the current signal generated by the Keithley 6487 picoammeter during optical measurements. Specifically in our experiments, 1000 data points were collected for each wavelength at a sampling rate of 60 Hz and stored in the buffer of the picoammeter. A Fast-Fourier Transform (FFT) algorithm was subsequently applied to convert the data from the time domain to the frequency domain, thereby enabling the application of an extreme low-pass filter (LPF) with a zero Hz cut-off frequency to remove noise and extraneous signals. The processed data was then converted back to the time domain, resulting in the determination of the mean value across all data points for each wavelength. It is necessary to correctly select the address of the picoammeter in the upper left-hand corner of the interface. Additionally, the number of data points in each set can be adjusted, as can the sampling rate of the picoammeter by setting the value of NPLC, which represents the number of power line cycles per second. 1 PLC is equivalent to 16.67 milliseconds at a frequency of 60Hz. The output of the program is displayed in the "FFT first point" cell, while the current signal is plotted as a function of time in the XY graph.

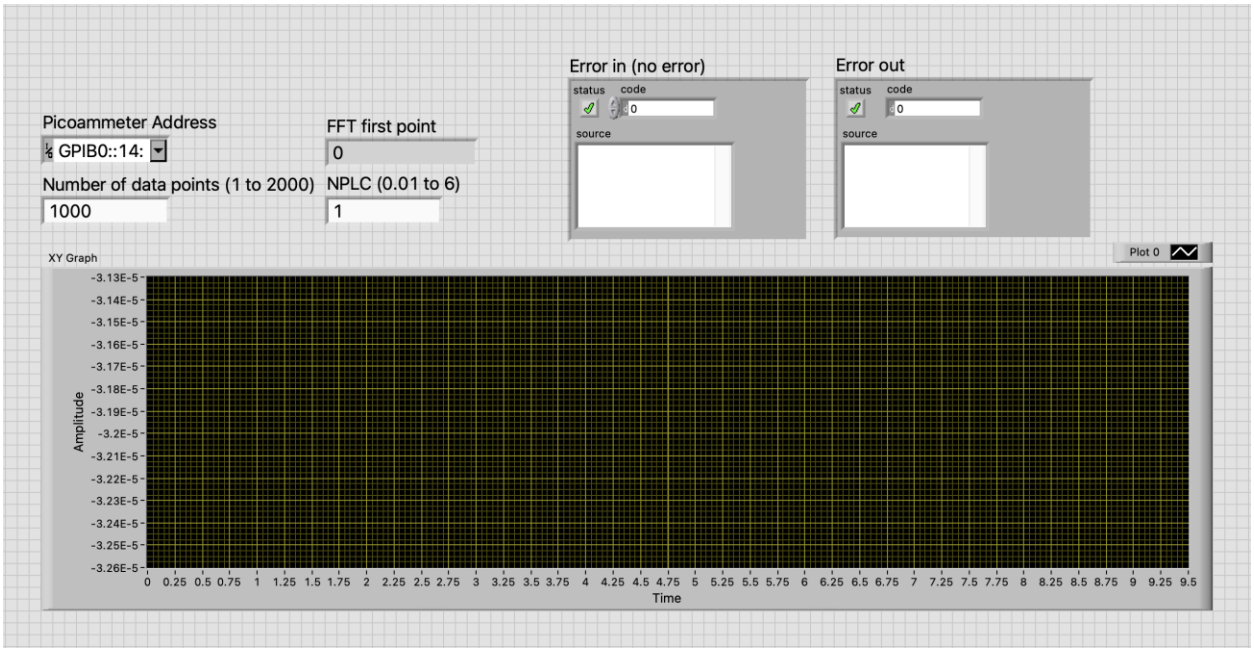

B.2 Block Diagram

The block diagram presents the order of the operations for the monochromator scanning system.

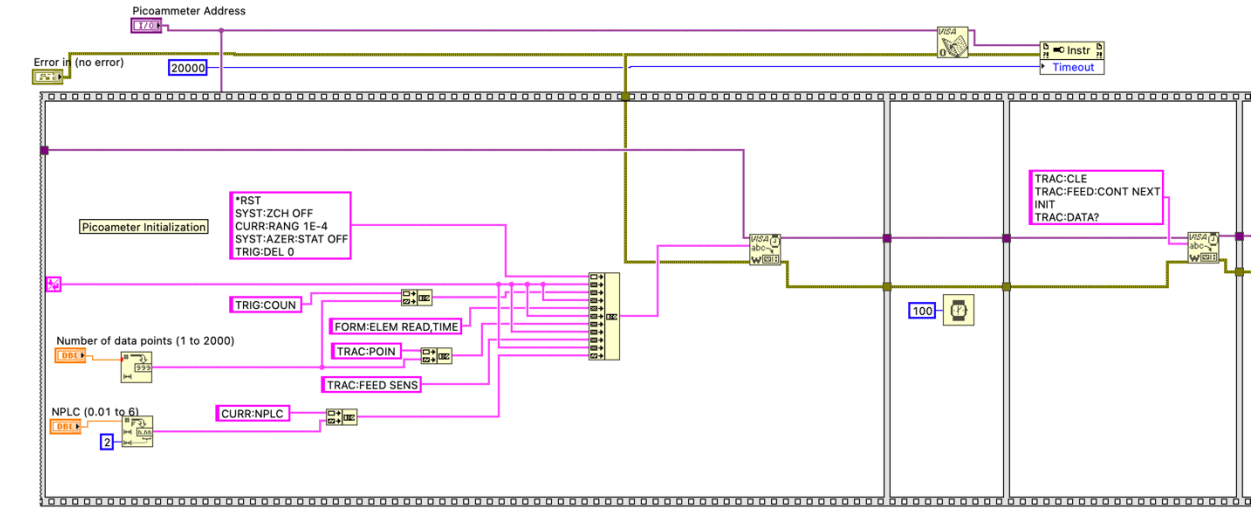

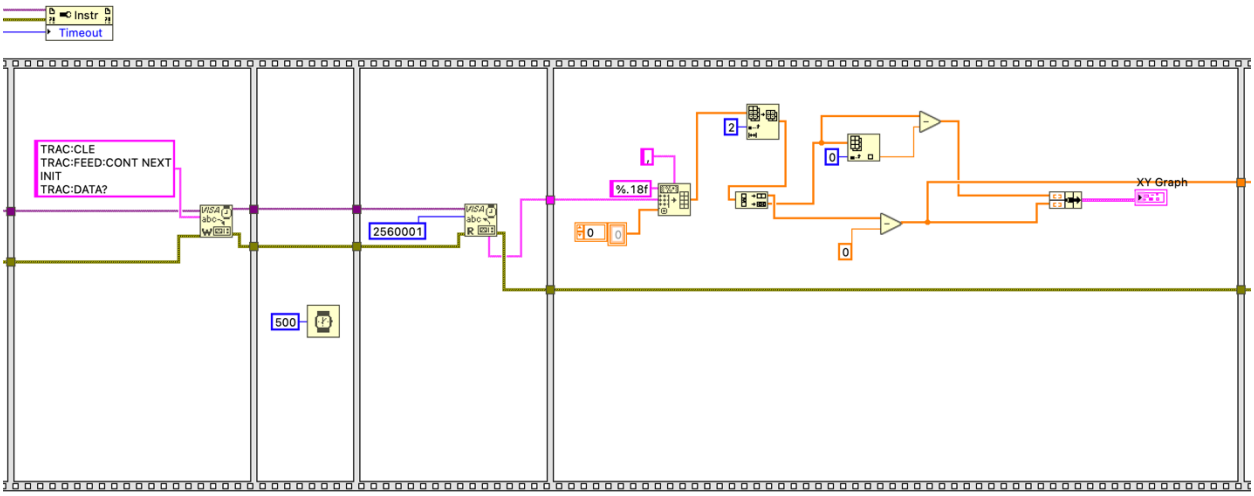

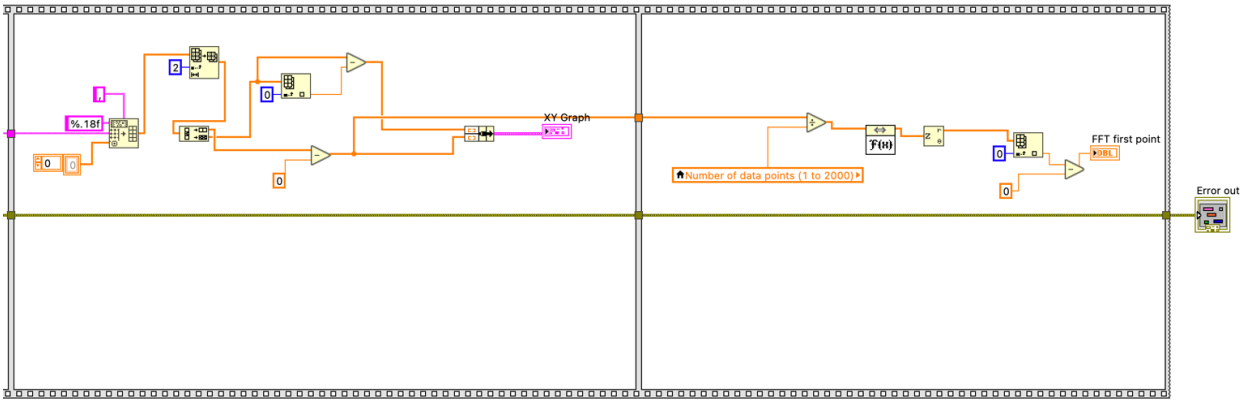
%.18f
XY Graph
Number of data points (1 to 2000)
FFT first point
DBL
Error out